The study of spokes in HiPIMS discharges with applications to the production of superconducting thin films

Francis Lockwood Estrin

Department of Electrical Engineering and Electronics
University of Liverpool

Thesis submitted in accordance with the requirements of the University of Liverpool
Doctor of Philosophy

September 2016

Declaration

I hereby declare that this thesis is my own work and no further sources of information have been used other than the references cited. Neither this thesis nor any part of it have been submitted to any other university or institution for the application of another degree or qualification.

Francis Lockwood Estrin
September 2016

Publications

The research carried out during the course of this study has, thus far, led to the following publications:

- P. Poolcharuansin, **F. Lockwood Estrin**, J. W. Bradley, "The use of segmented cathodes to determine the spoke current density distribution in high power impulse magnetron sputtering plasmas" *Journal of Applied Physics*, Vol. 117, no. 16, p 163304 (2015)
- K. Peter, **F. Lockwood Estrin**, J. Hnilica, P. Vasina, J. W. Bradley, "Simultaneous electrical and optical study of spoke rotation, merging and splitting in HiPIMS plasma" *Journal of Physics D: Applied Physics*, Vol.50, p 015209 (2017)

Conferences

The research carried out during this thesis was presented at the following conferences:

- Seventh International Conference on HiPIMS (**Oral presentation**) -Sheffield Hallam University, UK, 29^{th} - 30^{th} June 2016
- 43^{rd} IEEE International Conference on Plasma Science (**Poster presentation**) -The Banff Centre, Canada, 19^{th} - 23^{th} June 2016
- FuseNet PhD Event 2015 (**Poster presentation**) -Czech Technical University in Prague, Czech Republic, 15^th - 17^th November 2015

Acknowledgements

First I would like to thank my PhD supervisor Prof. James Bradley, for this opportunity, as well as for providing support and guidance though-out my PhD when I needed it. I would also especially like to thank Nu (Phitsanu) from whom i learnt a lot whilst we worked together. I would like to thank all my fellow University of Liverpool PhD students TJ, Fred, Mike, Steven and Mohammed, all of helped me and have now moved onwards.

I also wish to thank the fellow PhD students Tom, Brandony, Mike, Patrick, Ni, Sam, Carl and Pete who are still studying at the University of Liverpool, for the good times we shared. I hope that I was as helpful to you as those who have now left, were to me.

Also mention should be made of the non-academic staff at the University of Liverpool. Lindesy Clarke, Hannah Fosh, and Jane Gallagher who all did great work to make this PhD possible. As did Alan Roby and later Gareth Blacoe, who physically built many vital components of my experimental setups.

Outside of Liverpool i would like to thank everyone I worked and who welcomed me in Masaryk University, particularly Jaroslav Hnilica, Peter Klein and Assoc. Prof. Petr Vasina. Also everyone I worked with at Daresbury Laboratory; Dr Reza valizadeh, Dr Oleg Malyshev, Adrian Hannah, Stuart, Paolo and others.

I also wish to thank all the friends I have made in Liverpool over this time. As well as my family without whom this would not have been possible.

Lastly, I would like to thank the University of Liverpool for funding my studentship.

Abstract

HiPIMS is a method of physical vapour deposition (PVD) used to make thin films. Regions of high optical emission, known as spokes, have recently been discovered in HiPIMS. Spokes have been linked to the production of high energy ions, which can be beneficial for the production of high density thin films. The aim of this PhD has been to develop new methods and diagnostic devices capable of studying spokes in HiPIMS. These are used to gain a greater insight into the make-up of spokes and ultimately to use this knowledge in order to produce higher quality niobium films for potential use in SRF cavities.

The strip probe is one such diagnostic device. It consists of a radial section of the target, electrically isolated from the remainder, but kept at the same potential so that the local current drawn by the plasma above the strip can be measured. The strip probes reveal that in an argon plasma with an aluminium target, the spokes cause the local current to increase by up to 52 % above its base value. Moreover, the amplitude and nature of spokes change in reaction to changing current and power. There were found to be three regimes of spokes: chaotic short lived spokes at lower power and pressure; a spokeless regime at higher power and pressure, where no spokes are visible; and the coherent regime, where spokes are regular and periodic, in-between. It was discovered that there exists an optimum power for each pressure at which spoke amplitude is at a maximum; this effect was found for both aluminium and niobium targets.

The velocity of the spokes in the ExB direction approximately matches the CIV of argon and aluminium, for an argon plasma with an aluminium target. However, at lower pressures of argon, with a niobium target, the spoke velocities are far higher then the CIV.

The strips were also used simultaneously with optical imaging. Different ways of representing the strip probe current are investigated with both the strip probe current plotted as an image and the camera images linearised to a 1D time trace, like the strip probe output. These representations showed that the strip probe current matches the optical emission intensity closely.

The effect of the different spoke conditions on film deposition was tested by making niobium films at different angles to the target in the chaotic, coherent and spokeless regimes

and comparing them to films created by DC sputtering. The results indicated that pressure was the dominant effect, rather then the spoke regime.

Another diagnostic technique developed in this thesis was the triple probe. This was designed to take readings of n_e, T_e, V_f and V_p with a time resolution sufficient to investigate spokes. The triple probe was used to analyse the full HiPIMS pulse, the different spoke regimes and the spokes themselves, just above the target racetrack. The results match those previously taken by the Langmuir probe. It was found that electron temperature was an important factor in the formation of spokes, with spokes mostly absent when $T_e < 2.5$ eV.

The triple probe was also used with the strip probe to investigate spokes and T_e was found to be in anti-phase with n_e. The peaks in the strip probe current also seem to have an influence on T_e, indicating a heating effect from the spokes. This led to a model of rarefaction and heating above the target as the spokes passed beneath.

Suggested future work includes the continued use of the strip probe to detect spokes in systems where optical imaging is impractical and a more in-depth investigation into the effect of spoke regimes and amplitudes on deposited films.

Table of contents

List of figures

List of tables

Symbols and Abbreviations

α_2	A constant equal to $\ln\left(\sqrt{\frac{I_{esat}}{I_{isat}}}\right)$
α_{ss}	Probability that a sputtered neutral will be ionised
β_{ss}	Probability that an ion will self-sputter
ε_0	The permeability of free space
ε_0	The permeability of free space
γ_i	Sputter yield
γ_{ss}	Self-sputter yield
λ_D	Debye length
ω_p	Plasma frequency
ϕ	The electric potential
ϕ_i	Work function
τ	Time delay
A	Area
e	Electron charge
E_p	Energy per pulse
I_A	Average current over full period
I_d	Discharge current
I_{esat}	Electron saturation current

I_{isat}	Ion saturation current
k	The Boltzmann constant
m_i	Ion mass
m_t	Atomic mass of target atom
n_e	Electron/Plasma density
n_i	Ion density
P_A	Total average power
P_d	Probe width
P_g	Probe gap
P_p	Average pulse power
q_i	The ion charge
r_0	racetrack radius
r_L	Gyro-radius
T_e	Electron temperature
T_i	Ion temperature
T_m	Melting temperature
t_{on}	On time
t_{ramp}	The duration of time for the current to ramp
v_b	Bohm velocity
V_d	Discharge voltage
V_f	Floating potential
V_p	Plasma potential
V_{bias}	Battery bias
v_{CIV}	Critical ionisation velocity

Z	The ionisation state of the ions
T_{avg}	Average peak-to-peak period of oscillation
CIV	Critical ionisation velocity
DC	Direct current
f	frequency
HiPIMS	High power impulse magnetron sputtering
ICCD	Image charge-coupled device
m	mode number
PVD	Physical vapour deposition
SRF	Super-conducting radio frequency

Chapter 1

Introduction

Plasma is a state of matter; indeed it is often referred to as the fourth state, after solid, liquid and gas. Plasma is usually thought of as being a mixture of charged particles, normal ions and electrons; however, a better definition is as follows:

Plasma is a quasi-neutral gas of charged and neutral particles, which exhibit collective behaviour. -F. Chen [2]

Many types of matter contain mixtures of charged particles, for example ion and electron beams, acids and even metal crystals. However, none are considered to be plasma, because they fail to exhibit either quasi-neutrality, or collective behaviours. The latter is defined as the process by which the fields of the charged particle convolve in such a way that the particles act together. Collective behaviour was first categorised by Langmuir [3], who recorded regular frequency oscillations emitted from an ionised gas and attributed them to plasma oscillation; this being one example of collective behaviour.

The motion of a single charged particle in an electric or magnetic field can be easily calculated using the Maxwell equations. However plasma contains many charged particles, and their distribution can create electric fields. If an external field is applied to the plasma, the distribution of said charged particles will change in response, creating its own electric fields which interact with the external field; a similar effect occurs in response to magnetic fields. As the bulk distribution of charged particles in the plasma changes the way that the plasma acts when external fields are applied, the charged particles in the plasma are said to act collectively. Plasma oscillations [4] and Debye shielding [5] are two basic examples of collective behaviour and will be detailed in further chapters.

Plasma rarely occurs on earth naturally, especially at sea level where lightning strikes are the only major example. However, in the universe at large, the majority of matter exists as plasma, i.e. stellar-atmospheres [6] and interstellar hydrogen [2]. Man-made plasmas are also quite common now; being used in industry and research as well more domestic application. Their most common use is probably for fluorescent light-bulbs, but numerous other uses have been established, for example in plasma cutting, sterilisation, fusion research and in the focus of this research, the manufacture of films or surface coatings.

Film manufacture, i.e. the coating of one material with another, can be achieved in a variety of ways, some of which involve plasma and some of which do not. Plasma is mainly used for physical vapour deposition (PVD), whereby coatings are formed by physically bombarding a substrate surface with atoms of the desired coating material. As the bombardment continues, these atoms build up until they form a cohesive layer, coating the substrate with a film ranging in thickness from nanometres to tens of micrometres.

The original plasma PVD devices used in this process were a simple target made of the desired coating material in a vacuum, with either a negative DC (direct current) or RF (radio frequency) bias applied to it; this method is known as glow discharges [7]. Such devices have low plasma density, therefore low deposition rates, and additionally they needed to be operated at relatively high pressure. However progress was made when magnetic fields were introduced to improve the electron confinement, leading to the development of the magnetron [8]. The magnetron creates far higher density plasma than would be possible with a glow discharge, allowing a higher deposition rate and operation at lower pressures. This process results in the films being created faster and with a higher density [9] ([10] and references therein).

The deposition of thin films by way of a magnetron has been used for the production of niobium coated copper, superconducting radio frequency (SRF) cavities [11]. SRF cavities are used in particle accelerators, were they are normally made from bulk niobium [12]. Since the 1980s, there have been attempts to use niobium films coated onto copper instead of bulk niobium, as the resulting films have better thermal and accelerator properties [13]. However the use of these films is yet to become standard in this application. Even so, with refinement of PVD magnetron technique, higher quality thin film coatings may replace bulk niobium cavities, meaning better accelerators. One new area of promise is a technique called HiPIMS: high power impulse magnetron sputtering.

Magnetrons are now an industry standard for producing thin films. HiPIMS, proposed in 1999 [14], has been developed and found to be useful for IPVD (ionised PVD) [14] [15].

HiPIMS is a form of pulsed DC sputtering where the power can rise as high as to 10 kW cm^{-2}. These extreme power densities generate high ionisation rates [16], leading the deposit to be highly ionised [15]. These high levels of power cannot be maintained for long time periods [17], so pulses last only of the order of tens of microseconds. Moreover there are long pauses between these pulses, of the order of tens of milliseconds, where no or minimal power is applied. These off-times stop the high levels of power from melting the target [10] [18] [19].

IPVD has many advantages for the manufacture of thin films. For example it has been shown to improve film cohesion, hardness and surface smoothness [20] [21]. These properties can be brought about or enhanced by applying a potential bias to the sample [22] [23]. Normally a negative bias is applied to the sample and this will cause the positive ions to be accelerated towards the sample, allowing greater control and high energy ion impacts on the substrate [24].

Works by Hecimovic et al [25] as well as others [26] [27] have shown that HiPIMS produces high energy ions without the need for biasing. High energy ions have been linked to observed phenomena in HiPIMS known as spokes [28] [29]. Spokes are defined as regions of high ionisation rotating above the target racetrack [30] observed as regions of high optical emission intensity, so called because of their similarity to ionisation zones observed in Hall thrusters and other plasma devices, called 'spokes' [31].

The HiPIMS discharge as a whole has been studied by a large variety of methods; retarding field analysers [15], Langmuir probes [32] [33], film analysis methods [34] and embedded target probes [35]. However, the presence of spokes is random throughout the discharge and the majority of the above methods rely on averaging over multiple pulses to obtain results. This means that they cannot be used to investigate individual spokes. Moreover, spokes have been observed to dynamically change throughout the pulse [36], requiring instruments with a near instantaneous ($\sim$ 500 ns [31]) capture time to investigate individual spokes.

Since their discovery, a variety of different techniques have been applied to investigate the origin and operation of spokes. While electric probes, measuring the floating potential and the ion/electron saturation potential, have been used [37] [28] [38] [23], the majority of investigations into spokes have relied on the use of ICCD cameras [17] [36] [39].

A better understanding of spokes and their links to high energy ions may lead to the development of more effective HiPIMS deposition techniques. The aim of this PhD has been to develop new methods and equipment capable of studying spokes in HiPIMS to obtain a

greater insight into the make-up of spokes and ultimately to use this knowledge to produce higher quality niobium films for potential use in SRF cavities.

Chapter 2

Literature review

This chapter is intended to provide the reader with necessary information to understand the upcoming chapters, as well as giving the work its necessary context. The first section will explain the relevant plasma phenomena, leading to the derivation of key equations that will be used in later chapters. The next section will outline the workings of deposition and the magnetron operation. This will lead on to a section on HiPIMS phenomena and background. The final section will be specifically about the phenomenon of spokes, observed in HiPIMS.

2.1 Plasma physics

If sufficient power is supplied to a gas, as either thermal energy [40], or an electric field [41], the electrons can become dissociated from their atoms and the gas becomes ionised, forming either an ionised gas or a plasma. Plasma is often referred to as the fourth state of matter, because there is a transition of gas to plasma when heat is applied. This is argued to be analogous to the melting and evaporation processes. However, as the other two processes are phase shifts rather than ionisation processes, this analogy is not strictly true [42].

So far, plasma has only been described in terms of an ionised gas; however, to be truly considered plasma, an ionised gas must be quasi-neutral (displaying total charge neutrality, violated on a small scale by inherent dynamic chaos) and exhibit collective behaviour. The first example of collective behaviour was discovered by Langmuir [3], who noticed that samples of ionised gas gave off radiation at a specific set of frequencies. This is an effect of plasma oscillation, described below.

When an electric field is applied to a plasma, the ions and electrons will move in response. Because the electrons are $\sim$2000 times lighter than the ions, they move to their new position so quickly that the ions appear stationary. This leads to an electron deficit in the area vacated.

The electric field caused by the charge separation then starts to act on the electrons (the ions are still considered stationary). The electrons arrive at the positive region filling the electron deficit to the extent that it becomes negatively charged while the surrounding area becomes deficient of electrons and positively charged. The attraction is reversed and the process repeats itself, at a specific frequency, emitting the radiation observed by Langmuir. The frequency of these electron oscillations is called the plasma frequency ω_p.

The reason for the name 'collective behaviour' is apparent from this description. As described, the individual electrons and ions act together so that their collective motion affects the plasma conditions. Plasma frequency, which is an example of collective behaviour, has been shown to affect plasma response to high frequency electric fields (radiation); an area not investigated in this study. Another basic example of collective behaviour, more relevant to this study, is Debye shielding, a behaviour which defines plasma-surface interactions, a major part of this study.

Debye shielding

Non-thermal case

Consider the case of a surface with a permanent positive bias placed inside a quasi-neutral plasma, in the situation where both the ions and electrons are considered only to move when acted upon by an external force (both are non-thermal). The plasma electrons would be attracted to the positively charged surface. On the assumption that the ions are stationary relative to the electrons, the electrons will move to surround the positive surface with an infinitely thin (if the electrons are non-thermal) sheath. The sheath is defined as a closed surface, the inside of which, the 'plasma', can have a net charge, breaking with quasi-neutrality. For this example, the positive surface is assumed to be covered with a dielectric such that the electrons cannot be absorbed. Because of this negative sheath, the bulk plasma (the plasma outside the sheath) is free of any electric field. This is illustrated in figure 2.1.

While this case is highly simplified, the major elements are transferable to more complex systems. For example, when a biased surface is placed in a plasma, it will become surrounded by an opposite charged sheath that will neutralise the bias for the bulk plasma.

Debye sheath

The situation described above becomes more complicated in the case of a more realistic thermal plasma, e.g. one where the electrons have thermal energy. As previously, we assume

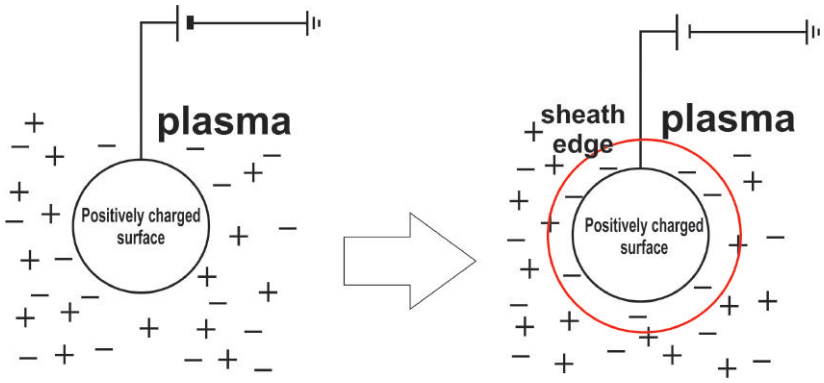

Fig. 2.1 Illustrating plasma response to a positive charge.

the surface in figure 2.1 is covered with a dielectric such that it cannot absorb charged particles from the plasma. This situation is the same as a system with a battery able to maintain the charge despite the incident electrons. Either way, the charge of the charged surface cannot change, and the potential (ϕ), therefore, is a function of position and the spatial distribution of the electrons (ions are assumed to be stationary). Consequently the Poisson equation can be used to calculate the field equation, for both the full 3D case in equation 2.1 and simplified to the 1D case in equation 2.2. For simplicity we chose the 1D case, where x is the distance from a charged surface. Where ε_0 is the permeability of free space, e is the charge of the electron, Z is the ionisation state of the ions (assumed to be 1 for simplicity), ϕ is the electric potential and n_i and n_e are the spatial distribution of the ions and electrons.

$$\varepsilon_0 \nabla^2 \phi = -e(Zn_i - n_e) \tag{2.1}$$

$$\varepsilon_0 \frac{d^2\phi}{dx^2} = -e(Zn_i - n_e) \tag{2.2}$$

We assume that electrons move in the time frame where ions are stationary, e.g. n_i is constant. Quasi-neutrality requires that n_e outside the sheath is equal to n_i (as ions are assumed to be evenly distributed, $n_i = n_0$ the plasma density in the bulk plasma). The distribution of n_e must be a function of the electric field ($\frac{d\phi}{dx}$) and the force of thermal kinetic energy. By treating the electrons as an ideal fluid, we obtain the thermal 'pressure' on the electrons by then imagining an arbitrary closed surface inside the sheath over which the electron 'pressure' (right hand side, equation 2.3) must match the force exerted by the electric field (left hand side, equation 2.3).

$$e\frac{d\phi}{dx} = \frac{kT_e}{n_e}\frac{dn}{dx} \tag{2.3}$$

By solving equation 2.3 and by using quasi-neutrality in the bulk plasma, $x \to \infty$, n_e must equal n_0 , we get equation 2.4, from integrating equation 2.3.

$$n_e = n_0 \exp[e\phi / kT_e] \tag{2.4}$$

Substituting equation 2.4 into equation 2.2 we get equation 2.5, this equation is true at any x (a spherical surface of radius x in 3D space) within the plasma. Choosing an x values (or surface of radius x in 3D) where $e\phi \ / \ kT_e >> 1/2(e\phi \ / \ kT_e)^2$, we can use the Taylor series around zero for e^x until the second term. Provided this is the case, equation 2.5 can be reduced to equation 2.6.

$$\varepsilon_0 \frac{d^2\phi}{dx^2} = en_0(\exp[e\phi / kT_e] - 1) \tag{2.5}$$

$$\varepsilon_0 \frac{d^2\phi}{dx^2} = \frac{e^2 n_0}{kT_e}\phi \tag{2.6}$$

Equation 2.6 can be rearranged to give the shielding of a charge Ψ in a plasma in terms of the Debye length (λ_D), given in equation 2.7. λ_D is given explicitly in equation 2.8.

$$\phi = \Psi e^{-\lambda_D x} \tag{2.7}$$

$$\lambda_D = \sqrt{\frac{\varepsilon_0 kT_e}{n_0 e^2}} \tag{2.8}$$

The Debye length is an important value as it defines the distance over which a plasma can effectively shield an electric field and hence the depth an electric field can penetrate into a plasma.

Bohm criteria

The previous situation considered a surface which maintained a constant charge regardless of what charged flux is applied, from this we derived the shielding of a potential in a plasma. We now consider an uncharged surface, which will change bias depending on the total number of incident ions and electrons, and from this we will derive the flux to a surface.

Consider an unbiased surface able to absorb charged particles; this surface's charge will alter upon the absorption of a charged particle. If the ions are always considered stationary, this system cannot reach a steady state; the electron flux to this surface will experience

exponential decay as the surface's induced negative charge grows. However the electron flux will never reach zero; therefore the system will never reach a equilibrium. It is reasoned that an ion flux is needed, at some point, to balance the electron flux to a surface in order for the system to reach an equilibrium.

To calculate this, we define the following normalised terms, where y and Φ are the kinetic and potential energy of the ions normalised to T_e. n'_e and n'_i are the ion and electron densities, both normalised to the bulk plasma density n_0, and x is the position distance (d) from the surface normalised to λ_D.

$$\begin{aligned} y &= \frac{m_i v^2}{2kT_e} & n'_e &= \frac{n_e}{n_0} \quad n'_i = \frac{n_i}{n_0} \\ \Phi &= \frac{-e\phi}{kT_e} & x &= d/\lambda_D \end{aligned} \tag{2.9}$$

In order to find the flux of ions to the surface, we use ion continuity and the conservation of energy. Ion continuity is derived from fluid dynamics and is a result of ions being unable to leave the system. For 1D system, the ion flux ($n_i(x)v(x)$) through a surface at point x in the sheath must be equal for all values of x. The ion continuity is given in normalised terms in equation 2.10, where y_0 is the initial ion kinetic energy of an ion entering the sheath.

$$n'_i y^{1/2} = {y_0}^{1/2} \tag{2.10}$$

Conservation of energy requires the initial energy of the ion, in terms of both y_0 and the initial potential energy, to equal the final kinetic energy at the charged surface energy; e.g. $y = y_0 + \Phi$.

It can be immediately seen from ion continuity (equation 2.10) that unless the ions enter the sheath with some initial kinetic energy y_0 e.g. $y_0 > 0$, then the ion flux to the surface will be zero. As we maintain the assumption that ions are non-thermal, that is to say they have no thermal y_0, this seems to be a paradox.

However as the sheath displays an exponential decay (never reaching zero), it technically covers the entire plasma, so therefore ions cannot be said to "enter" the sheath. This exponential behaviour is also the origin of our need for an ion flux. To address this, we assume a "pre-sheath" with a charge $\Phi_{pre-sheath}$ sufficient to accelerate an ion in the bulk plasma to y_0 (where y_0 is to be calculated). An important assumption is that the pre-sheath is quasi-neutral, as quasi-neutrality can only be broken in the sheath.

The ion continuity equation (equation 2.10) and energy conservation equation are combined to get the ion distribution in terms of Φ, equation 2.1.

$$n_i' = (1 + \Phi/y_0)^{-1/2} \tag{2.11}$$

Equation 2.11 can be used in the Poisson equation (equation 2.5) with the previously derived electron distribution (equation 2.3) to give equation 2.12(the unit-less form).

$$\frac{d^2\Phi}{dx^2} = (1 + \Phi/y_0)^{-1/2} - e^{-\Phi} \tag{2.12}$$

Equation 2.12 can then be integrated, using the boundary conditions as $x \to \infty$, Φ and Φ' $\to 0$ to give equation 2.13.

$$\left\{\frac{d\Phi}{dx}\right\}^2 = 4y_0((1 + \Phi/y_0)^{1/2} - 1) + 2(e^{-\Phi} - 1) \tag{2.13}$$

Equation 2.13 cannot be reduced further, but it can be solved analytically. By taking the Taylor expansion of equation 2.13, until the Φ^2 term, the result is equation 2.14

$$\left\{\frac{d\Phi}{dx}\right\}^2 = (1 - \frac{1}{2y_0})\Phi^2 + ... \tag{2.14}$$

It can be seen from equation 2.14 that if we discount the Φ^3 or higher power terms, a real solution is subject to the condition $y_0 \geq 1/2$. Re-stated, the ion must enter the sheath with initial velocity (v_b), $v_b = \sqrt{\frac{kT_e}{m_i}}$, known as the Bohm velocity.

Child-Langmuir law

Using the Bohm velocity and the ion continuity equation, it is possible to calculate the total flux of ions or electrons through a sheath, and thus the expected current to a wire of area A and bias ϕ in a plasma.

It is easier to calculate the n_i and v_i at the sheath edge where $v_i = v_b$ (the Bohm velocity), than at $x = 0$ (the probe surface). The current can then be calculated using ion continuity as $n_i v_i = n_i(0)v_i(0)$. The ion current I_{isat} component of the current to a surface is given by equation 2.15 where n_i(b) is the density at the sheath edge and q_i is the ion charge (eZ).

$$I_{isat} = q_i n_i(b) v_b A \tag{2.15}$$

To find n_i(b), the ion density at the sheath boundary, we use the assumption that the pre-sheath is quasi-neutral, therefore $n_i = n_e$. n_e is defined by equation 2.4 as we know ϕ at

the sheath edge is ϕ =-kT_e/2e, $n_i = n_e = n_0$ exp(-1/2). Therefore I_{isat} in its complete form is given in equation 2.16.

$$I_{isat} = q_i \sqrt{\frac{kT_e}{m_i}} A e^{-1/2} \tag{2.16}$$

It is harder to calculate the electron component of the current I_e to a surface because for the electrons there is a thermal component. Equation 2.4, with a modification that the potential in the plasma V_p is not necessarily equal to ground, is given in equation 2.17. We also use the initial electron velocity v_e, which is the thermal electron velocity through a solid angle to a surface. The current (equation 2.15) must be modified for a temperature in a 3D system and the result is given in equation 2.17.

$$\begin{aligned} I_e &= 1/4 e n_e v_e A \\ n_e(0) &= n_0 \exp[e(\phi - V_p)/kT_e] \\ v_e &= \sqrt{\frac{8T_e}{\pi m_e}} \end{aligned} \tag{2.17}$$

From the three equations in 2.17, we obtain the formula for the electron current to a charged surface in a plasma equation 2.18, under the condition exp[q($\phi - V_p$)/kT_e] ≤ 1.

$$I_e = eAn_0 \sqrt{\frac{T_e}{2\pi m_e}} \exp[q(\phi - V_p)/kT_e] \tag{2.18}$$

By combining equation 2.18 and 2.16, we get the total current to a wire without sheath expansion given in equation 2.19 in the full and reduced form.

$$\begin{aligned} I(\phi) &= eAn_0 \sqrt{\frac{T_e}{2\pi m_e}} \exp[e(\phi - V_p)/kT_e] - q_i \sqrt{\frac{kT_e}{m_i}} A e^{-1/2} \\ I(\phi) &= I_{esat} \exp[q(\phi - V_p)/kT_e] - I_{isat} \end{aligned} \tag{2.19}$$

Equation 2.19 is used in plasma diagnostics, as it defines the plasma's response to applied voltages and currents, relative to important plasma parameters such as V_p, n_0 (reported as n_e for the remainder of this thesis) and T_e. Hence these important plasma parameters can be calculated from the voltage-current response of the plasma. All the equations in this section were calculated under the assumption that the ions are non-thermal.

Gyroscopic motion

When a charged particle in a plasma (or isolated) is acted upon by an external electric field, it will move in response; the motion of these individual particles can affect the behaviour

of plasma generally as seen for Debye shielding. The same is true for a magnetic fields. The important example of this interaction for our study is the interaction between ions and electrons moving through a magnetic field.

A particle of charge q moving through a magnetic field $\overline{B}$ at velocity $\overline{v}$ where $v_{\perp}$ is velocity perpendicular to the $\overline{B}$-field and $v_{\parallel}$ parallel to $\overline{B}$, will experience a force $\overline{F}$ given by equation 2.20.

$$\overline{F} = q\,\overline{v} \times \overline{B} \tag{2.20}$$

The force $\overline{F}$ can also be written as mass times the second derivative of $\overline{v}$ (Newton's Second Law); from this substitution, the equation of motion can be calculated. If $v_{\perp} \neq 0$, then the charged particle will execute a circular motion in the plane perpendicular to $\overline{B}$. However the $v_{\parallel}$ component to $\overline{v}$ will be unaffected by the magnetic field and so the particle will continue to travel along the magnetic field line in a corkscrew motion with a gyro-radius (r_L) (radius of circular motion) given by equation 2.21.

$$r_L = \frac{mv_{\perp}}{qB} \tag{2.21}$$

The charged particles of a plasma will follow the same laws of motion, and will travel in circular gyrations along the magnetic field lines until they are disrupted from this path by either a collision or a change in the B-field. This means that charge particle are transported along the magnetic field line far more efficiently than they are transported perpendicularly, magnetically confining the plasma.

However, unlike the Debye shielding, as magnetically confined charged particles can be transported perpendicular to a magnetic field by collisions, the frequency of collisions acts counter to magnetic confinement.The frequency of collisions is governed by plasma density. Calculating the effectiveness of magnetic confinement involves not only knowing the particles gyro-radius but the frequency of collisions in the plasma. For high density plasma, where collisions are frequent, the gyro-motion is often disrupted such that charged particles are moved perpendicular to the magnetic field. In these situations, charged particles are transported in all directions with similar efficiency so there is no magnetic confinement.

This is only the case in higher density plasmas where the mean free path $l \approx r_L$ then the charged particles will not follow gyroscopic motion and the plasma can be considered un-magnetised. However if $l >> r_L$ then the gryo-motion will be unimpeded and the plasma will be contained by the magnetic field.

It should be noted that ions and electrons can have different r_L.

2.2 Technological plasmas

It is often said that 99 % of matter in the universe exists as plasma, in some form [2]. Although this is impossible to prove, the suggestion does demonstrate the abundance and variety of conditions at which plasmas occur. These range from interstellar hydrogen where the plasma density and electron temperature are less than $n_e < 10^{-6}\ m^{-3}$ and $T_e < 0.01$ eV [43] to stellar atmospheres, with density and temperatures of greater than $n_e > 10^{31}\ m^{-3}$ and $T_e > 10^4$ eV [44].

Man-made plasmas have a similarly wide range of operating conditions, with some operating at atmospheric pressures while others require artificial vacuum conditions [8] or only exist on the order of nanoseconds [45]. The man-made plasmas of both high density and T_e plasma are mostly used in nuclear fusion, and as such attempt to mimic the conditions found in stellar atmospheres. In contrast, lower density plasmas tend to be used in industrial applications [46].

There is an important distinction separating the behaviour of the technological plasmas studied here and other plasmas not discussed, which is the behaviour of the ions and whether these ions can be considered non-thermal. In this study, we observe technological plasmas where $T_e >> T_i$, and therefore the calculations in the previous section are considered valid.

Physical vapour deposition (PVD) by sputtering

The plasmas discussed in this study were created with the intent of depositing thin films through PVD. PVD is a method for creating coatings and thin films on a surface without the film chemically reacting with either the surface or the desired coating material, as occurs in chemical vapour deposition (CVD). The PVD process starts with a target of the coating material being vaporised and the vapour condensing on the substrate to form a coating.

Plasma is often used in PVD as a means to vaporise a target, such as in this study where the type of PVD used is sputtering. This occurs when a surface is vaporised by the impact of energetic particles, in this case ions from a plasma. The neutrals are ejected from the target, in some cases with a high kinetic energy, and then travel to the substrate condensing on it to form a film.

When an ion strikes a surface, as shown in figure 2.2, it sets off a series of Newtonian collisions between the sputtering ion and the target atoms. These collisions may result in one or more of the target ions being ejected. The maximum energy of the sputtered atoms will be a function of the incident ion energy (E_{ion}), the relative masses of the incident ion (m_i) and

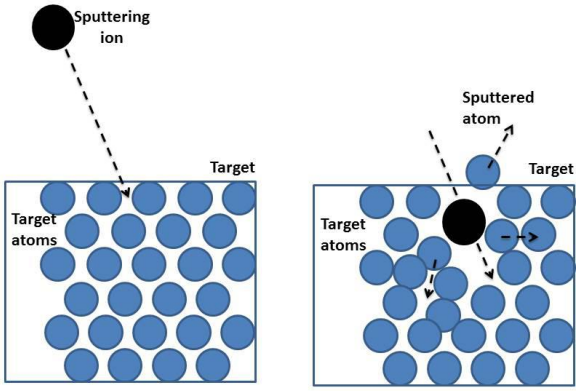

Fig. 2.2 Illustration of sputtering, showing the before and after of a sputtering ion hitting the target surface.

the target atoms (m_t), as shown in equation 2.22 (calculated from Newtonian mechanics).

$$E_{Max} = E_{ion} \frac{4 m_t m_i}{(m_i + m_t)^2} \tag{2.22}$$

The Thompson energy distribution of sputtered particles is given in equation 2.23, where E is the energy of the ejected ion and U_s is the surface binding energy [47]; the distribution from equation 2.23, has a peak at U_s / 2.

$$f(E) \propto \frac{E}{(E + U_s)^3} \tag{2.23}$$

Additionally to the ion energy, there is the possibility of ejection of multiple atoms from a single impact: the so called sputter yield (γ_i) (where i is the incident ion) denotes the mean sputtered atoms per incident ion. The sputter yield is a function of both incident ion and target neutral mass, as well as E_{ion}.

Secondary electrons

As well as sputtered atoms leaving the target surface, electrons, known as secondary electrons, can also be ejected from the target surface. Secondary electrons become very important in the case where the target is subject to electrical biasing, as after there ejection they are accelerated through the target potential, arriving in the plasma with energy equal to the target bias relative to the plasma. There are different paths for secondary electron emission [48]; however here we concentrate on Auger emission [49], the most likely mechanism at the levels of sputter energy used in this study, $<$ 1 000 eV energy [48].

As ions have a net positive charge when an ion approaches a target, there is the possibility for the electron to quantum tunnel from the target to the ion and therefore to neutralise it. If an electron jumps from a target atom to the ion's ground state to neutralise it, it will have the excess energy E_{iz} (the ionisation energy). This energy can be absorbed by a secondary electron in the target and if E_{iz} is sufficiently high, $E_{iz} > 2\phi_t$ (where ϕ_t is the target work function), this secondary electron will be ejected once it has absorbed the excess energy.

From experimentation by Baragiola et al [50], it was found that the secondary electron yields, (γ_{se}), is approximately given by equation 2.24

$$\gamma_{se} \approx 0.032(0.78E_{iz} - 2\phi_t) \tag{2.24}$$

Film growth

In order to design a plasma system for use in PVD an understanding of how films are formed is required.

A film grows from sputtered atoms condensing on the surface of a substrate. The position at which the ions first condense is known as a nucleation site. These nucleation sites act as points on the substrate from which further growth can develop. The growth from this point can be modelled as islands, layers or Stranski-Kranstanov growth.

In island growth, as a result of the binding atoms attaching to each other more strongly than to the surface, the nucleation sites grow into 3D stable clusters known as islands. In layer growth, the neutrals attach to the substrate more strongly than to each other so the atoms condense on the substrate surface, initially coating it in a mono-layer before further growth layer by layer. The Stranski-Kranstanov mode is an intermediate combination, where the film grows initially as a layer before islands form [51].

Once the films have grown significantly, to the point where the model of growth is no longer important, the grain structure develops, affecting the films' density, smoothness and structure. When the film atoms are immobile, the film grains form into round topped columns, and this structure is known as a porous columnar structure. The porous columnar structure is a result of the columns growing so that they shadow themselves and other columns. As the name would suggest, the porous columns have a low density, due to the columns shadowing and leaving gaps; this condition of growth is called zone 1. To avoid this, energy can be input in the form of substrate heating. This gives atoms the energy to defuse in the film and to fill the shadowed voids leading to denser film. However there is still a columnar structure; this typically occurs when the substrate temperature relative to the film's melting point (T/T_m in $^\circ$kelvin) is $0.5 < T/T_m < 0.8$ called zone II. when the substrate temperature approaches the

film's melting temperature, zone III, the atoms in the film can fully defuse filling the volume and leading to a smooth dense film with randomly aligned grains.

Ion bombardment can be applied to film deposition creating a new zone T. An ion striking the film can break the existing grain structures to prevent the porous columns forming. This implants the ion in the crystal structure, acting to increase ion mobility. The grains in zone T are fibrous, and grow perpendicular to the substrate surface giving films in zone T a high density and a smooth surface. The energy of the ions hitting the substrate and substrate temperature affects the zone T transmission. The ion energy term in this transition is fully investigated by Anders [52]; however normally the pressure of deposition [53] is used to denote ion energy (as it is normally the dominant factor). T/T_m for zone T occurs in the range $0.3 < T/T_m < 0.5$.

Plasma deposition

The use of plasma for PVD sputtering has been long established [7] [10]. To heat the ions so that their thermal energy T_i is enough to cause sputtering would require very high energies. Therefore, rather then relying on T_i for sputtering, non-thermal ions must be accelerated through a potential to strike the target with sufficient energy (E_{ion}) to cause sputtering. The first generation of plasma sputtering devices were simply a negatively charged target in a vacuum vessel, shown in figure 2.3. These simple sputtering devices are known as glow discharges. The vacuum is needed to reduce arcing in the plasma discharge. A low pressure is also desirable to ensure that the sputtered atoms have the longest possible mean free path. This acts to reduce the number of collisions between the target and the substrate. This is important since collisions scatter the sputtered neutrals, reducing the number which arrive at the substrate and their energy when they do.

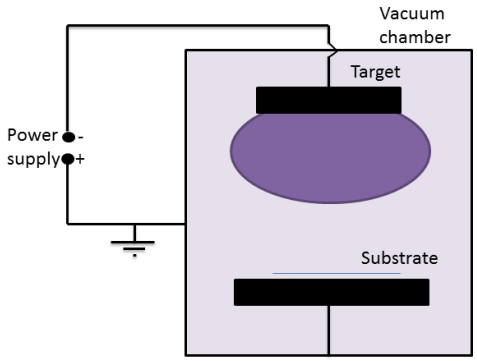

Fig. 2.3 A diagram showing a simple glow discharge.

These glow discharges had low deposition rates due to their low plasma density. The pressure also had to be kept high, relative to modern PVD sputtering, as the plasma confinement was low, further reducing film growth.

In order to increase n_e, the ionisation rate must be increased. The best way to achieve this is to confine the ionising, high energy secondary electrons in the plasma for as long as possible. In a glow discharge, the only thing keeping the secondary electrons from leaving the plasma is the short mean free path resulting from the high pressure. For reasons previously discussed, charged particles will follow magnetic field lines if their gyro-radius (and gyro-circumference) is small compared to the mean free path, the distance to the chamber wall and the divergence of the B-field. A glow discharge with a magnetic field can then be designed from these criteria. A B-field, configured so that the high energy secondary electrons from the target are contained, thereby giving them more time in the plasma, was developed into the magnetron.

2.3 The magnetron

In order to raise the ionisation rate, the high energy secondary electrons given out at the target must be trapped. The easiest way to do this is to use a magnetic field in the target region, with sufficient magnitude to confine the ejected secondary electrons. In this way, the secondary electrons can be confined close to the target, which means that the ionisation rate (and therefore plasma density) is highest where it is needed the most, close to the target. This high rate of ionisation has a secondary positive effect because the increase in ionisation leads to more ions incident on the target. This results in more secondary electrons, thus further raising the ionisation rate and deposition rate.

The use of magnetic fields in glow discharges leads to an increase in n_e and deposition rate, and it also allows the magnetron operation to occur at lower pressures. This is because the system no longer requires a short mean free path to ensure secondary electron collision before they leave the chamber.

The typical magnetron has a magnetic field of the order of 100 mT at the target surface, which decreases as we move away from the target. At this field strength, the thermal electrons' gyro-radii is of the order of ~ 1 mm meaning the thermal electrons, and more importantly the high energy secondary electrons, are considered magnetised, confining them close to the target. Ions, due to their lower energy and higher mass, are not magnetised.

There are many potential designs of the magnetic topology; however the most common is the one used in the magnetron, a (mostly) circular set of magnetic field lines from the centre to the diameter [8]. This magnetic field configuration is shown in figure 2.4.

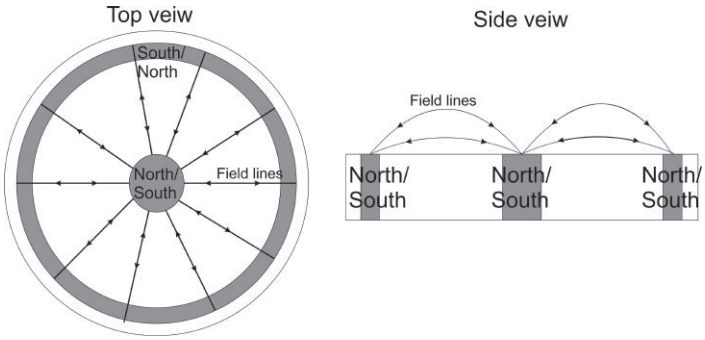

Fig. 2.4 A top and side view of the magnetron with field lines. Magnetrons with both a north at the centre and a south at the edge and a south in the centre and north at the edge have been have been used; the direction of the magnetic field lines do not matter.

The magnetron design has an additional advantage due to the closed E cross B (ExB) drift. A charged particle such as an electron will have its motion dictated by the electronic and magnetic fields applied to it. In the case of perpendicular magnetic ($\overline{B}$) and electric ($\overline{E}$) fields, charged particles move in the $\overline{E} \times \overline{B}$ (cross product) direction. The ExB drift can ultimately be considered as an effect of the E-field acceleration changing the gyro-radius of the charged particle. Therefore only particles which perform gyro-rotation in the magnetic field will be subject to the ExB drift. The ExB drift can also be referred to as the Hall current. It can be seen that for an alignment of E and B fields like that in figure 2.4, the Hall current is closed. This means that electrons stay in the ExB drift indefinitely; the ions do not perform gyro-rotation and so do not travel in the ExB drift. The Hall current can therefore become extremely large, up to an order of magnitude higher than the target current [54], so will be highly ionising. The area directly below the ExB drift has the highest deposition rate and is known as the racetrack.

For the reasons above, the magnetron has a far higher deposition rates at lower pressures than the glow discharge and has therefore replaced it as the main method of plasma sputtering deposition .

The magnetron can operate at pressures between 10 and 0.1 Pa, and it can be supplied by DC, RF or pulsed DC power. The deposition rate in magnetrons is given by equation 2.25. This is derived from the fact that the deposition rate D_r is proportional to the incident ion energy to the power half [55] (proportional to $V_d^{\frac{1}{2}}$, the discharge voltage to the power half) and the discharge current (I_d) to the number of incident ion, where C_d is an arbitrary

constant.

$$D_r = C_d I_d V_d^{1/2} \tag{2.25}$$

Both V_d and I_d can be increased or decreased by changing the power supplied to the target. Plasma conditions such as pressure also have an effect on V_d and I_d; higher I_d at higher pressures.

2.4 High power impulse magnetron sputtering (HiPIMS)

The magnetron target can be supplied with power as either a continuous DC supply, an RF signal or as pulsed DC. Normal pulsed DC has a duty cycle $\sim$50 % with on-times and off-times approximately equal. The averaged power is the limiting factor in magnetron discharges; if the power becomes too high the target may arc or melt. Therefore, by reducing the duty cycle, the on-time power can be higher. The extreme case of this is high power impulse magnetron sputtering, called HiPIMS.

HiPIMS was first proposed by Kouznetsov et al [14] in 1999, and it is the highest power (0.1 - 10 kW cm^{-}2) and lowest duty cycle (0.1 - 5 %) of the pulsed DC discharges. With pulses so short and of such high power, the HiPIMS discharge is considerably different to that of DC or pulsed DC sputtering. HiPIMS was primarily intended to increase the ionisation rate to the point that even the sputtered neutrals become ionised, so as to produce ionised PVD (IPVD) [24]. HiPIMS does have the disadvantage of lower deposition rate then for a normal DC sputtering magnetron; however IPVD is advantageous to film deposition for reasons that will be described later.

HiPIMS discharge

While the magnetic field and target in HiPIMS are the same as in normal DC magnetrons, the way that the power is applied leads to a very different discharge. Part of this is due to the effect of the high ionisation rate of the sputtered flux [16]; however there are other effects present such as rarefaction [56] [57]. This sub-section focuses on the pulse cycle of HiPIMS.

The power in HiPIMS is delivered as a series of pulses of pulse length t_{on} and frequency f where $t_{on} \times f$ gives the duty cycle as a decimal ($t_{on} \times f \times 100$ for percent). The typical t_{on} is of the order of $\sim$100 μs with frequency of repetition changed so as to keep the duty cycle low. This normal operation leaves a long off-time between pulses, where no power would be applied. During this off-time, there is no ExB drift, because of the lack of an E-field.

Therefore the plasma density decreases in the off-time [33]. If the off-time is too long, then the plasma density may be so low that the plasma cannot ignite at the beginning of the on-time. To avoid this, a pre-ioniser, or simmer source (low power), which maintains a low density plasma during the off-time, is often used [58]. Let us assume for this section that there is an initial, low density plasma, either left over from the previous pulse or maintained by the pre-ioniser.

The average on-time V_d and I_d is higher in HiPIMS than in the DC case. The sudden high voltage of the target has the effect first of causing the plasma to become very negative [59] [60] [61]. In addition to this, there are large number of high energy non-thermal electrons (secondary electrons) in the plasma with energy up to 100 eV during this initial stage [33]. This phase, where plasma density is still low, lasts for approximately the first 10 μs of the pulse.

Soon after the start of the pulse, exactly how soon will depend on factors like pressure and power, the plasma density begins to increase rapidly because of the increasing ionisation as the hot electrons become trapped in the ExB drift. This in turn increases deposition rate and secondary electron production. This rapid increase in n_e is accompanied by an increase in I_d (current ramp) [62] [33] [63].

It might be expected that this current ramp would continue until the end of the pulse or until I_d grows so large that it cannot be sustained by the power supply. While this can be the case [64] [65], in general it occurs only at lower powers and for shorter pulses, or for extremely high powers. However for a typical pulse, the current ramp is not indefinite, but reaches a peak after which it decreases [66] [58]. This current drop-off is due to a lack of available neutrals [66] [67]. The high power causes heating and the high deposition results in a high sputter-wind (high flux of sputtered atoms) which causes the neutral gas density at the target to decrease to the point it limits the I_d [10].

Taken together, this leads to the general pattern of HiPIMS discharge, namely: 1) a negative plasma with a low density and small population of hot electrons 2) a sudden current ramp and increase in n_e 3) a peak current after which I_d decreases primarily due to lack of neutrals. The post-peak behaviour of the discharge will be dependent on the level of self-sputtering.

Ionised sputter flux

The very high power in HiPIMS causes extremely high ionisation rates, to the point that the sputter flux, which is normally comprised of neutrals becomes ionised to a high degree

[16] [15]. For this reason, HiPIMS can be used for IPVD [68] [24], though this high rate of ionisation can also lead to other effects such as self-sputtering [69].

IPVD

Since its creation, HiPIMS has been known to generate high rates of ionised sputter flux [14] [66]. Ion bombardment has long been used in the production of thin films [70] [71] [72], . The desire to combine a sputtering technique with inherent ion bombardment is partly the motivation for creating HiPIMS. As ions have a charge, they are affected by electric fields and this allows for greater control of the sample deposition [73]. A common technique is to bias the sample, so that the ions in the sputter flux are accelerated towards the sample. This allows control of the energy with which the ions bombard the film [52]. As discussed in the previous section, the high energy ion impacts allow the production of higher quality films at lower temperatures (zone T). HiPIMS and IPVD has been shown to improve film smoothness, density and cohesion in many studies and reviews, as well as acting to improve sample control through biasing [22] [24] [74] [68] [75].

Self-sputtering in HiPIMS

The high rate of ionisation of sputtered flux in HiPIMS also leads to self-sputtering [76]; where a sputtered particle becomes ionised and is re-attracted to the target, becoming the source of further sputtering. This self-sputtering results in a lower deposition rate in HiPIMS [77] (along with rarefaction [56]). The process of self-sputtering is shown in figure 2.5. Self-sputtering probability can be analysed in terms of two values: α_{ss}, the probability that a sputtered neutral will be ionised, and β_{ss}, the probability that a sputtered ion will return to the target.

The extreme powers in HiPIMS cause a high sputter wind and subsequent rarefaction of background gas [66]. The resulting lack of neutrals eventually leads to a drop in I_d. However this effect can be counteracted by self-sputtering [63]. As $\alpha_{ss}\beta_{ss}$ the probability of a sputtered neutral performing self-sputter must be less than one, so self-sputtering cannot sustain the discharge unless γ_{ss}, the self-sputter yield, is greater than one [78]. If $\gamma_{ss}\alpha_{ss}\beta_{ss} < 1$ in the HiPIMS system, once the background gas has been refracted, I_d will drop due to lack of available neutrals. If $\gamma_{ss}\alpha_{ss}\beta_{ss} \approx 1$, then the discharge will be somewhat stable, maintaining a relatively constant I_d. However if $\gamma_{ss}\alpha_{ss}\beta_{ss} > 1$ the self-sputtering will become runaway and grow exponentially [17] [10] [78].

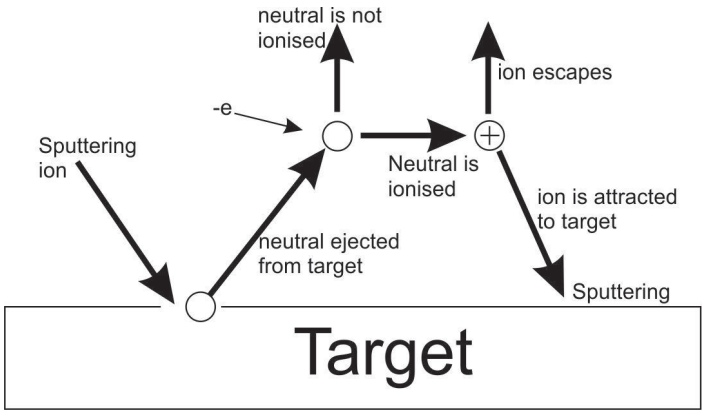

Fig. 2.5 An illustration of a sputtered neutral and paths that can be taken, leading to self-sputtering.

Runaway self-sputtering in normal HiPIMS operation leads to the I_d increasing exponentially to the point where the power-supply can no longer sustain the draw. However it does open the possibility of a gas-less operation where HiPIMS is run purely though self-sputtering with no need for a backing gas [79] [80].

2.5 Spokes

Spokes were first observed in 2011 by Kozyrev et al [81], who observed the target during the on-time of a HiPIMS discharge using a fast imaging camera which was able to take images with a exposure time of 1 μs. Inhomogeneities around the racetrack were observed during the pulse, and they were found to be rotating in the ExB direction [82] with velocities of $\sim$10 km s^{-1}. Anders et al [31] later used imaging with shutter speeds varied between 25 μs and 5 ns and found these same inhomogeneities could be observed at shutter speeds $< \sim$1 μs. The inhomogeneities observed were likened to spokes, similar inhomogeneities seen in Hall thrusters [83] and other systems with an ExB discharge[84]. Since their discovery, spokes have become an area of considerable interest in HiPIMS research.

Theory of spokes

The theory of spokes presented here is largely based on a set of papers on spokes by Anders et al [31] [85]. While many modifications have been made to this theory, it remains the basis for spoke theory [86].

Since spokes were first observed as images of high optical emission intensity, it has been proposed that they represent regions of high plasma density, with a positive charge relative to

the surrounding plasma. As in a normal magnetron, the ionisation in HiPIMS is driven by the high energy secondary electrons trapped in the ExB drift. As plasma density in a specific region of the track increases, the likelihood of the electrons causing an ionisation reaction in that region also increases. This is because, in these regions of high plasma density, there is a shortened electron mean free path [48] [31] and therefore a higher ionisation rate. The system is therefore in a state of positive feedback, where regions of random high density increase in density to form the inhomogeneity observed in the images. Significantly for this study, it is also proposed from observations that the spokes have a higher plasma potential than the surrounding plasma.

Spoke density growth cannot continue indefinitely; eventually the ionisation in the spoke reaches a peak where the spoke ionisation is near 100 % and all neutrals have either been ionised, or rarefied by heating [87] [84]. This results in the spoke dissipating in this area. The spoke's motion is thought to be caused by the secondary electrons moving in the ExB direction creating new regions of runaway ionisation. The region of ionisation though moves an order of magnitude slower than the electrons. The lower spoke speeds compared to the secondary electron speed is due to the fact that ions need to vacate the spoke region and reach the target to produce more secondary electrons.

It should be noted from this that spoke motion and velocity are therefore not a motion of a physical plasma, but a group velocity as the plasma density at each region on the target increases and deceases.

Modifications to spoke theory

As mentioned, modifications have been made to the theory of spokes first proposed by Anders et al [31] [85], and the most important suggested modifications for our purpose are discussed below.

Critical ionisation velocity (CIV)

Studies of spokes with different target material and backing-gas found that the critical ionisation velocity (CIV) of the materials used is closely correlated to the spoke velocity [88].

The CIV, v_{CIV}, is given by equation 2.26 (values in equation 2.26 are as previously defined) and is the relative velocity at which a gas and plasma can pass through a magnetic field where significant ionisation occurs. It can be seen from equation 2.26 that if gas and plasma interact with a relative velocity of v_{CIV}, then a stationary plasma electron in the

plasma's rest frame will have the energy to ionise a gas neutral, which is stationary in the gas's rest frame. This means the ionisation of the gas will be very high.

$$v_{CIV} = \sqrt{\frac{2eE_{iz}}{m_i}} \tag{2.26}$$

The link between CIV and the spokes' velocity has been discussed in many papers [89] [87] [90] as a close correlation between the CIV of the target material or the backing gas and spoke velocity has been observed. A correlation between CIV and spokes has also been observed in other spoke systems, such as the Homopolar discharge, where the gas CIV acts as a spoke speed limit [88] [91].

Brenning et al [84] combine the main spoke theory [31] [85] and the spoke theory of the Homopolar discharges. This newer theory requires electron heating in the spoke to balance the spoke's charge. This heating has a threshold for spoke velocity related to v_{CIV}. This theory also requires ions to be reflected by the spoke explaining asymmetrical planar output [92] [93].

Spoke tails

Spokes have been observed by fast imaging as having two distinct tails, e.g. ends. This results in two apparent spoke shapes. Either the spokes can end suddenly giving the spoke a triangular shape [94] or end gradually, mirroring the build up and giving the spoke a round (diffuse) shape [39]. It was proposed by Hecimovic et al [38] that this difference is the result of secondary electrons. Depending on the work function and the ionisation energy, some metallic ions are unable (or less able) to produce secondary electrons, due to their lower E_{iz}, see equation 2.24. As secondary electrons are needed to continue the spoke, it is argued that once the backing gas has been rarefied or fully ionised, the sputtered target atoms are the only available source of neutrals. The spoke will therefore end rapidly, producing a triangular shape if the target neutrals cannot produce secondary electrons. However if the target neutrals can produce secondary electrons, then the discharge can sustain itself a little longer and the spokes will have a diffuse tail. However they will still ultimately end, as the self-sputtering cannot provide neutrals indefinitely.

The secondary electron yield cannot be the only factor in spoke shape however, as niobium has been observed to produce both diffuse and triangular spokes [38] [87].

Spokes at low powers

Spokes have been observed in magnetrons at multiple powers and pressures, which are not limited to the HiPIMS region. Anders et al [95] observed inhomogeneity around the racetrack at DC currents from $\sim$10 mA, and a more in-depth investigation was later carried out by Panjan et al [96]. The discovery of spokes at lower powers would imply that any effect in HiPIMS attributed to spokes would also be observed at lower powers; however they are not. This suggests that the DC spokes are not exactly the same as the HiPIMS spokes.

This argument is supported by the fact that low power spokes have been observed to rotate in the -ExB direction [37] at velocities far below the CIV and may even be quasi-stationary [97].

Electron flares

Spokes have been associated with heating mechanisms and electron flares since their discovery [81]. Furthermore, since then many images of spokes have identified electron/plasma flares emitted perpendicular to the target from the spoke [31] [94] [98]. The source of these flares has been theorised as secondary electrons from the target [98] and electrons accelerated though the pre-sheath [99]. However the leading theory proposed by Anders et al [100] is that they are electrons accelerated out of the positively charged spoke.

The relationship between spokes and high energy ions

One of the major areas of interest in the study of spokes is their link to high energy ions observed in HiPIMS but not in the DC case [25] [10] [101]. A link between these high energy ions and spokes was first implied by Anders et al [102] who observed that ion energies given off in the plane parallel to the target surface were higher when facing the racetrack into the ExB drift than into the -ExB drift. This work was later developed by Panjan et al [28], who did both flat probe and mass spectroscopy analysis on the ExB and -ExB output to show a higher ion energy and flux given off in the ExB than the -ExB direction.

From observation, it was proposed that the spoke itself is a region of positive potential due to its high ionisation rate. This positive potential must be sheathed both at the front and back, giving the spokes a 'double sheath' (in azimuths direction around the race track) [102] [87]. Brenning et al [84] proposed that to maintain charge in the spokes, some plasma ions entering the spokes must be ejected. While this would explain the existence of the high energy particles given out to the side, it does less well to explain the presence of high energy particles given out in the target-facing direction.

To develop these ideas, the theory was expanded so that the double sheath of the spoke is also theorised in the z-direction (coming out of the target perpendicular) [29] [103]. This double layer, possibly forming a triple layer depending on the interaction with the existing target sheath, was proposed by Maszel et al [29] as the mechanism responsible for the high energy ions seen in HiPIMS. This is because the ions created in the spoke will be accelerated to the substrate though the spoke charge. This theory has been supported by other work from several sources [103] [23] [28].

Spoke conditions

Spokes have been categorised as existing over a variety of powers and pressures [39]. The effect of different powers, pressures and target conditions on the spoke mode number (number of observable spoke on the target) was studied by de los Arcos et al [36], who noted that changing spoke conditions affect the discharge I_d V_d

Work by Poolcharuans et al [90] and Breilmann et al [23] found three distinct regions of spokes at different discharge conditions. At lower power and pressure, spokes were chaotic and lower amplitude in nature; spokes in this regime are known as 'chaotic' or 'stochastic'. As the power and pressure increase, the spokes became regular and periodic, this is the true spoke regime, sometimes known as the 'coherent' regime. However if the power and pressure were increased sufficiently, the spokes disappeared, and this can be called the 'homogeneous' or 'spokeless' regime. These changing conditions have an effect on the ion energy [23] and deposition rate, as well as on the angle of deposition [104].

2.6 Summary

The first part of this review covered basic plasma physics, for a plasma where the ions are considered non-thermal. Relative to important plasma values such as V_p, T_e and n_e, the plasma reaction to an applied charge or at a surface was calculated. Understanding of these relationship will allow the development of plasma diagnostics.

A brief history of plasma vapour deposition was given as well as sputtering and the process behind the development of the magnetron. In addition, theories of important phenomena such as secondary electrons and sputter yield have been explained.

The section on HiPIMS explains some of the relevant effects associated with HiPIMS; the ionised flux, the self-sputtering and refractions are explained. This is done with the hope the reader will understand the known HiPIMS phenomena.

The final section discusses spokes. The main area of investigation in this study, this section included the current theory of spokes, and recent modifications: the spokes' relationship to high energy ions and the variability of spoke conditions.

Chapter 3

Experimental systems

3.1 Introduction

This chapter will list the core components of the two experimental setups. The majority of work in this study was conducted on the system one setup, and in the next section, the chamber, power supply and magnetron are detailed. The system one setup was housed in the Department or Electrical Engineering and Electronics at the University of Liverpool. While the majority of experiments were conducted on system one it was not possible to use imaging technique on system one. Experiments requiring imaging were performed on a entirely different setup, called system two, located in the Department of Physical Electronics, Masaryk University, Kotlářská, Brno, Czech Republic. The chamber and power supply of system two are detailed in the third section. As this rig was only used for imaging experiments, it is described in less detail.

For both setup rigs only the basic unchanging equipment is described. The diagnostics, which are changed depending on the particular experiment, are described in the next chapter.

3.2 System one setup

The majority of the experiments in this study were conducted using the system one setup described in this section. The basic apparatus needed to create and maintain the plasma discharge are detailed, but the diagnostic apparatus and methods of plasma analysis used in this study are not discussed in this chapter.

The chamber

The chamber is a tube with an internal diameter of 270 mm and length of 300 mm, which is made of aluminium. The chamber houses a circular magnetron facing down the length of the tube, which can be held either in the centre, or off-centre, in such a way that the target racetrack is centred. The magnetron stem is such that the head can be moved forward and backwards, along the length of the tube. Flanges are positioned in such a way that probes can be inserted both perpendicular and parallel to the magnetron target through feedthroughs. The position of these flanges is designed to give the probes good access to the target surface. The flanges are mostly standard MK-25 size and type; however a range of adapter flanges are employed so that all flanges can be attached to any feedthrough. A variety of in-house-built aluminium feedthroughs were used for a range of different diameter probe stems (all tubular in shape). The feedthroughs were sealed by screw tightened O-rings and could be adjusted to move the probe along the axis of the stem without breaking the vacuum.

The flange at the end of the chamber could be fitted to either a probe stem, or a Hiden Analytical Limited EQP300 quadrupole mass spectrometer, in such a way that both would face down the centre of the chamber. There are two gas inflow channels, each controlled by an MKS 1179A mass flow controller, although in this study only the argon line was used. Stopper values are used to seal the gas lines when they are not in use. The system is pumped to a base pressure down to 10^{-4} Pa by an Edwards EXT75DC turbo pump and a 28 litre Edwards E2E28 rotary backing pump. The base pressure is limited due to the use of rubber O-rings on the flanges and feedthroughs. The rubber O-rings have the advantage that they allow the setup to be easily adjusted and allow probes to be moved at vacuum pressures (without the need for expensive bellows systems), but copper gaskets would able to hold a greater vacuum. The chamber schematic is shown in figure 3.1.

Three different pressure gauges are required to measure the pressure accurately, with each specialised for use over a different pressure range. The first, an Edwards Apg100-XJG pirani gauge, is used for pumping as it is able to cover a wide range of pressures from atmosphere to around 1 to 0.1 Pa, but it is not very accurate (± 15 % at > 1 Pa)[105]. The second, a MKS 627A baratron, is used to measure experimental pressure, as it is most accurate in the range 0.01 - 10 Pa, and gives the same results independent of gas (± 0.15 % at < 130 Pa) [106]. The third, an Edwards Aim-X inverted magnetron, is used to measure base pressures, because it is able to measure at pressures < 0.1 Pa although these measurements are relatively inaccurate (± 25 % depending on gas) [107]; for this reason it is only used to give an order of magnitude of base pressure. The inverted magnetron creates plasma, which could interfere with the experiment, and so it must be turned off after the base pressure is found.

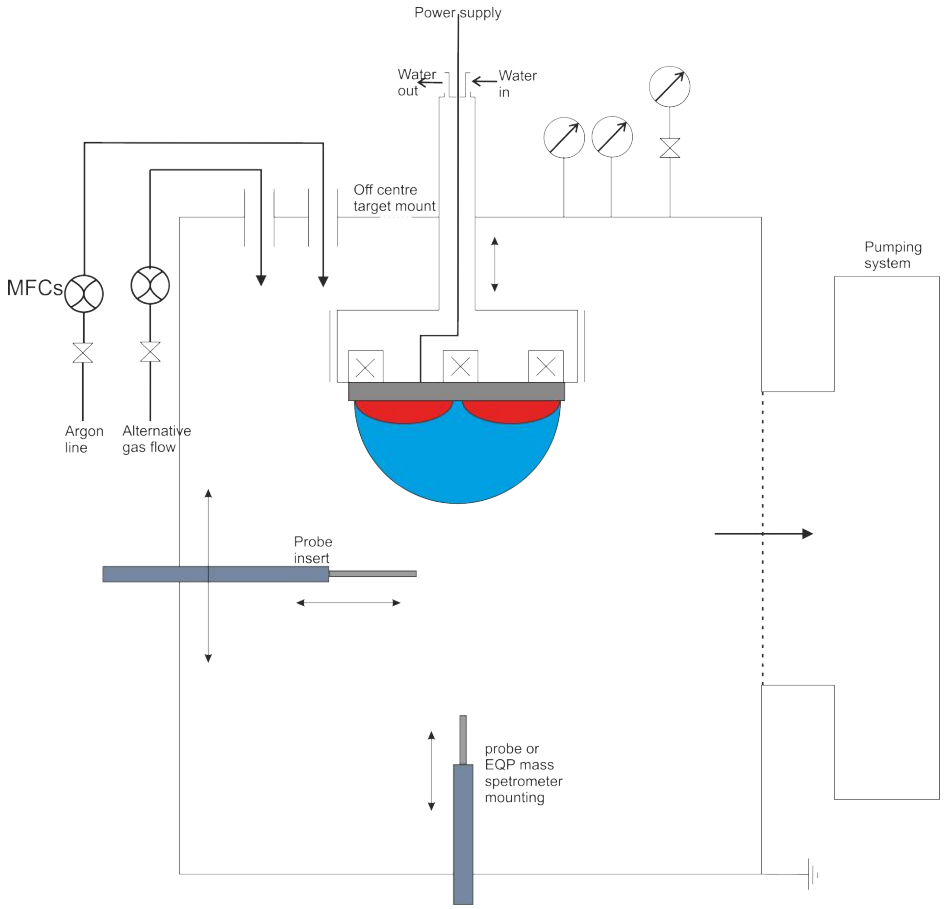

Fig. 3.1 General schematic of the magnetron chamber setup for the magnetron in the centre of the chamber (Off-centre mount shown), with both probe insert positions and their mobilities shown. The gas flow pressure lines, magnetron and pressure gauges are also shown.

All pressure gauges are connected to the chamber by sealed tubes which are no longer than the chamber length, with their thinnest point on the instrument itself to ensure that there is minimal pressure discrepancy.

The power supplies

Power could be supplied to the magnetron by a range of supplies listed below. Each power supply connects through a junction box with two inputs, each of which pass through a diode to prevent the power running from one supply into the other. Both inputs can be fed to the magnetron simultaneously. The current and voltage through this junction box are measured by a Tektronix P5100 voltmeter and a Pearson 3972 current monitor connected to an Oscilloscope.

When operating in HiPIMS, the current and voltage to the target are monitored by the oscilloscope. When DC mode is used, an alternative current probe must be used, a Tektronix TCP202, or the power-supply's internal current and voltage monitoring system. This setup is shown in figure 3.2.

A total of five power supplies were available for use in any experiment; two for DC power, one pre-ioniser and two HiPIMS supplies. They were:

- Two DC power supplies.
  - An Advanced Energy, Pinnacle 18 kW supply, capable of delivering both constant and pulsed DC.
  - An Advance Energy MDX 1.5 K capable of delivering DC power.
- A Flux 415B low power DC supply, used as a pre-ioniser/simmer source.
- Two HiPIMS supplies, both of which were in-house builds.
  - Power supply (A) which was used at lower average and pulse powers. This power supply has a 5.5 μs delay between the start and the trigger.
  - Power supply (B) was able to provide higher average and pulse powers.

As both HiPIMS power supplies are home-made, a brief description of their discharge profile is appropriate. Because the power supplies are home-made, they find it hard to maintain a constant voltage so V_d drops during the current ramp, as can be seen in figure 3.3. Although this effect can be seen in all the figures, it is most noticeable for power supply A Similar voltage drops have been reported for the power supply in several papers [36] [29]. The current drawn by the supply is not fixed, but dictated by the plasma. The current-voltage curves seen in figure 3.3b and c are similar to the ones described by A. Anders [17] and others [24]. The explanation for this curve is fully outlined in the literature review, chapter 2.

The effect of the pre-ioniser on the power supplies can be seen in figure 3.3b and c. Even in conditions where the pre-ioniser was not necessary for the plasma to ignite, its absence still caused a delay in the start of the pulse. This meant that the rest of the pulse had to be of a higher power to reach the same average power. Power supply A has a 5.5 μs delay between the trigger and power activation; this fact is taken into consideration when power supply A is used.

Both power supplies used external triggers, an Agilent 3210A signal generator, to define the pulse length and repetition rate. This signal generator was more accurate than the power supplies' internal trigger. Oscilloscopes and other instruments used to monitor the plasma

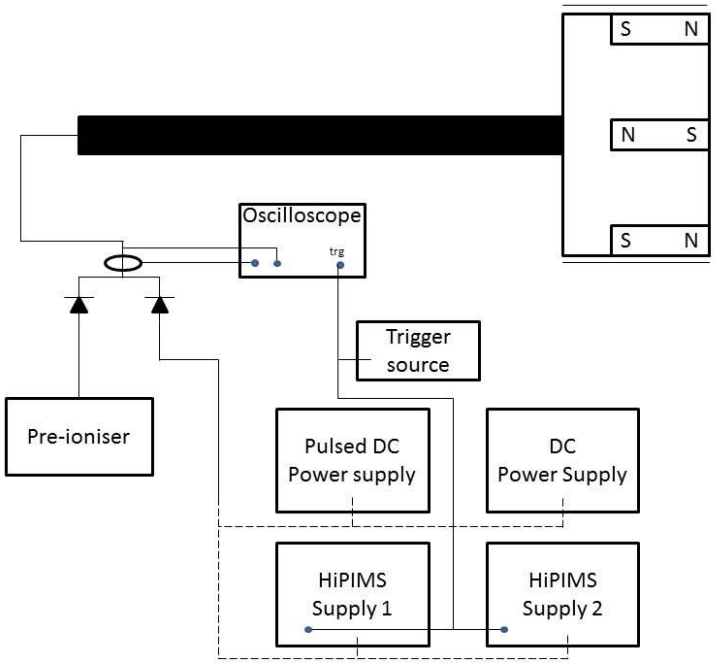

Fig. 3.2 A simplified block diagram illustrating a power supply circuit, including all power supplies, the oscilloscope, the triggering system and the magnetron.

were also triggered from the same source. When this is done, care is taken to ensure that the pathways to all instruments are of the same length.

Power calculation

Because power in HiPIMS is delivered as a series of pulses, reporting the power requires knowledge of several factors. Throughout this study, the power or energy of individual HiPIMS pulses as well as the average power of a series of pulses will be discussed, and it is important to distinguish between these different values. In general, power is the product of voltage and current, and this holds in the case where the current and voltage have a time dependency, as they do in figure 3.3. Therefore for a pulse, the average power during the pulse (P_p) is given by equation 3.1, where t_{on} is the pulse length and I(t) and V(t) are the current and voltage time traces respectively.

$$P_p = E_p/t_{on} = \int_0^{t_{on}} v_d(t) I_d(t) dt / t_{on} \tag{3.1}$$

This value (P_p) for the average on-time power and the average pulse energy E_p ($E_p = t_{on}\ P_p$) is useful when discussing single pulses. However for normal operations, multiple pulses

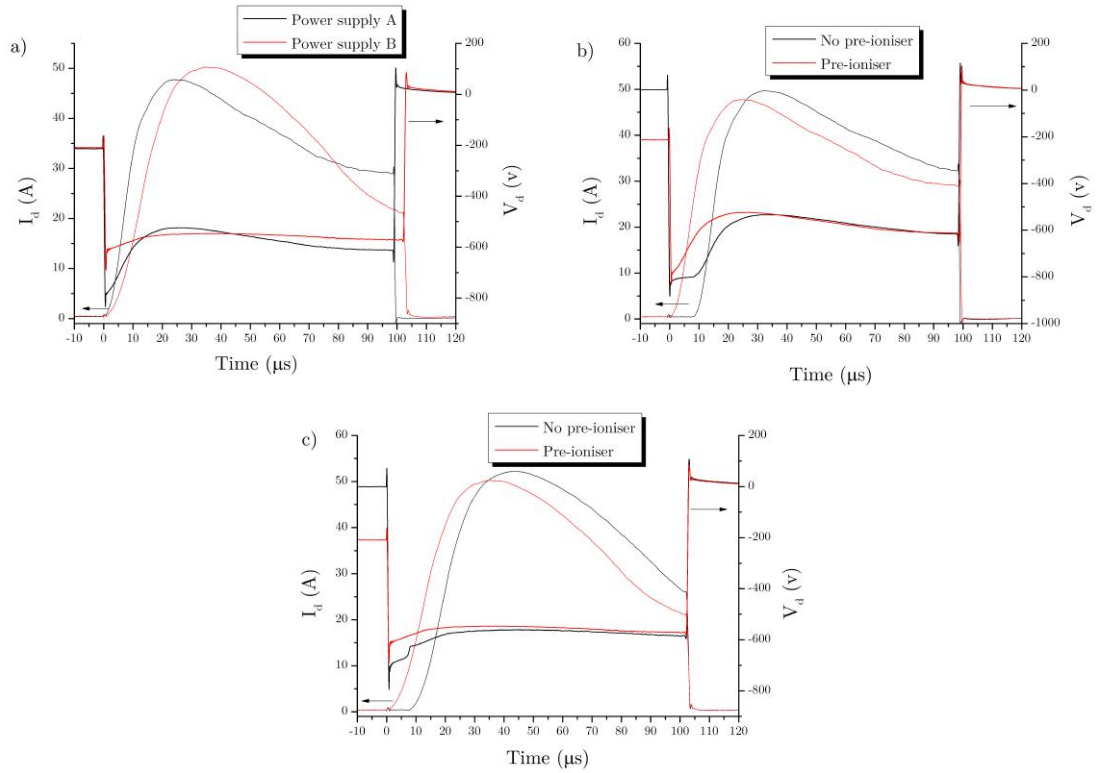

Fig. 3.3 The current-voltage discharge for a 106 μs, 50 Hz, 0.67 Pa pressure, E_p = 1 J pulse, with a niobium target. a) both power supplies compared, with the pre-ioniser on, with power supply B shifted so both start at the same time. b) power supply A with and without pre-ioniser starting at 0 μs. c) power supply B with and without pre-ioniser.

make up the discharge so additional information is needed to compare HiPIMS to the DC case. Normally, the average total power P_A is reported, as this is most easily compared to the DC case. P_A's value is given by $P_A = f \times E_p$ or $f \times P_p \times t_{on}$, where f is frequency.

However only presenting P_p and P_A is not enough information, so either f or t_{on} must also be presented. For example it is apparent that a discharge with t_{on} of 10 μs and frequency 500 Hz could P_p and P_A equal to that shown in figure 3.3, yet have very different discharge properties. Normally E_p is given; reported with f and t_{on}, P_A can be easily calculated if needed.

The power from the pre-ioniser P_i very small compared to P_A, the average HiPIMS power, and therefore the effects of the pre-ioniser are not considered when calculating P_A

The magnetron

The magnetron itself uses a 76.2 mm (3 inch) diameter, 6.35 mm (1/4 inch) thick target held in place by a 3 mm raised guard ring. The magnetron is a type-1 unbalanced field that is

50 mT strong in the radial direction at the target surface, just above the racetrack. All the experiments presented used a non-magnetic target.

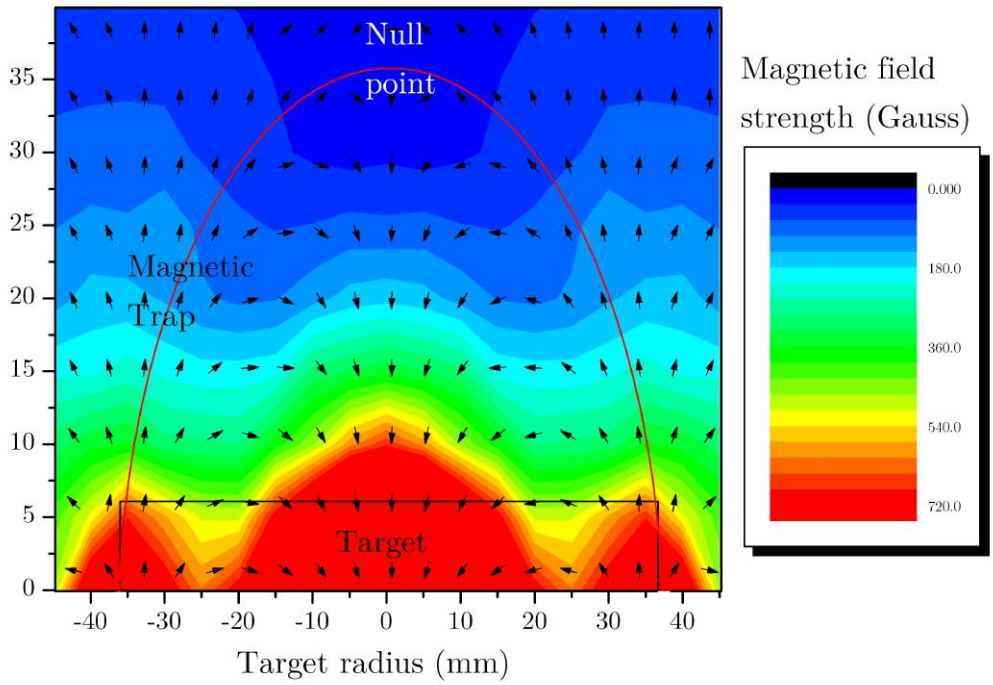

Fig. 3.4 The magnetron field with the target, magnetic trap and null point all marked.

The magnetic field up to the null point is shown in figure 3.4. It is measured by a GM07 Gauss-meter with a TP002 Hall probe along a major axis of the magnetron where zero represents the centre. The results at height 40 mm were interpolated from previous results, as the Hall probe became inaccurate. The mapping was done in the target and radial directions and both have a spatial resolution of 5 $\pm$1 mm. The magnetic field is measured to an accuracy of $\pm$ 10 Gauss. The values of the magnetic field, shown in figure 3.4, were measured without the target, the guard ring or the grounding anode. The target's position is indicated in figure 3.4, as are the limits of the magnetic trap, defined as the last closed magnetic field line, shown as a red line, and the null point.

A grounding anode is a ring consisting of a 5 mm thick metal tube surrounding the guard rig of the magnetron; a 3 mm gap separates them. An anode is used so that the magnetron has local grounding. Normally the anode is levelled so that it is flush with the guard ring; however it can also be drawn back if this is necessary. Note that so doing does not significantly affect the discharge. The magnetron is kept from overheating by water-cooling at a rate of 1 l

min^{-1} kW^{-1}. The race track, assumed to take the majority of the target current, is centred at 22.5 mm.

3.3 System two setup

The majority of experiments reported in this study were performed on the system one setup already described. However, some of the experiments required imaging and these were performed on the system two setup, a separate imaging rig in the Department of Physical Electronics, Masaryk University, Kotlářská, Brno, Czech Republic. This imaging rig is described in this section.

The chamber and magnetron

The system two chamber was an Alcatel SCM 650 magnetron sputtering system, housing a 75 mm diameter circular magnetron (Kurt J. Lesker) fitted with a niobium target of 99.95 % purity (Testbourne Ltd). The total magnetic field strength above the 1 mm racetrack was measured to be 72 mT using a Hall probe MI 2010T (Magnetic Instrumentation Inc.). The deposition chamber was pumped by a turbo-molecular pump backed by a Roots pump to a base pressure below 10^{-4} Pa. The pressure was measured using both a Capacitance Baratron MKS gauge and a PKR 251 compact full vacuum range gauge (Pfeiffer Ltd). Argon gas with 99.999 % purity was supplied to the vessel at a flow rate in the range of 1 – 140 sccm (standard cubic centimetre per minute) to provide working pressures of 0.14 – 5 Pa. A metal substrate holder was positioned 4.5 cm from the target although no coatings were made using this rig.

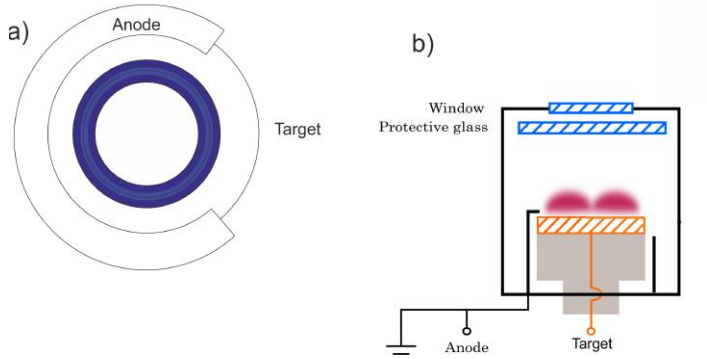

Fig. 3.5 The target and anode showing the cut away section from both a) the target facing view and b) the cross section view showing the whole chamber.

The outer anode shield of the magnetron shield is shown in figure 3.5. Part was cut away, as shown, to allow the probes access to the target surface; specifically for the strip probes described in chapters 4 and 5. This removal of the anode shielding had a minimal effect on the discharge. However the optical images in the vicinity of the cutaway section dropped; a 15% drop in the intensity of the optical emission signal, compared to the rest of the target.

The power supply

The discharge was driven by a dual-channel Melec SIPP 2000 HiPIMS generator, capable of providing peak discharge currents of up to 500 A and voltages up to -1000 V. The output cables from the generator were looped nine times through a ferrite ring to suppress fast high-amplitude oscillations that could damage the pulser. In addition, an Auxiliary Dressler Cesar 500 radio frequency (13.56 MHz) generator with mean power of 20 W connected to the substrate holder is used as a pre-ionizer. RF matching was adjusted to maintain the reflected power below 2 W.

The waveforms for the total discharge voltage and discharge current were measured using a measuring system integrated into the Melec generator, in which cathode voltages and currents in the range 0 – 1000 V and 0 – 500 A respectively were displayed as voltage signals in the range 0 – 10 V. These readings were recorded using a Keysight Infiniium DSO-S 204A oscilloscope working in single shot mode with 4 ns sampling interval. An example is shown in figure 3.6, for E_p = 15 J and pressure 0. 25 Pa for a 200 μs pulse, 5 Hz. The differences between the discharge in figure 3.3 and figure 3.6 are probably caused by the differences in magnetic field strength and grounding. The perturbations in the frequency range $\sim$1 MHz seen in the I_d and V_d do not significantly affect the discharge and have been observed in other systems [29].

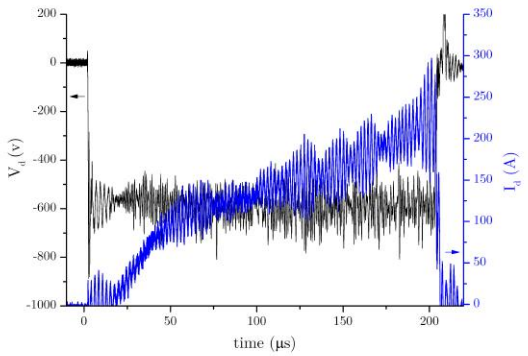

Fig. 3.6 The discharge current I_d and voltage V_d for the imaging rig discharge at 0.25 Pa, $E_p = 15$ J, 5 Hz and a 200 μs pulse length, with a niobium target.

3.4 Summary

This chapter describes the rigs used in all subsequent experiments. System one, is a moderately size chamber which can be pumped to a reasonably low base pressure of 10^{-4} Pa. Inside the chamber is a type-1 unbalanced magnetron with a 76 mm diameter target. The magnetron can be supplied by power from a DC supply, a pulsed DC supply and two different HiPIMS supplies, which can be used with or without a pre-ioniser. The chamber was fitted with flanges such that the probes have easy access to the target. While this chamber lacks the high or ultra high vacuum conditions normally used in deposition rigs, its versatility is well suited for performing plasma analysis.

The system two setup has a somewhat different magnetron and power supply to system two, though the systems are not meant to be directly compared. This imaging rig also lacks the high or ultra high vacuum normal used for deposition. However like system one, it is suitable for plasma analysis and, unlike the system one, it is also suitable for imaging.

Chapter 4

Diagnostic techniques

4.1 Introduction

This chapter will explain the workings and use of the diagnostic equipment and techniques developed and used in this study. There are four techniques described in this chapter: the Langmuir probe, the strip probe, the triple probe and optical imaging. The operation of these diagnostics and the readings they are used to obtain is detailed; explanations of the plasma physics involved are given where applicable; and the drawbacks and errors are also indicated.

4.2 The Langmuir probe

Introduction to Langmuir probes

The Langmuir probe is one of the most commonly used plasma analysis devices. This is due to its simplicity and the wide range of plasma parameters it is capable of measuring. The Langmuir probe consists of a thin conductor placed inside a plasma, to which a potential can be applied (V_b). In this study an 0.08 mm diameter 5 mm long tungsten wire is used as the conductor; the rest of the probe must be insulated from the plasma to ensure the Langmuir probe only measures the plasma at the probe tip.

Despite its simplicity, a Langmuir probe system is capable of finding a number of plasma parameters: the floating potential V_f, plasma potential V_p, electron temperature T_e and the density of a plasma n_e. This is done by applying a set of potentials V_b to the probe, and then measuring the current response I_L from the plasma.

Langmuir probe theory

As the Langmuir probe is inside the plasma, its interaction is governed by plasma-surface interactions. The total current I_L to a surface in plasma with bias V_b is given by equation 4.1, where $I_L(V_b)_{V_b>V_p} = I_{esat}$.

$$I_L(V_b) = I_{esat} \exp(e(V_b - V_p)/kT_e) - I_{isat} \tag{4.1}$$

Equation 4.1 is the ideal case. When the $V_b - V_p$ is very negative compared to kT_e/e, I_L = -I_{isat} and when V_b is greater than the plasma potential V_p, $I_L = I_{esat}$. Because ions are far less mobile than electrons, I_{esat} is much larger than I_{isat}. This results in the ideal Langmuir curve, of $I_L(V_b)$ over all three regions (ion saturation region, electron saturation region and the transition region), seen in figure 4.1a.

In the more realistic case, shown in figure 4.1b, there is sheath expansion from both ion and electron sheaths, meaning that I_L continues to increase beyond I_{isat} and I_{esat} as the probe potential increases. Thus, the ideal Langmuir curves plotted from equation 4.1 can be seen in figure 4.1a, while the realistic case is shown in figure 4.1b.

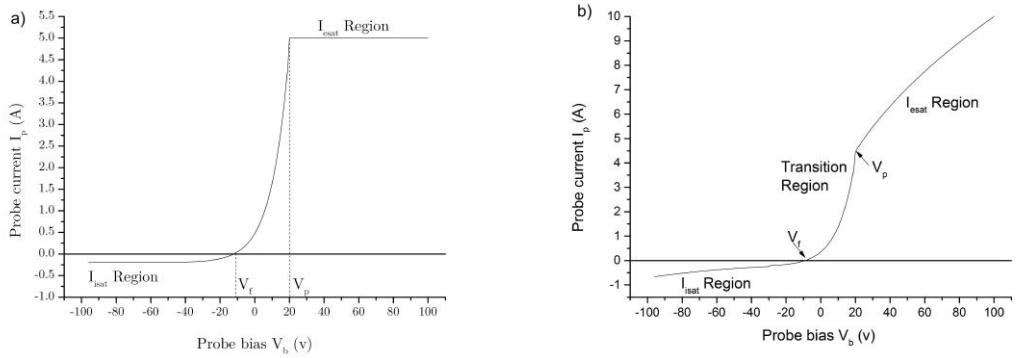

Fig. 4.1 A Langmuir curve drawn from equation 4.1, for the a) ideal and b) more realistic case.

Floating and plasma potential

V_p and V_f are both easily readable from the Langmuir curve in the ideal case. V_f is the potential at which no current flows, and as such is readable in both the ideal and real case. V_p is the point at which I_L changes from being governed by equation 4.1, to I_L the electron saturation region. V_p is easily readable in the ideal curve in figure 4.1a. However in the realistic case in figure 4.1b V_p is obscured, V_p can still be seen; however it may require the use of fitting lines and log plotting to get an accurate value. A better method may be the

differential of equation 4.1. At $V_b = V_p$, I_L changes from being governed by equation 4.1 to being either equal to I_{esat} or governed by sheath expansion. It can be seen from the second derivative of equation 4.1 with respect to V_b ($I''_L(V_b)$) >0 for $V_b < V_p$. For $V_b > V_p$, $I''_L(V_b)$ = 0 for the ideal case or in the case of sheath expansion $I''_L(V_b) < 0$. For this to be possible, $I''_L(V_p)$ must equal zero, making $I'_L(V_p)$ a stationary point.

Ion saturation current

Like V_p, I_{isat} is easily determined in the ideal case, by directly reading the value from the Langmuir curve as can be seen from figure 4.1a. In the real case, this is not possible due to sheath expansion. The normal method is to use a linear fit to model the sheath expansion. This linear sheath expansion model is then extended to V_p, the value at which there is no sheath expansion.

Electron temperature

The T_e is found by modifying equation 4.1; taking I_{isat} from I_L giving the purely electron component of the current I_{Le}. Taking the natural log of both sides of I_{Le} gives equation 7.1, which can be reduced to equation 4.3.

$$\ln(I_{Le}) = \frac{eV_b}{kT_e} - \frac{eV_p}{kT_e} - \ln(I_{esat}) \tag{4.2}$$

$$= mV_b + C \tag{4.3}$$

When the natural log of I_{Le} is plotted against V_b, the gradient m is the inverse of the electron temperature in electron volts as shown in figure 4.2. This is true for both the ideal and real Langmuir case. However in the real case, there may be multiple electron populations, each with different T_e. The more common populations will be found to have higher values of I_{Le}, as higher values of I_{pe} correspond to more electrons collected.

Plasma density

From the calculated values of T_e and I_{isat}, the plasma density can be calculated from equation 4.4. Equation 4.4 is derived in Chapter 2.

$$I_{isat} = en_e\sqrt{\frac{kT_e}{m_n}}A_{eff}\exp[-1/2] \tag{4.4}$$

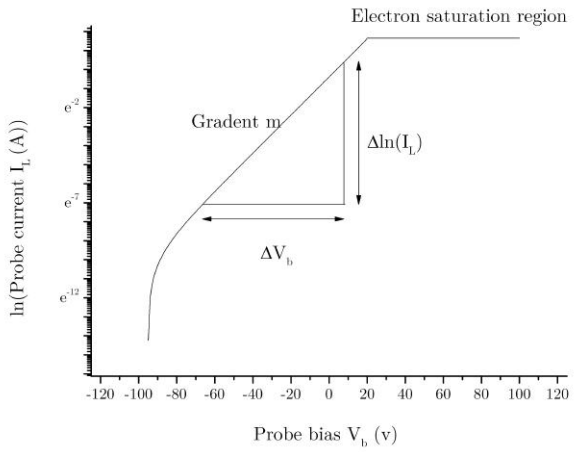

Fig. 4.2 Showing the calculation of T_e for an ideal Langmuir curve, where T_e = 1/m. A real Langmuir curve may have multiple lines, each needing to be fitted to a different m value.

The other major technique to calculate n_i is to use orbital motion limited theory, (O.M.L). However this requires the probe sheath (s) to have the value s >> r where r is the probe radius (4×10^{-5} m). HiPIMS plasma densities n_e have been reported as up to 10^{19} m^{-3} with T_e in the range 1-10 eV. The calculation of s derivations or the sheath width based on n_e and T_e is discussed in chapter 2. However at values of T_e and n_e used in these experiments, the s >> r condition would not be met so O.M.L. is not used.

Langmuir probes: limitations and errors

Limitations

Despite being commonly used, Langmuir probes do have certain limitations. The biggest limitation is the long capture times required by the voltage sweeps. A large number of measurements, each at different voltage points, are needed for an accurate I-V curve; each point has a finite measurement time on the order of microseconds.

This limitation can be avoided for a regularly repeating plasma system such as HiPIMS, by syncing the Langmuir system to the same trigger as the power supply and taking readings over multiple pulses always at the same time within the pulse. However, because readings are made over multiple pulses, the results are, by definition, averaged.

Errors

Values measured by a Langmuir probe, are often calculated from, not only their specific measurement, but also other measured values, each with their own error to calculate. To

simplify the error calculation, once a value and error are reported it is assumed to be absolute in further calculations, with the exception of the calculation of n_e
The errors are calculated from:

- The error in V_f and V_p, which is the V_b voltage step used to capture the Langmuir I-V characteristic.
- I_{isat} is calculated from linear fits so the error is derived from the error in the linear fit's gradient. In the case of I_{isat}, the error in the linear fit's y-axis intercept is also needed.
- T_e is calculated from a $\ln(I_{Le})$ plotted against V_b, this use of natural log distorts the linear error in I_{Le} giving for example asymmetrical error bars. The error is still derived from the linear fit's gradient.
- n_e (and n_i) are calculated from I_{isat} and $T_e^{1/2}$, and the error in both values can be used to calculate the error in n_e.

Given the number of repetitions and the degree of measured error in each measurement, the techniques above will give proportional errors of the order ± 1 %. While this error of $\pm$ 1% is quantifiable there are harder to define sources of error, especially in the case of HiPIMS. The Langmuir probe required averaging over multiple single pulses; however the measured values of different pulses can differ significantly. Other factors can also affect the readings such as variation in measured values over time and as discussed in the introduction, magnetic fields can affect charged particle transport. Estimating the error resulting from these effects is difficult, but a standard error of $\pm$ 20% [108] should be sufficient.

Langmuir probe tip

The Langmuir probe tip is 0.08 mm diameter wire: 5 mm of this wire is exposed to the plasma and the rest is shielded by alumina ceramics for >50 mm (the exact distance can vary) before it is connected to an insulated wire in a metallic probe stem. This 50 mm distance prevents the metallic probe stem acting as a ground and perturbing the plasma.

The main ceramic tube was 1 mm internal diameter so two tubes were needed to step down to the bore size until it provided the 0.08 mm wire with a tight fit. The final ceramic is recessed, which gives the probe tip a longer lifetime in a conduction depositing plasma. This is shown in figure 4.3.

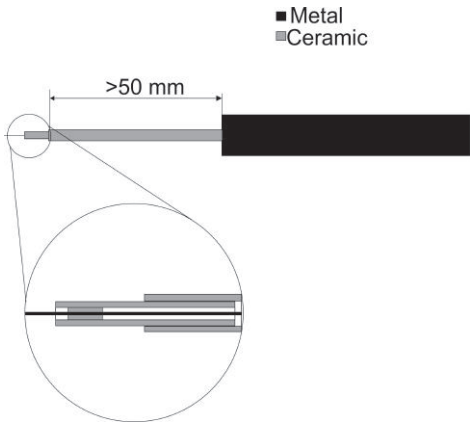

Fig. 4.3 A diagram of the Langmuir probe tip.

4.3 The Strip probe

Introduction to strip probes

The strip probe is a new diagnostic device, first created at the University of Liverpool and presented in a publication by Poolcharuansin et al [90]. The strip probe is a radial section of the target electrically isolated from the remainder of the target, but kept at the same potential. This allows the current drawn from the specific region above the strip to be measured in real time. The strip probe was designed with the intention of studying spokes. Since spokes are regions of high density plasma, they have a higher flux of ions through the target side sheath (equation 4.4), and this increase in flux causes the local target current to increase measurably. The strip probe is able to detect this increase in local current so it can therefore detect spokes and measure the magnitude of the increase in local current for which they are responsible.

Earlier methods of detecting local discharge current were used to measure and compare the radial target deposition profile in HiPIMS and DC discharges [35]. The technique used by Clarke et al [35] was refined with the intention of investigating spokes; more specifically, the increase in local current drawn by a spoke, compared to the 'normal' discharge.

Strip probe operation and design

The strip is a thin bar of width 2 mm, the same thickness as the target, with a length 35 mm fully rounded on one end. This strip is matched by a radial slot, cut into the target of width 2.14 mm, stopping 7.5 mm from the target centre, with a circular end to complement that of the strip. Thin polyimide tape is wrapped around the strip to insulate it from the target, but still allowing connections to be made as shown in figure 4.4. The polyimide tape is 0.07 mm thick so when insulated, the strip provides a tight fit to the target slot, such that it lies

flush with the target. The strip or strips are connected to the same power supply as the target, as shown in figure 4.4. However the supply to the strip is split off after the total current is measured and run through a Pearson 2877 current monitor, so that the current drawn by the strip can be measured specifically .

Multiple strip probes are often used on a single target, even though a single strip can be used to study the I_p drawn by spokes. The normal setup uses three strips each separated by the same fixed angle θ. Using multiple strips allows spokes to be tracked across each strip in turn. Hence the spoke's angular velocity ω can be calculated from the time delay (τ) that it takes the I_p peak to move from one strip to the other at a set angle θ away.

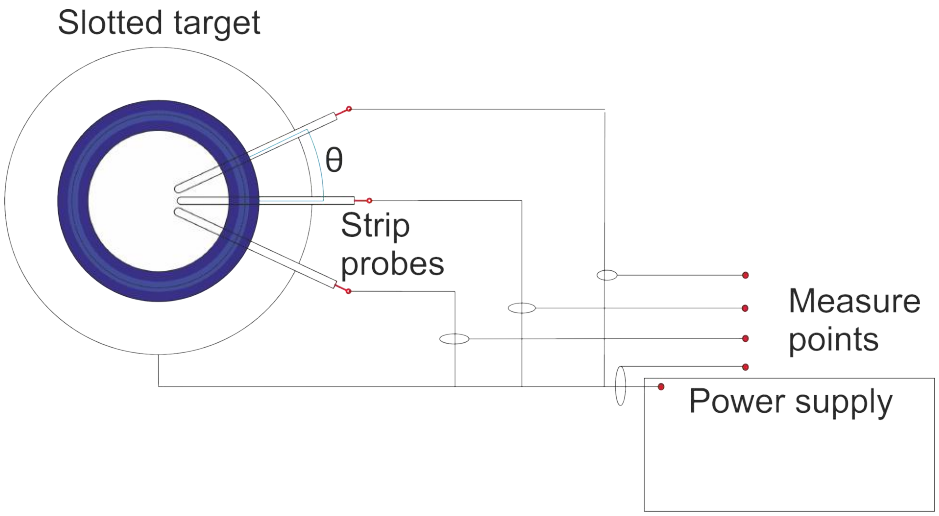

Fig. 4.4 Multiple strips on a single target strip probe connected to the power supply

A target with three strip probes allows us to be sure of the direction of spoke motion; with only two strips the argument could be made for the spoke to be moving an angle θ in one direction or an angle $2\pi - \theta$ in the opposite direction.

From the τ for a spoke to move from one strip to the other, the full spoke rotation period T (T = $\tau \times 2\pi/\theta$) can be found. Using the racetrack radius (r_0) and T, the spoke velocity (v) can be found, using basic mechanics ($v = 2\pi r_0/T$).

Strip probes: limitations and errors

The main drawback of strip probes is their short lifetimes. Due to erosion and re-deposition effects, the strips cannot be used at very high power or for long periods of time as the tape becomes conductive, which renders the strip useless. However the drawback of a short lifetime is offset by the ease with which the polyimide tape can be replaced.

While the polyimide tape does electrically insulate the strip probes, it also insulates them thermally. Rather than cooling the target and strips unevenly, the water cooling is not used with strip probe operation; hence the strips cannot be used at high average powers (P_A), where P_A is power averaged over the full HiPIMS cycle. This requires that the duty cycle and frequency of repetition, f, be low. Therefore a pre-ioniser must be used with the strip in most conditions.

The main source of error in the strip is geometric in nature. Ideally the strip probe would be an infinitely thin wedge. However this is not possible as:

- A wedge shape would not stay securely in place on the target.
- A thinner probe would draw a lower current,
- The probe width (P_d), must be much greater than P_g, the gap between the strip and the target (P_g) where P_g = 0.07 mm.

Both the probes' rectangular shape and thickness create their own sources of error. It should also be noted that the strip probe takes no radial data.

Finally there is a limitation due to the current monitor used to measure I_p. In this study, a Pearson 2877 current monitor was used. This current monitor is accurate to +1/-0 %, with a usable time of 2 ns and able to take a total current time product of 0.4 milliamp seconds, which limits the pulse length [109].

Probe thickness error

The strip width means that, as a current profile passes over a strip, there will be an averaging effect due to the width of the strip. This effect will average the current over a time range given by equation 4.5 where v is the velocity of the phenomena and P_d is the strip width.

$$I(t_0) = v \int_{t_0 - P_d/2v}^{t_0 + P_d/2v} I(t)dt/P_d \tag{4.5}$$

Spoke velocities have been reported as 5-15 km s^{-1} [88] with P_d = 2 mm, which means that the time rounding error is only of the order of Δt = 0.4 - 0.13 μs. This time resolution is similar to that of fast imaging shutter speeds. This will have the same effect as using a moving average smoothing function over a time t = P_d/v. It also means that two objects travelling around the racetrack with a separation less then P_d will appear as one on I_p, the recorded strip probe current.

Probe shape error

The discharge current is assumed to be angularly symmetrical; it follows that the strip should also be angularly symmetrical e.g. wedge shaped. However as the strip probe is rectangular in shape it has a greater area near the inner edge of the target and a smaller area near the outside, compared to a wedge of width 2 mm at the centre of the race track. This is illustrated in figure 4.5 with the rectangular and wedge shaped strips on two targets with different radii racetracks. The total area of the two strip shapes in figure 4.5 is the same; however the different shapes can make a significant difference in the measured probe current, as the outer (from the racetrack) area of the rectangular strip is around 20 mm^2 smaller than the wedged shaped one and the inner (from the racetrack) area is around 20 mm^2 larger than a wedge shaped strip (for a strip 50 mm^2 in area). Figure 4.5 shows two racetracks of different r_0. If the total current through the racetracks are the same, for both the racetrack radii, the wedge I_p would be the same. However the rectangular strip shape shown will give two different values of I_p for the different racetrack radii.

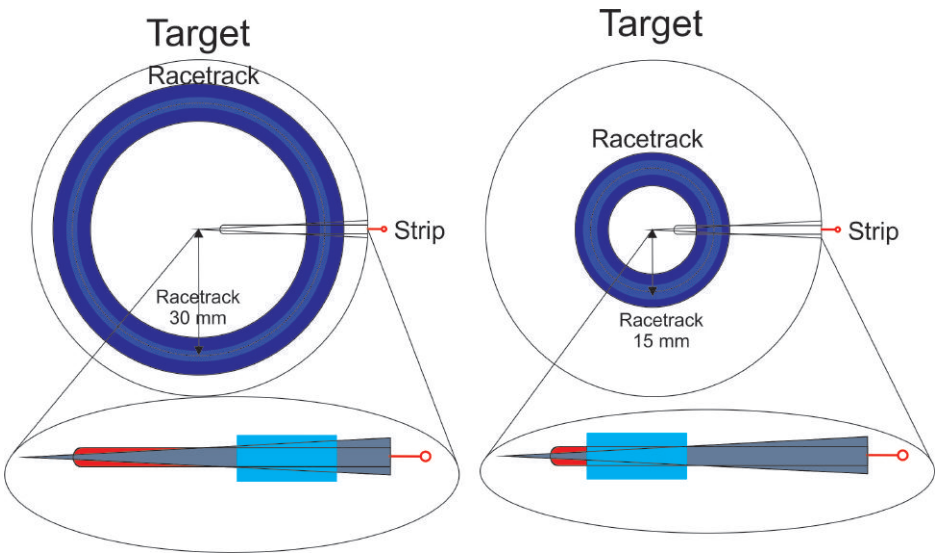

Fig. 4.5 The target with strip probes of two different shapes to show the difference between the wedge and rectangular shape, with the grey wedge superimposed over the red strip. Also showing the effect of two different radii racetracks.

Figure 4.5 is an extreme case. However, because of this effect, the strip probe current signal is normally that represented as a current I_p, rather than a current density. I_p, the current draw by the strip, is therefore an absolute output.

4.4 The triple probe

Introduction

The triple probe was originally proposed by Chen et al [110]. It is designed to be able to take the same range of readings as the Langmuir probe (n_i, T_e and, depending on the mode, V_f and V_p as well) with a time resolution only limited by the plasma response time ($1 / \omega_p$ for a HiPIMS plasma $\sim$1-100 ns), sufficient to investigate spokes. Triple probes are commonly used on systems unable to use normal Langmuir systems, i.e. events with short lifetimes [111]. As the name suggests, a triple probe uses three probes placed within the plasma, separated so that their sheath does not overlap once a bias is applied, but close enough that the local plasma parameter conditions are the same for all probes.

Triple probe theory

A triple probe can be operated in one of two setups, both shown in figure 4.6. The first setup figure 4.6a is known as current-mode; this is where all probes are biased relative to one another and the current is measured. The voltage-mode figure 4.6b has only two probes biased, with the third left floating [112].

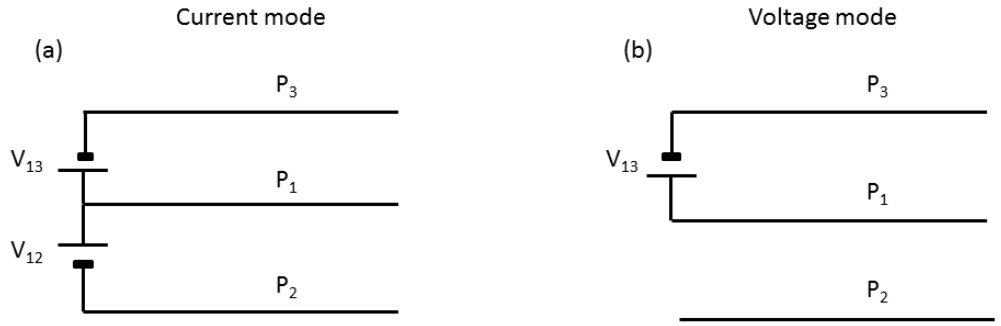

Fig. 4.6 A simplified diagram showing the connections of the three probes in the a) current mode and b) voltage mode of the triple probe.

Electron temperature

Triple probe theory is derived from the formula of the current to a wire I_L at a potential V_b given in equation 4.6, true for V_b in the transition region between ion and electron saturation [113].

$$I_L(V_b) = I_{esat}\exp((V_b - V_p)/T_e) - I_{isat} \tag{4.6}$$

For simplicity, kT_e/e is given as just T_e, as in eV kT_e/e=T_e. If equation 4.6 is applied to three probes, like those shown in figure 4.6, each at a different potential described by probe P_n being biased with potential V_n and having current I_n (V_n), their currents can be reduced to equation 4.7 where V_{nm} is $V_n - V_m$.

$$\frac{I_1 - I_2}{I_1 - I_3} = \frac{1 - \exp(-V_{12}/T_e)}{1 - \exp(-V_{31}/T_e)} \tag{4.7}$$

Equation 4.7 is true for both the voltage and current mode, but a simplification can be made if voltage mode is used. In voltage mode, $-I_1 = I_3$ as the current through a wire must be conserved; additionally as probe 2 sits at the floating potential it draws no current, so $I_2 = 0$. These conditions reduce the left hand side of equation 4.7 to 1/2 giving equation 4.8. By taking the assumption that the battery bias $V_{31} >> T_e$, equation 4.8 can be further reduced, as $e^{-x}_{x\to\infty} \to 0$, to give equation 4.9 .

$$\frac{1}{2} = \frac{1 - \exp(-V_{12}/T_e)}{1 - \exp(-V_{31}/T_e)} \tag{4.8}$$

$$V_{12} = T_e \ln(2) \tag{4.9}$$

Using equation 4.9, the electron temperature can be calculated simply by measuring the floating potential and the potential on the probe P_2 connected to the positive terminal of the battery.

For the current mode, equation 4.7 cannot be reduced further but as the potential V_{12} and V_{13} are fixed by battery biases, the right hand side of equation 4.7 can be solved numerically over a range of values of T_e. To calculate the electron temperature using the current mode, the current through at least two probes must be recorded (the third can be calculated by conservation of current); additionally, one must also know the battery biases precisely.

Plasma density

To calculate the plasma density, equation 4.5 can be rearranged to give equation 4.10.

$$\exp((V_1 - V_p)/T_e) = \frac{I_1 + I_{isat}}{I_{esat}} \tag{4.10}$$

Equation 4.10 is then substituted into equation 4.7 with the value of I_{isat} taken for equation 4.4, resulting in equation 4.11 which can be used to calculate the plasma density n_e.

$$n_e = \frac{1}{en_e\sqrt{\frac{kT_e}{m_n}}A_{eff}\exp(-1/2)}\left[\frac{I_3 - I_1\exp(-eV_{12}/kT_e)}{\exp(-eV_{12}/kT_e)-1}\right] \tag{4.11}$$

Equation 4.11 is true for both the current and voltage modes. To calculate n_e in the current mode, there is no way to further reduce the equation. However in the voltage mode, as $I_1 = -I_3$, equation 4.11 reduces to equation 4.12.

$$n_e = \frac{1}{en_e\sqrt{\frac{kT_e}{m_n}}A_{eff}\exp(-1/2)}\left[\frac{I_1}{\exp(eV_{12}/kT_e)-1}\right] \tag{4.12}$$

Equation 4.12 can be further reduced by using equation 4.9 to show $\exp(eV_{12}/kT_e) = 2$, reducing equation 4.12 to a rearrangement of equation 4.4, effectively meaning I_1 and $-I_3$ are the ion saturation current.

As the current mode requires the current in at least two probes to be measured to calculate T_e, no further probes are required to measure n_e. However to calculate n_e in voltage mode, the current I_1 or I_3 must be measured in addition to the two voltage measurements needed to calculate T_e.

Floating and plasma potential

For current mode operation, both the plasma and floating potential are impossible to calculate without the addition of a fourth probe, to measure V_f.

The voltage mode records the floating potential V_f directly. Moreover V_f must be measured to calculate T_e and n_e, so recording V_f requires no addition to the voltage mode setup. V_p can be calculated using T_e and V_f by rearranging equation 4.6, into equation 4.13 and 4.14.

$$V_p = V_f - T_e\ln\left(\sqrt{\frac{I_{esat}}{I_{isat}}}\right) \tag{4.13}$$

$$= V_f - \alpha_2 T_e \tag{4.14}$$

Triple probe tip

As can be seen in figure 4.7. The triple probe tips are separated by 1 mm in two, double bore, ceramic tubes. These tubes are held together, flushed with polyimide tape, so that all bores in the tube are aligned with the same separation. The holes in the double bore tubes are 0.2 mm

in diameter, 0.12 mm wider than the wire probe tips (0.08 mm). This gap is filled by a set of four tubes, 0.2 mm outer diameter, 0.08 mm inner diameter, which are slightly recessed to reduce the rate at which a conductive film is sputtered onto the probe. This extends the lifetime of the probes in the plasma. The fourth bore is also filled with a ceramic tube and sealed with polyimide tape.

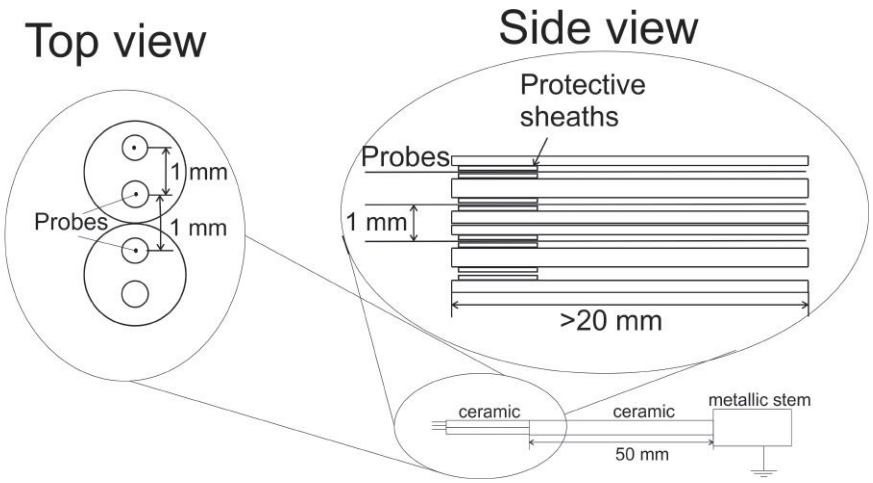

Fig. 4.7 Diagram of the triple probe tip; top and side view.

The ceramic used was alumina, extending ∼70 mm from the metallic probe stem, and cleaned of deposit regularly.

Triple probes: errors and drawbacks

While the triple probe does allow time-resolved, measurement which are not averaged over multiple pulses, it has several drawbacks. One such is that the triple probe will only measure one value of T_e, so in the cases where there are multiple populations of T_e, the triple probe will not give fully representative results.

The T_e measured by the triple probe will be the electron temperature in the range of the probe bias; for voltage mode this T_e will be measured between V_1 and V_f, whereas for current mode it will be in the range of all three probes.

The theory of the current mode triple probe has no simplifications, as equation 4.8 and 4.11 are solved numerically; Therefore the main sources of error will be inaccuracy in measuring the currents, the error in numerical calculation or from a voltage drop in the battery bias as described below.

The voltage drop across the batteries is a potential source of error, more important in the current than in the voltage mode. As batteries have an internal resistance, if the current

drawn from them increases, the battery output bias can be reduced. Given that equation 4.7 in current mode requires the battery bias to be known precisely, this can be a source of error. The effect of a battery bias drop is reduced when voltage mode is used, as the absolute value of the bias (V_{bias}) is unimportant as long as the condition $V_{bias} >> T_e$ is satisfied.

An important source of error in voltage mode is the assumption that the battery $V_{bias} >> T_e$, which is necessary for the calculation of T_e. While it would be trivial to use a large bias ($V_{bias} \approx 150V$), if V_{bias} is too large it will cause sheath expansion in the ion saturation region, and this would give a false high n_e. Therefore V_{bias} must be carefully chosen such that $V_{bias} >> T_e$, but V_{bias} does not cause significant sheath expansion. It can be seen from figure 4.1b that the current response to an increasing battery bias is greater in the transition region than in the ion saturation region, meaning that a V_{bias} value which is too large is preferable to one which is too small.

Another source of error from triple probes is inaccuracy of the voltage and current probes. However, this error is relatively easy to calculate from the given probe errors. The final source of error, the effect of magnetic fields, is discarded, as no suitable theory on triple probes in magnetic fields currently exists. It should also be noted that a Maxwellian electron distribution is assumed.

4.5 Imaging

Introduction to imaging

This section describes the camera and optical systems used to take images of the plasma while in operation. Simple 2D optical images were taken of the target racetrack during the HiPIMS on-time; if the times resolution is sufficiently fine, spokes can be observed. The imaging in this study was only performed in system two described in chapter 3.

Imaging system

The imaging system consists of an internal protective glass sheet, a quartz vacuum window, an external convex lens with focal length 50 mm, a 45° mirror and an intensified charge coupled device (ICCD) camera, all shown in figure 4.8. The protective glass sheet was placed on a rotatable substrate holder 4.5 cm above the target to protect the chamber window from the coating build-up and to maximize the experimental run time. The images were taken by the ICCD camera PI-MAX 3 (Princeton Instruments) equipped with Nikkor MF 80 – 200 f/4.5 camera lens. The ICCD camera worked in dual image feature mode (DIF), enabling the

capture of two snapshots during one HiPIMS pulse with a 3 μs delay between them. The start of the exposure was synchronized with the discharge pulse and the ICCD detector was gated through an electronic shutter with a gate width of 100 ns. The camera captured grey-scale images with 1024$\times$1024 pixels resolution, which can be later converted to (false) colour using MATLAB Jet(72) software. As can be seen in figure 4.8, a section of the guard ring has been cut to allow access to the strip probes; this resulted in a 15 % decrease in the light emitted from this area.

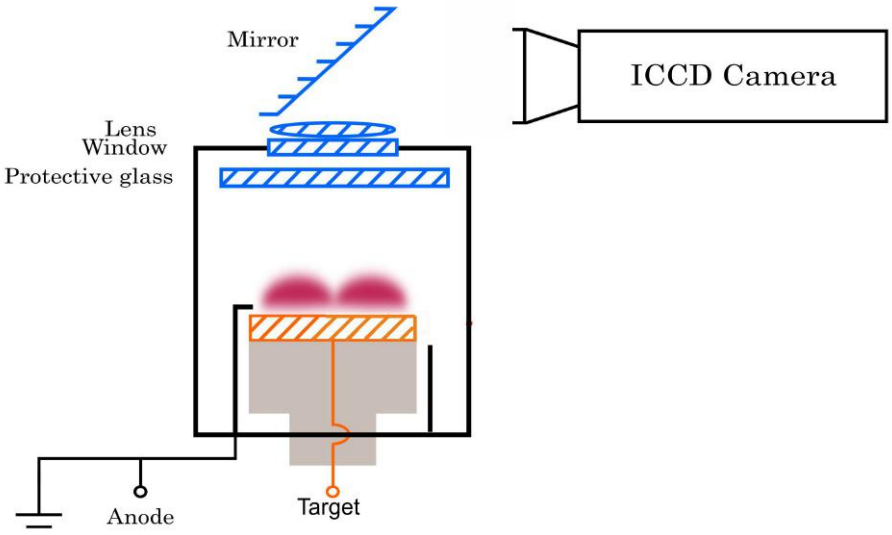

Fig. 4.8 The imaging setup, with focusing lens, cut away anode and mirror shown.

Imaging errors and limitations

The camera outputs a 2D black and white image of resolution 1024x1024 pixels. Since a single image contains over one million pixels, it is not useful to discuss the error on an individual pixel, and we instead focus on factors that affect the image as a whole. One such example is that the optical intensity is an arbitrary value. The (false) colour must be applied over this arbitrary scale between arbitrarily selected values; if this selection is incorrect then detail from the image becomes invisible over background brightness, losing important data.

The focusing is another sources of error; as the camera is being used to investigate spokes, it should be focused in the area where the spokes are expected, (3-5 mm above the target). This is also where one would expect the majority of optical emission to originate, lessening the effect of out of focus optical emissions from elsewhere. As the camera is used to take

images of moving events (spokes), the shutter speed can also create an error. Here we use a shutter speed of 100 ns, with an expected spoke velocity of $\sim$10 km s$-$1. With this shutter speed, the spoke is expected to move a distance $\sim$1 mm during the time it takes to take the image. This shutter speed could be reduced; however this would have further effects on the image, and an error of $\sim$1 mm is in line with the strip probe precision. The focusing and shutter speed and other camera aspects are very complex and are not discussed in detail in this study.

The major limitation is that the imaging system is restricted to only two images, taken a short time apart, with a long break between each set of two, of the order of milliseconds. This limits the set up to two images per pulse, with a fixed time delay between them. Additionally, the camera can only be used on the specific setup (system two) in chapter 3.

4.6 Summary

This chapter discusses the four main plasma diagnostics used in this study. The discussion here is kept general, with the use, plasma physics (where applicable), set-up and error and limitations presented. The full use of these diagnostics are described further in the chapters presenting results from experiments in which they are used.

The Langmuir probe is a simple and well established plasma analysis technique that consists of an insulated probe able to take a wide variety or readings. The Langmuir probe uses the plasma surface interaction governed by equation 4.1 to give T_e, n_e, V_p and V_f. The major limitation of the Langmuir probe is that it cannot measure a single short event and therefore it cannot be used to study spokes. A standard error of $\pm$20% is added to the results.

The strip probe is a segment of the target which has been electrically isolated; this allows the local current drawn from the plasma above the strip to be measured. The spoke velocity can also be measured by using multiple strips. The use of strips does limit the power that can be applied to the magnetron and the strips' width acts to smooth the outputted local current, though not in a major way. Additionally, changing the racetrack radius will result in a change in the strip probe, not reflected by a change in local current density.

The triple probe is a diagnostic able to give the same results as the Langmuir probe; however it can measure single short events. The triple probe can be used in both voltage and current mode and each require different methods of measurement and analysis. The voltage mode is able to measure V_f and V_p, however it requires simplifications in calculating T_e. The triple probe also requires all probes to be in very similar plasma conditions.

Imaging can be used, however, only on a dedicated rig as described in chapter 3. The camera produces two 2D images of the targets 3 μs apart, each with 100 ns exposure time. These images can be used to study spokes.

Together these diagnostics will be used to study spokes in detail in the following chapters.

Chapter 5

Strip probes in a HiPIMS discharge

5.1 Introduction

HiPIMS is a relatively new pulsed plasma, physical vapour deposition (PVD) technique that has a highly ionised sputter flux allowing IPVD (ionised PVD). This technique has advantages over PVD in the creation of thin films [24]. Recent studies of HiPIMS have found high energy ions are present in the HiPIMS discharge and has linked them to the phenomenon known as spokes [29] [23]. High energy ions are important in IPVD as they affect the properties of the films which are deposited [52]. A fuller description is contained in chapter 2.

In many low-pressure plasma devices, including HiPIMS, the discharges demonstrate plasma self-organization in which ionization zones, the spokes, can be seen to rotate in the E×B direction [31]. In HiPIMS, spokes are believed to be regions of higher local plasma density with anomalously high positive space potentials. They sit directly above the cathode target sheath and rotate around the closed azimuthal path of the magnetron in the E×B direction. Spokes themselves are likened to double layer regions (or perhaps more accurately triple layer regions) [29]. This triple layer acts to counter streaming ions and electrons and their associated plasma instabilities [87].

In HiPIMS discharges, spoke velocities range from 4 to 15 km s^{-1} depending on the target material and running/background gas. This corresponds to rotation frequencies from several 10's to 100's kHz depending on the target dimensions [81].

Discharge operating parameters such as target current density (power) and working pressure can also have a large effect on the nature of the spokes [36]. The mode number m, which indicates the number of spokes present on the target at any one time (typically $1 <$ m < 5), is also influenced heavily by the operating parameters [36]. Since it is believed that

spokes are high density regions with higher associated ionization rates on the target surface, it is logical to assume that the target beneath the spoke has an increased deposition rate and therefore that a considerable fraction of the total discharge current I_d is carried by the spokes. This is assumed by Gallian et al [87].

A number of diagnostic techniques have been employed to study and characterize the nature of spokes in HiPIMS discharges. These include the use of electrical probes positioned outside the magnetic trap. These probes are either floating or operate in either the electron or the ion saturation current regions of the plasma. They can be used to observe the modulation in the plasma density as the spokes pass the probe [38] [28]. The most common technique of studying spokes, however, is to employ fast intensified cameras (ICCD's) to take an image of the target, with time resolution < 1 μs [102], to determine the spokes' shape, mode number, rotation speed, and the general conditions of existence for such rotating instabilities [104] [114] [85].

Notably Hecimovic et al [86] have used fast optical imaging and an array of electrical probes to record the floating potential in order to observe spokes rotating around the race track. They have also studied events of spokes merging and splitting, which lead to changes in the mode number.

ICCD cameras with shutter speeds required to observe spokes are costly, especially if one wishes to investigate spoke velocity because this requires multiple images to be taken during one pulse. The main alternative method of studying spokes has been electric probes placed outside the magnetic trap. However in this chapter we detail an attempt to improve on this.

Plasma parameters, such as the electron temperature and the density associated with the spokes, have been obtained in Hall thrusters by using flush mounted planar probes [115]. However, it is problematic to try to obtain such measurements with electrical probes in HiPIMS. This is because they can potentially destroy the phenomena concerned by introducing a ground to the plasma. Moreover, the probes themselves can accumulate a considerable amount of deposit on their tips, which corrupts their operation. Therefore in this chapter we do not attempt to measure the plasma parameters within the spokes themselves, but instead employ an array of electrical probes (strip probes) forming a segmented target to measure the distribution of current sourced from individual spokes directly as they rotate around the racetrack. The strip probes are made of the target material, are mounted flush to the target surface, and have the same cathode potential, which should make them indistinguishable from the rest of the target as far as the plasma directly above them is concerned. However whether the strips are indistinguishable from a whole target or whether the 0.08 mm gaps have no measurable effect on the discharge, remains to be confirmed. Using this arrangement,

we also measure the spoke velocities, mode number and azimuthal profile (shape) during the HiPIMS pulse. //

The remainder of this chapter is organised as follows. In the next section, we outline the two rigs and experimental set ups used to generate results for this chapter; system one in the University of Liverpool using strip probes and the second, system two at the University of Masaryk using an ICDD camera with the strip probes. The results are reported and discussed in the third section, which includes the tests and the comparisons of results using strip probe current as against the camera images as well as an analysis of mode number changes. Conclusions are drawn in the final section.

5.2 Experimental setup

This experiment was conducted using two set ups. The system one was based in the University of Liverpool Department of Electrical Engineering and Electronics, and used an alumininum target. System two was based in the Department of Physical Electronics at Masaryk University, Kotlářská, Brno, Czech Republic, and used a niobium target. Both systems are described in more detail in chapter 3 with the strip probe and imaging diagnostics described in chapter 4 in more detail.

System one setup

The first part was conducted in a purpose-built cylindrical vacuum vessel, 300 mm in length and 260 mm in diameter, pumped down to a base pressure of $< 10^{-3}$ Pa using a turbo molecular pump backed by a rotary pump. Argon was introduced into the vessel with flow rates ranging from 0 to 50 sccm (standard cubic centimetre per minute) determined and controlled using a capacitance pressure gauge (MKS 628A) and a mass flow controller (MKS 1179A) respectively. The general chamber configuration is shown in figure 5.1a. The magnetron used in this study was a circular unbalanced type, equipped with a 75 mm diameter aluminium target of 6.35 mm thickness and 99.995% purity (racetrack = 21.5 $\pm$ 0.5 mm radius). Power supply A with a simmer source, as described in chapter 3, was used providing a peak current of 60 A operated at a repetition rate of 3 Hz and a pulse width of 70 μs providing energies up to 2.15 J per pulse. This setup used three strip probes, as described in chapter 4. The three 2 $\pm$ 0.02 mm wide flush-mounted aluminium strip probes (same purity as the target) were placed in machined slots at 3 angular positions 45° around the target, see figure 5.1b.

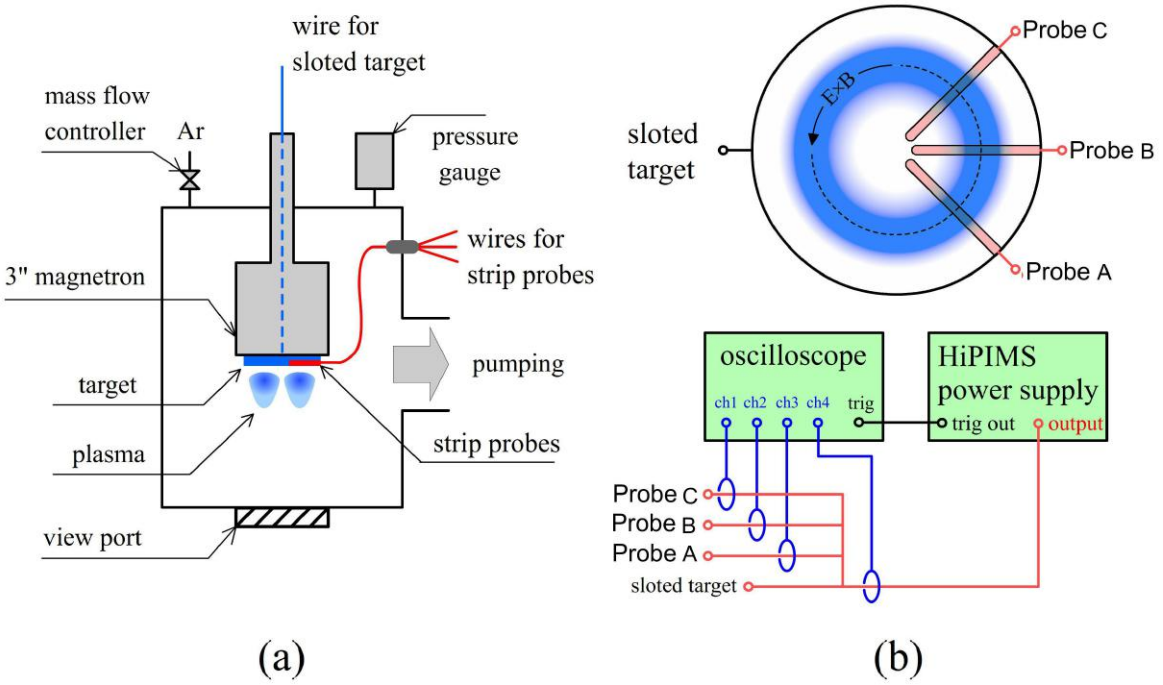

Fig. 5.1 Schematic diagrams of a) the magnetron and chamber setup and b) the strip probes and current measuring arrangements.

The three strip probes filled the entire target track radius and extended past the target edge by 5 mm to allow electrical connections. The strip probes were electrically isolated from the rest of target by a thin layer of polyimide tape of thickness of 0.07 ± 0.01 mm, placed around 3 sides of the probe, which provided a tight fit. This insulation thickness defined the gap between the strip probe and the target. The three strip probes were connected directly to power supply A as shown in figure 5.1b. In this configuration they always remained at the same potential as the target, but with their contribution to the total current measured separately using Pearson current probes (Model 2877 with 1 V/A). The total target current, I_d, was measured using a larger Pearson probe (Model 3972 with 0.1 V/A). The four current waveforms were recorded using a digital oscilloscope (Tektronix DPO 3034 with 300 MHz bandwidth) in a single short mode, if not otherwise stated. The discharge voltage waveforms V_d were measured separately using a high voltage probe (Tektronix P5100).

System two setup

The second part of the experiment was conducted using an Alcatel SCM650 magnetron sputtering system, housing a 75 mm diameter circular magnetron (Kurt J. Lesker) fitted with a

niobium target of 99.95% purity. The deposition chamber was pumped by a turbo-molecular pump backed by a roots pump to a base pressure below 10^{-4} Pa, measured using both Capacitance Baratron MKS gauge and a PKR251 compact full vacuum range gauge (Pfeifier Ltd). Argon gas with 99.999% purity was supplied to the vessel at a flow rate in the range of 1 - 140 sccm (standard cubic centimetres per minute) to provide working pressures from 0.14 - 5 Pa.

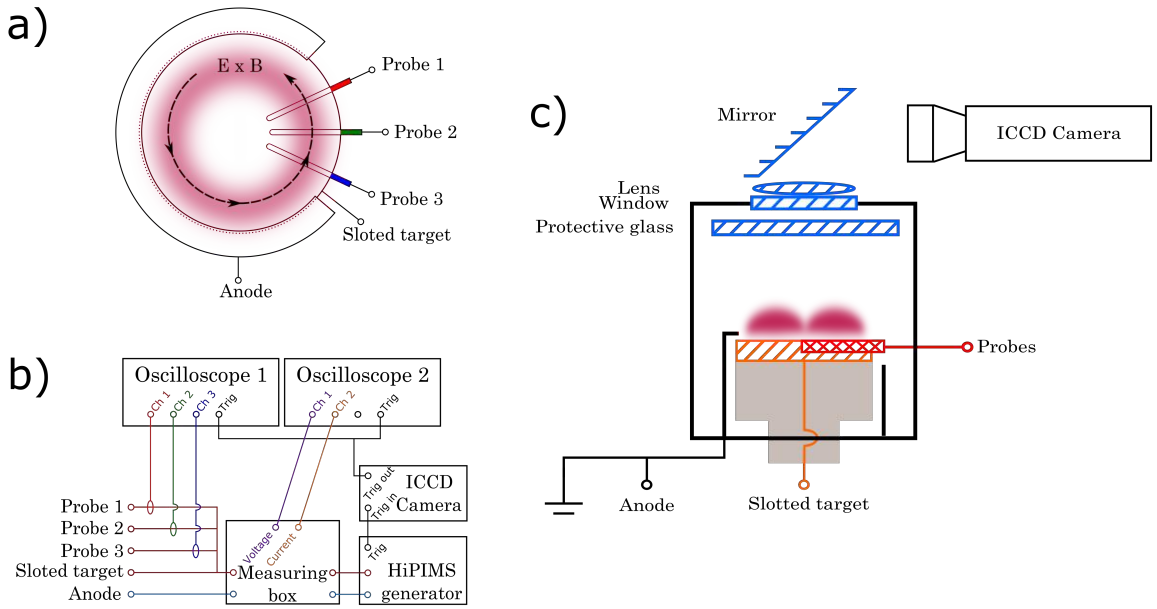

Fig. 5.2 Schematic drawing of the a) top view of the target strip probe experimental setup, b) strip probe electrical arrangement and c) the optical imaging arrangement.

The target was a 75 mm diameter (racetrack = 25 $\pm$ 0.5 mm radius, wider than the main rig) niobium target with three flush-mounted niobium strip probes; the same purity as the target. These were placed in machined slots at 3 angular positions (25° from each other) around the target, but otherwise were the same as the one used in the main chamber. To accommodate the strip probes, the outer anode shield of the magnetron was cut away as shown in figure 5.2a and c. This unavoidably influenced the discharge marginally in the vicinity of the strip probes, as seen by a 15% drop in the intensity of the optical emission signal compared to the rest of the target.

The three individual strip probes were connected directly to the HiPIMS power supply as shown in figure 5.2b, allowing each to maintain a potential equal to that of the rest of the target. Their contributions to the total discharge current were measured separately using three Pearson current probes (Model 2877 with 1 V/A). All three probe signals were recorded

using the single shot mode facility of a LeCroyWaveRunner 6100A digital oscilloscope with a 4 ns sampling interval. The waveforms for the total discharge voltage and discharge were measured using a measuring system integrated in the Melec generator, in which cathode voltages and currents in the range 0 - 1000 V and 0 - 500 A respectively were displayed as voltage signals in the range 0 - 10 V. These readings were recorded using a Keysight Infiniium DSO-S 204A oscilloscope working in single shot mode with 4 ns sampling interval.

The 2-D optical imaging arrangement to observe the rotating spokes is shown in figure 5.2c. The system consisted of an internal protective glass sheet, a quartz vacuum window, an external convex lens with focal length 50 mm, a 45° mirror and an intensified charge coupled device (ICCD) camera. The protective glass was placed on rotatable substrate holder 4.5 cm above the target to protect the chamber window from the coating build-up and to maximize the experimental run time.

The images were taken by the ICCD camera PI-MAX 3 (Princeton Instruments) equipped with Nikkor MF 80 - 200 f / 4.5 camera lens. The ICCD camera worked in dual image feature mode (DIF), enabling the capture of two snapshots during one HiPIMS pulse with a 3 μs delay between them. The start of the exposure was synchronized with the discharge pulse and the ICCD detector was gated through an electronic shutter with a gate width of 100 ns. The camera captured grey-scale images with 1024x1024 pixels resolution, which were later converted to (false) colour using MATLAB Jet(72) software.

5.3 Results and discussion

Testing the strip probe

Strip probe tested at a range of powers and pressures (system one)

The measurement of the local current drawn from strip probe A (figure 5.1b), I_p and the total discharge current to the target (including the strip) I_d for a set of pressures (0.18 to 1.59 Pa) and a variety of pulse energies E_p (0.15 to 2.2 J) are shown in figure 5.3.

Under certain conditions, we observe strong oscillations in I_p which we attribute to the existence of coherent spoke structures. At low pressures, 0.18 Pa and low pulse energies $E_p < 0.5$ J, oscillations appear somewhat chaotic with irregular and non-periodic peaks and valleys during the pulse. However, as the discharge energy is increased, more coherent periodic structures develop with oscillation amplitudes growing monotonically with E_p. There appears to be a threshold in E_p for coherent spokes to form, and this decreases with

increases in pressure. For example, in figure 5.3 we see at 0.81 Pa a threshold value of E_p $\sim$1 J; however this decreases to E_p $\sim$0.6 j at 1.58 Pa.

The largest amplitude in the I_p oscillations seen in figure 5.3 at E_p = 1.8 J, 0.81 Pa, is about 45% above the base level (the I_p values in the valleys) at 30 - 40 μs into the pulse, figure 5.3b.

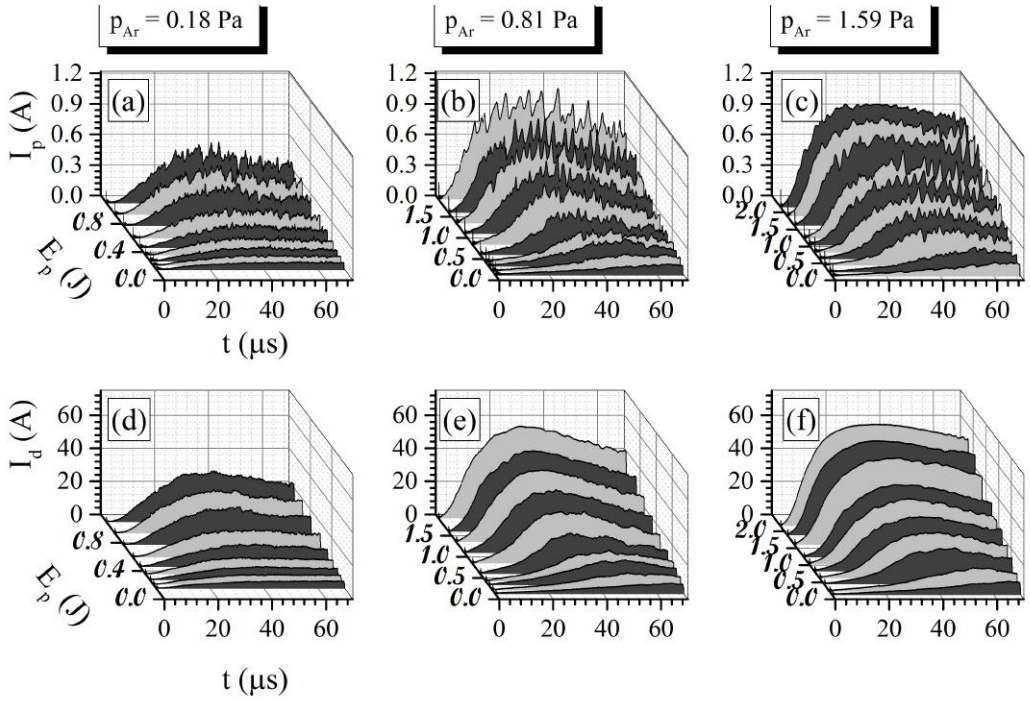

Fig. 5.3 In a), b) and c) time traces of the strip probe current, I_p, in d), e) and f) time traces of the total target current, I_d, for a number of pulse energies E_p and argon pressures, 0.18, 0.81 and 1.59 Pa.

In contrast to the strip probe measurements, the total discharge current I_d measurements at any operating condition show little or no perturbations. This can be expected since the current contribution from any non-changing structure moving around the whole target will yield no temporal dependency in the I_d measurement. There are very small oscillations seen in I_d, discernible in figure 5.3 ,d to f, and reported in the discharge current elsewhere. However, there is no evidence to linking them to spokes directly.

Although we have no optical imaging evidence of spokes from this experimental setup, the data show a lack of notable oscillations in I_d combined with strong oscillations in the I_p measurements. This gives us confidence we are observing moving plasma structures passing over our strip probe rather than any kind of superimposed signal from the plasma-power

supply network. The logical next step is therefore to test the strip probes in conjunction with optical imaging.

Strip probe tested with imaging (system two)

Figure 5.4 shows three representative images of the broadband plasma emission (300 - 850 nm) and the corresponding strip probe 1 (figure 5.2a) current signal for three different instantaneous discharge current readings: I_d of 30 A at 20 μs, 185 A at 140 μs, and 240 A at 195μs, during a set of identical 200 μs pulse E_p = 15.6 J at 5 Pa. The emission intensities are normalised to a maximum intensity within that image.

As seen in figure 5.4a, early in the pulse at very low discharge currents, spokes are not yet fully developed. The plasma emission is homogeneous with no periodic structures in I_p, only a gradual increase in I_p as the total discharge builds up, progressing through the pulse. Spokes are formed by the time I_d reaches 185 A, as in figure 5.4b, which shows six differentiated diffusive spokes clearly visible and with a matching harmonic signature signal on the strip probe. At 240 A, the spokes becomes triangular in shape, see figure 5.4c, as observed in many optical studies. This shape is easily discernible in the strip probe current signal as the spoke passes with a shallow rise in current followed by a more rapid fall. Both the diffusive and triangular spokes are observed at a pressure of 5 Pa. Decreasing the pressure leads to a decrease in the spoke mode number for the same discharge current. Additionally, only the triangular spoke shape, with a very precisely defined trailing edge of the spoke, is observed.

These observations directly correlate with the oscillation in the strip probe current I_p to spokes as observed by ICCD camera. Given that the current IV characteristics match those for an unaltered target and that the ICCD images do not show any difference in the plasma above the strips, it can be concluded that as far as the discharge is concerned, the strips are indistinguishable from the target. It should be noted that, across the variety of amplitudes of I_p perturbations in figures 5.3 and 5.4, the spokes never carry the majority of the current, nor does I_p ever fall close to zero. This might counter to expectations from the images of spokes in figure 5.4b and c, where the gaps between the spokes have an emission intensity close to the background. It is purposed that this apparent lack of discharge between the spokes present in the images is not a physical result but a result of the normalisation of the background optical intensity.

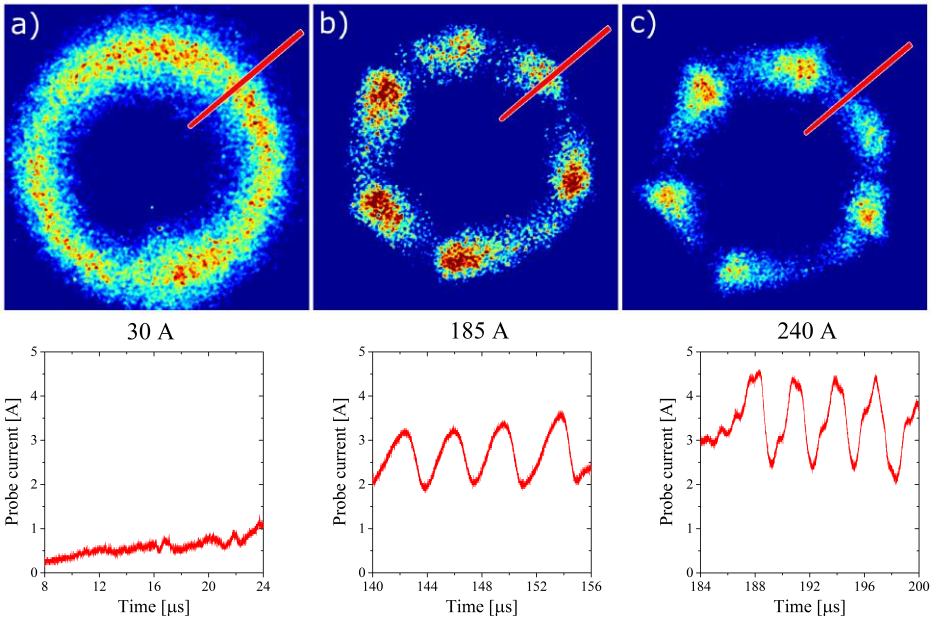

Fig. 5.4 Broadband emission images of the full target with corresponding strip probe current measurements (strip 1) for an operating pressure of 5 Pa, E_p = 15.6 J at times of a) 20 μs b) 140 μs c) 195μs. Note: intensities are normalized to maximum intensity with the given picture.

Spoke velocity

One of the potential applications of strip probes is for the measurement of spoke velocity. Below, this technique is explained and compared to conventional methods using imaging, before being applied to investigate the link between spoke velocity and critical ionisation velocity (CIV).

Measurement of spoke velocity and mode number using strip probes (system one)

To gain information about the speed of the spokes and their mode number, I_p measurements were made simultaneously with all three strip probes, each separated by 45° increments. The case where E_p = 1.79 J and 0.68 Pa is shown in figure 5.5.

The I_p waveforms have been stacked (with a vertical increment of I_p = 0.6 A) to allow the phase information to be seen clearly. The I_p oscillations are similar between probes in terms of shape, amplitude and period but the phase has been shifted by a time (τ). This demonstrates the existence of essentially coherent (and rigidly-formed) current perturbations, rotating in the E×B direction; in short, spokes. In the particular case chosen, over the driven part of the discharge, we can identify seven distinct oscillation packages, labelled as I to VII in figure 5.5. To calculate the spoke angular frequency, ω and tangential velocity, v at the racetrack

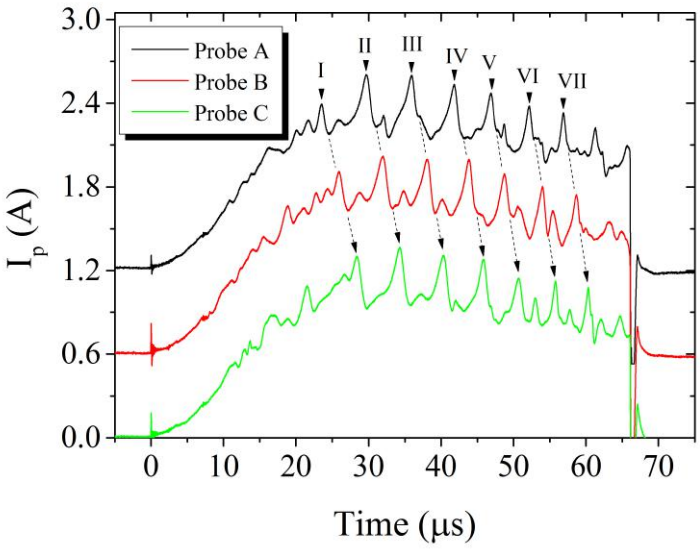

Fig. 5.5 The strip probe current time traces for E_p = 1.79 J and pressure 0.68 Pa. The traces are stacked (incremented by 0.6 A to allow the phase relationship to be seen). The rapid, short-lived, negative current observed at the end of the pulse is thought to be the result of finite inductance of strip probe assembly.

centre (radius $r_0 = 21.5 \pm 0.5$ mm) average time delays τ_{avg} in the peaks have been used. We define $\tau_{avg} = (\tau_{AB} + \tau_{BC})/2$, where τ_{AB} and τ_{BC} are the time delays between probes A and B and probes B and C, respectively. The spoke speed calculations are summarized in table 5.1.

Peak	τ_{AB} (μs)	τ_{BC} (μs)	τ_{avg} (μs)	ω (rad s^{-1})	v (km s^{-1})
I	2.45	2.41	2.43	3.23 x 10^5	6.95
II	2.29	2.36	2.33	3.37 x 10^5	7.26
III	2.13	2.27	2.20	3.57 x 10^5	7.68
IV	2.04	2.02	2.03	3.87 x 10^5	8.32
V	1.96	1.91	1.94	4.05 x 10^5	8.73
VI	1.80	1.86	1.86	4.29 x 10^5	9.23
VII	1.67	1.78	1.73	4.54 x 10^5	9.79

Table 5.1 Table of τ_{AB}, τ_{BC} and τ_{avg} for all spokes in figure 5.5 from which spoke velocity is calculated.

From the average period of oscillation T_{avg} and the time lag τ_{avg} data, the mode number m can be determined as m = $(8 \times \tau_{avg})/T_{avg}$ (for strips with 45° separation). In our chosen operating condition (0.68 Pa, E_p = 1.79 J), we find values of m between 2.8 and 3.1. This indicates that we have m = 3 operation.

It is known from the literature that the mode number varies with operating conditions, for instance with higher m observed for increased pressure as evidenced by the higher mode number in seen in figure 5.4.

The velocities observed as well as the mode number of spokes measured by the strip probe in this experiment closely match what has been reported in the literature [84]. However confirmation by the simultaneous use of camera and strip probes can provide further evidence.

Spoke velocity from strip probes and camera (system two)

Spoke velocity has often been measured previously by imaging [31]. This technique takes two or more images with a set time delay and tracks the spoke's angular progression during this time. In this subsection, we use the dual image (two consecutive plasma emission images) feature of the PI-MAX 3 camera to calculate the spoke velocity. For the same pulse, we also use the strip probe to calculate the spoke velocity (using the method described above). This is best accomplished with lower mode numbers, as the spokes are larger and more clearly defined. The best conditions were found at pressure 0.14 Pa and E_p = 9 J, with images taken at 210 A, 191 and 194 μs into the pulse where m = 2.

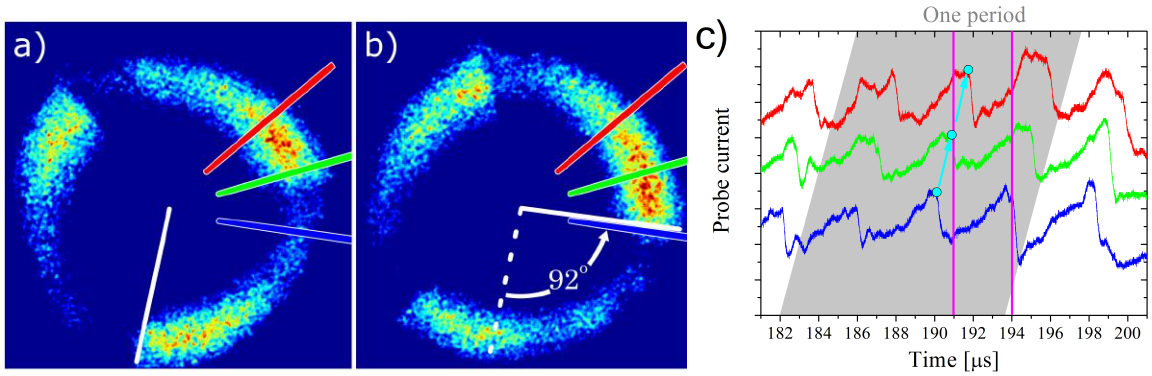

Fig. 5.6 In a) and b) two consecutive 2-D emission images of the whole target from a single pulse and c) the corresponding strip probe waveforms (red, green and blue) for an operating pressure of 0.14 Pa E_p = 9 J, instantaneous discharge current of 210 A and cathode voltage of 628 V. The vertical violet lines at time of 191 μs and 194 μs indicate when the optical images a) and b) were taken. The grey background depicts a spoke rotation period.

Figure 5.6a and b show images at a 191 μs and 194 μs (3 μs between images). In both images, the position of each strip probe is indicated by a different colour. Three well developed triangular spokes are clearly seen rotating in a counter-clockwise direction with a velocity of 13.4 km s^{-1}. This is calculated from a spoke travelling 92° around the racetrack (total length of 157 mm) in the 3 μs camera delay time between the images of figure 5.6a and b. The corresponding current signals for the three strip probes are shown in Figure 5.6 c.

The two violet vertical lines (at time of 191 μs and 194 μs) indicate when the 2-D images were taken. From the current traces, a spoke rotation velocity of 13.5 km s^{-1} (the gradient of the cyan line in Figure 5.6c) and a rotation period of 11.6 μs are determined; this is a value extremely close to that determined above optically. This shows that the strip probe method of determining spoke velocity can generate equivalent results to the more established camera method [88].

Critical ionization velocity (system one)

The majority of spoke velocity measurements in the literature have been found using the imaging techniques mentioned above [84]. However this technique can only measure the spoke velocity during the short period between images, whereas strip probes are able to measure the spoke velocity (v) for the entire time that spokes are detectable. In this subsection, strip probes are used to derive spoke velocities over the whole pulse and these are analysed to see how v changes over the pulse.

Previously, v was measured for conditions E_p = 1.79 J and 0.68 Pa pressure in the main rig. The results are shown in table 5.1 and lie between 6.95 and 9.79 km s^{-1}. These values of v are similar to those seen in other HiPIMS discharges with Al targets [88].

To determine any gross trends in v during the evolving HiPIMS pulse, spoke velocity has been calculated over ten identical HiPIMS pulses and plotted as a function of time in figure 5.7.

We observe that, as the pulse progresses, v increases from about 6.5 to 10 km s^{-1}. This increase can partly be understood as being caused by a change in the composition of the plasma. It has been postulated that spoke speeds adhere to the critical ionization velocity (CIV) hypothesis, with the CIV given by $v_{CIV} = \sqrt{\frac{2eE_{iz}}{m_n}}$. As the discharge builds up, and certainly at times close to the peak discharge current, we expect the discharge to be dominated by Al giving a CIV velocity $v_{CIV.Al}$ = 6.5 km s^{-1}. However, towards the end of the pulse, we conjecture that argon replaces the Al particles and the CIV velocity will therefore increase to $v_{CIV.Ar}$ = 8.7 km s^{-1}. The results in figure 5.7 suggest just such a trend, because the weighted mass m_n and effective U_i values change with the composition. The CIV for the two gas species are shown in figure 5.7.

For t $>$ 50 μs, our calculated spoke velocities exceed the CIV velocity for Ar. One possible explanation for this is that, as the spoke evolves in time, its average radial position may change. If the spoke's average radius of rotation were to reduce by about 3 mm, the distance the spoke travels (the race track circumference), would be reduced. This would decrease the calculated velocities by 13%. With a reduction of 13 %, the measured spoke

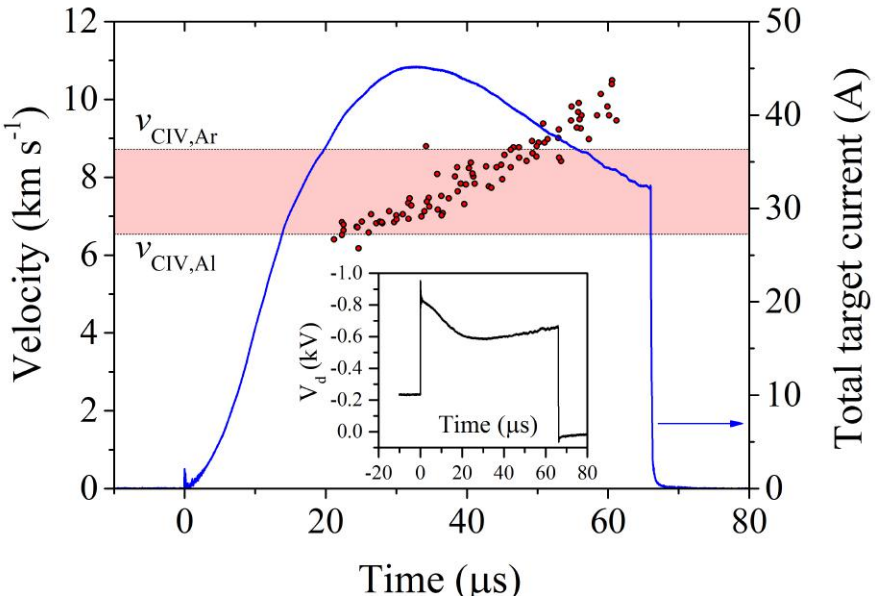

Fig. 5.7 A plot of spoke velocities through a HiPIMS pulse, calculated from the time lags in the waveforms between the azimuthally separated strips. The data were recorded over ten HiPIMS pulses for E_p = 1.79 J and 0.68 Pa. The target current and voltage for this discharge are also shown.

velocity would always be limited to $v_{CIV.Ar}$. Note that such a change would cause an equivalent error, even if imaging were used to determine v, as the racetrack radius is not discernible to within 3 mm by image.

Our estimated spoke velocities are comparable to those obtained in other HiPIMS plasmas with Al targets, for instance a velocity of 8.1 ± 0.3 km s^{-1} determined by fast camera imaging [39].

This argument of changing composition is consistent with measurements made using time-resolved tunable diode-laser absorption, where Ar depletion was found to occur at the peak of the target current. In the early stages of the discharge, it is difficult to identify and then calculate v. Hence we are unable to demonstrate that spoke's velocity is consistent with the $v_{CIV.Ar}$ velocity, as we would expect in this stage in the discharge before Al becomes the dominant species [67].

In the case of the niobium target, the spokes' velocity of 13.5 km s^{-1} was far higher then the CIV of either Ar or Nb. These results were taken at lower pressure, 0.14 Pa. We know that spoke velocity is inversely correlated with pressure, so this result indicates that, at low pressures, CIV is not the dominant effect in spokes' velocity. Indeed, velocities far above

those dictated by CIV have been reported [37] and therefore further investigation into the relationship between spoke velocity and CIV is needed.

Spoke regimes and amplitudes (system one)

A notable advantage of the strip probe method is that it produces quantified readings. This is in contrast to image intensity readings, which must be normalised. It is true that other techniques have also measured oscillations in qualified values as spokes pass [97] [86]. However they did so outside the magnetic trap region, some distance from the spoke region so they could not be said to measure total oscillation due to spokes. The strip probes are embedded in the target so they measure the flux through the target side of the spoke to the target directly.

In figure 5.3 it can clearly be seen that the amplitude of spokes varies with conditions such as pressure and power. Not only does the amplitude change, but the spokes themselves show different behaviours. To illustrate this, measurements for three discharge conditions have been made and are shown in figure 5.8. Here we choose pulse energies E_p of 0.11, 0.87 and 2.20 J at a single operating pressure of 1.92 Pa.

During the early part of the pulse, at low pulse energy, (t $<$ 30 μs, E_p= 0.11 J), we see no evidence of spokes in the I_p traces (as in figure 5.4a). However, as the current increases, even at this low pulse energy, we can observe a fluctuation in the strip current waveform from about 40 to 65 μs. Increasing the pulse energy to E_p = 0.87 J reveals strong oscillations in I_p. It also seems clear that in the early part of the pulse (i.e. at low discharge current), the plasma is homogeneous, which has been observed elsewhere (figure 5.4). Here, strong oscillations in I_p start at t $\sim$15 μs and remain throughout the pulse.

In figure 5.8, the dashed lines represent an effective oscillation envelope within which the peak-to-valley amplitude of the oscillation ΔI_p can be determined. We define the bottom of the valley as the base current I_b; for example, at t $\sim$ 40 μs, ΔI_p = 0.24 A, which corresponds to about 32% of the base current (I_b = 0.73 A). The ratio $\Delta I_p/I_b$ varies during the pulse, rising to a plateau of 0.32 then persisting up to the end of the pulse. At the highest pulse energy condition, E_p = 2.20 J, oscillations are significantly attenuated with ΔI_p = 0, particularly during times of peak discharge current I_d (t $\sim$30-40 μs).

The peak-to-valley strip probe current densities normalized to the base current (valley) $\Delta I_p/I_b$ are shown in figure 5.9. The measurements were obtained at one particular time during the pulse (t = 40 μs) and are mapped out as a function of pulse energy and operating pressure. The maximum value of $\Delta I_p/I_b$ is = 0.52 at E_p = 1.6 J and pressure 0.7 Pa.

In figure 5.9, we represent an approximate boundary which separates two regions, one where spokes appear to be more chaotic and one where they are coherent. It is at low E_p

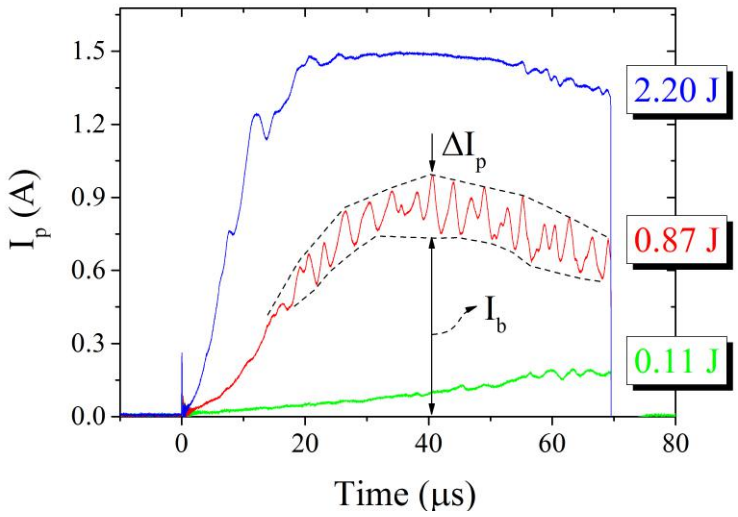

Fig. 5.8 A plot of I_p for E_p = 0.11 J, 0.87 J, 2.20 J at a pressure of 1.92 Pa, showing the effect of power on the amplitude and nature of spokes. Also shown is the method of measurement of ΔI_p an I_b, used to calculate the spoke amplitude.

(typically $<$ 0.8 J) where chaotic behaviour is generally observed, as reported by Winter et al [39]. One should note that due to limitations of power supply A, some operating parameters could not be attained and these are represented by the shaded region in figure 5.9 . In later experiments, the more powerful power supply B is used to address this problem. Despite this experimental limitation, the contour plot does clearly reveal regions where spokes are chaotic in nature; coherent (as in figure 5.9 E_p = 0.87 J); and non-existent. Our observations are in general agreement with those obtained using fast optical imaging to investigate spoke structural evolution [39].

The mechanism determining spoke formation is unknown, but it appears that chaotic structures are observed at low power only and their amplitude is largely independent of pressure. However, once coherent spokes are created, pressure plays a key role in determining the current oscillation amplitude above its base value. It is argued that collective behaviour such as spoke formation is a result of insufficient ion production, with structures moving to seek regions of enhanced ionization [31]. At high powers, sufficient ionization takes place and spoke structure is lost. Individual spokes may merge to form a single continuous structure, possibly maintaining a reversal in axial electric field (potential fill) but with no azimuthal component. Increased pressures may provide the necessary sustainment and hence reduce spoke current amplitudes.

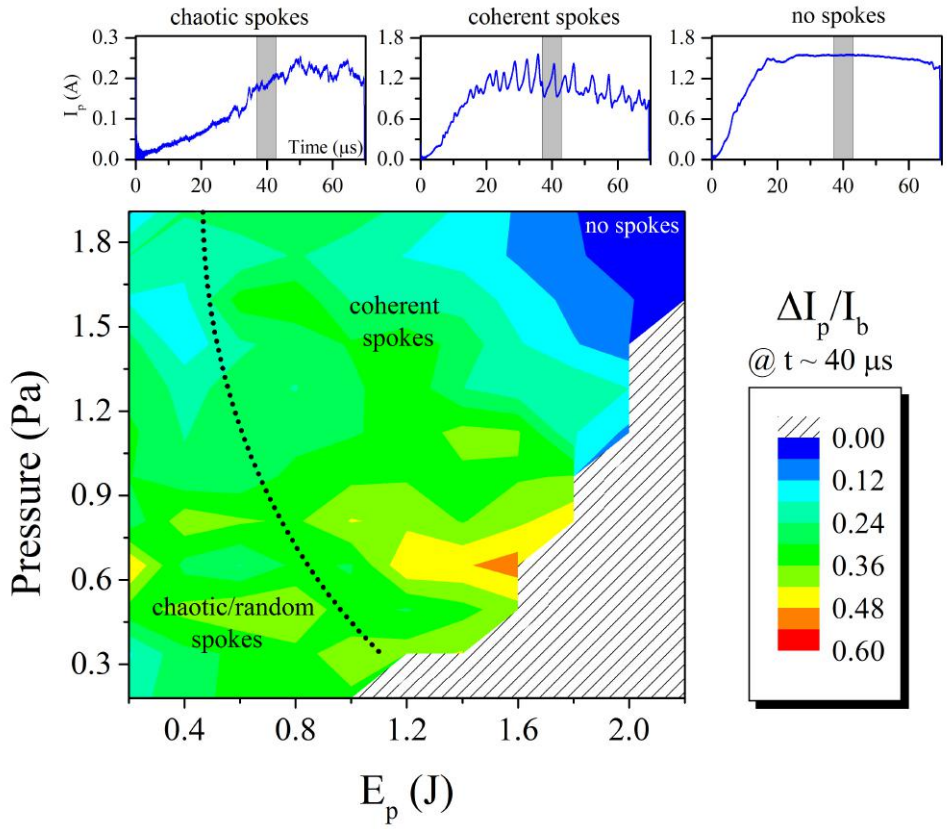

Fig. 5.9 A contour plot of $\Delta I_p/I_b$, the ratio of ΔI_p normalized to the base current I_b, at time t $\sim$40 μs for a range of pulse energies E_p and argon pressures. The hatched region represents an area inaccessible to experiment due to power supply limitations. The dotted line represents the approximate boundary between chaotic and coherent spoke behaviour.

Strip probe current compared with camera images (system one and two)

In previous sub-sections, it has been demonstrated that spokes can be observed using both strip probes and camera imaging. In this section we provide a direct comparison of the two techniques.

To allow the comparison, we have attempted to display the current density data in 2-D, as has been done for optical signals obtained from fast imaging. This can be achieved by transforming the temporal distribution I_p(t) (obtained using the system one to an angular distribution of current density $j_p(\theta)$ and convolving it with a Gaussian radial distribution to artificially add radial information. We choose a Gaussian function G(r) = A exp $(-(r-r_0)^2/L^2)$, where r_0 = 21.5 mm is the radius of racetrack centre, L = 10 mm is an assumed mean radial width of the spokes, and A is a scaling constant to be calculated. Although we have no radial

measurements of I_p in this study, the invoked Gaussian representation of I_p(r) centred on the middle of the racetrack is sufficient to produce a realistic 2-D distribution of target current density j(θ, r). A Gaussian function is based on work by Clarke et al [35] which investigated radial cathode current. Here we choose the current density data from figure 5.10 (probe C) over one period T from 30 - 47 μs. To ensure our function j(θ, r) provides the correct measured discharge current I_d ,it must satisfy the condition

$$\int_0^{2\pi}\int_0^R \mathrm{j}(\theta, \mathrm{r})\ \mathrm{r}\ d\theta\ dr = I_d.$$

where j(θ, r) = G(r)$j_p(\theta)$ and R is the target radius. Here the target current I_d is averaged over the same time period ($30 \leq \mathrm{t} \leq 47$ μs) as the j_p(t) was collected. Performing the integral yielded, in the particular case chosen, a scaling constant A = 1.06.

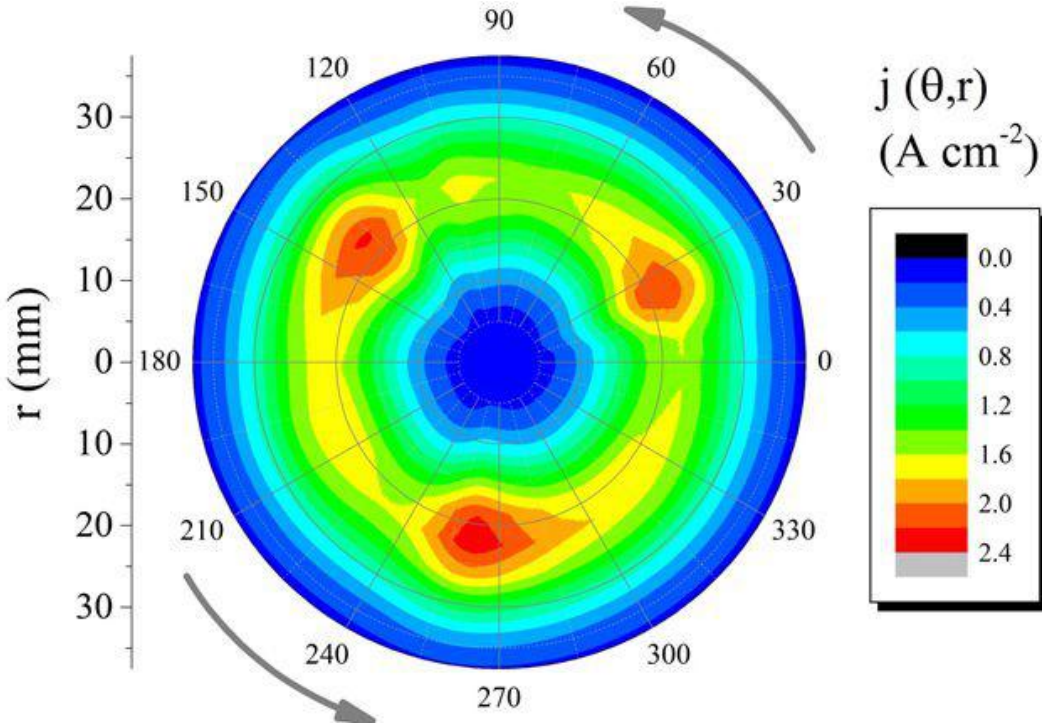

Fig. 5.10 A 2-D reconstruction of the target current density using measured azimuthal data combined with an assumed Gaussian radial current density distribution, of the form G(r) = A exp (-(r-r_0)^2/L^2). The azimuthal data was obtained for 0.68 Pa, E_p = 1.79 J, and for spokes passing a single strip in the time period 30 - 47 μs. The arrows show the direction of motion of the spokes (i.e. in the E×B direction).

It is interesting that in figure 5.10, our constructed map of j(θ, r) is very much consistent in form to that obtained through optical emission fast imaging. The shapes of the spokes seen in figure 5.10 show a *soft* triangular shape similar to those seen in figure 5.4b. It seems clear

that spokes do carry a considerable fraction of the discharge current, since their elongated structure occupies a significant area of the target in the racetrack region. In the case displayed, the peak current density at the spokes' centre is highly localized and has a current density 43% greater than that at the racetrack minimum.

The converse comparison can be achieved by taking the varying image intensity around the racetrack of a 2-D image and plotting it as a 1-D figure using velocity to convert radial position to time. The 2-D images in figure 5.6a and b have been transformed in this manner and are shown in figure 5.11a and b together with the corresponding probe current waveform from strip 1 (figure 5.2a). The time-trace of the transformed optical data matches the strip probe current traces closely; that is to say, the length of the spokes are equal, the phases are consistent and the maxima and minima appear at the same time.

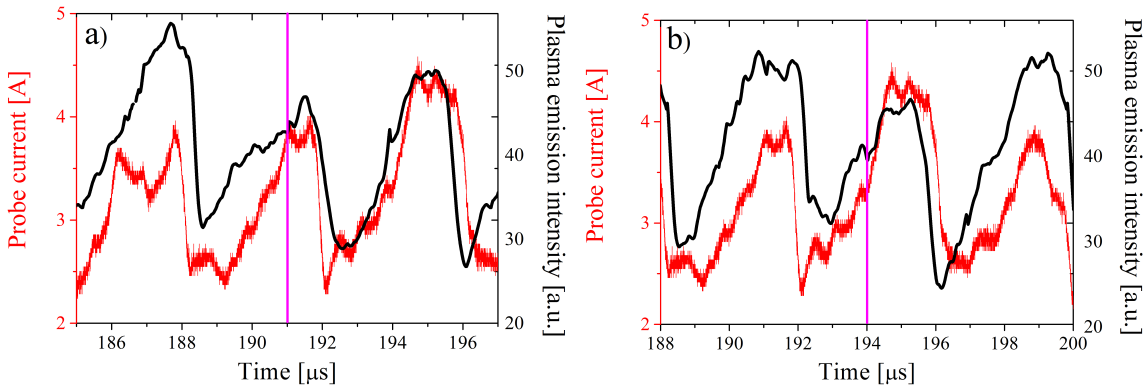

Fig. 5.11 Transformation of 2-D optical intensities shown in figure 5.6 to 1-D time traces (black) together with the corresponding strip probe (probe 1 in figure 5.2a) waveform (red) for an operating pressure of 0.14 Pa and average discharge power of $E_p = 9.6$ J at an instantaneous discharge current of 210 A and cathode voltage of 628 V. The vertical violet lines at time of 191 μs (graph a) and 194 μs (graph b) indicate times when the original images in figure 5.6 were taken.

This similarity indicates that the strip current and the optical emission from the spoke are somehow linked or share a common source. In a simplistic view, we consider the strip probe current I_p to be determined by the availability of charged particles above. The availability of charged particles is given by the Bohm criteria where the current through the sheath is proportional to $n_e {T_e}^{1/2}$, for a plasma density n_e with electron temperature T_e.

The optical emission is less clearly defined, however. Once again taking a simplistic view, it can be assumed that a more dense plasma will have a higher density of ions emitting photons, and therefore a higher optical emission. This simple relationship gives a linear relationship between optical emission intensity and n_e. There must also be a factor of T_e in

optical emission as a plasma with higher energy electrons (higher T_e) radiate more highly, but this relationship is not necessarily linear. Therefore it is proposed that the emission intensity is correlated with $n_e T_e{}^n$. Given the close correlation to I_p seen in figure 5.11, it is proposed that n $\sim$1/2.

From these two direct comparisons, it can be seen that the imaging and strip probe methods produce very similar results. However the techniques are also complementary, as the strip probes detect perturbations in a specific region for the entire pulse, whereas the camera observes the whole target but does so only for a very short moment of time.

Changes in the spoke mode number

Many of the findings in this chapter have been related to the mode number of spokes; in particular, how the mode number changes throughout the pulse and with varying pressures, I_d and E_p. In this sub-section, the mechanism whereby the mode number changes is investigated, using both imaging and strip probes.

Spoke merging (system two)

The existing hypothesis of merging spokes was proposed by Hecimovic et al [86] and states that consecutive spokes merge as the discharge current grows and spokes duly enlarge. This results in increased local sputtering of the target and higher buffer gas rarefaction. The lack of buffer gas atoms slows the ionization rate, causing the following spoke to shrink, while providing less stopping power for electrons, allowing the smaller spoke to catch up with the larger one. This leads them to unite to form one large spoke.

The merging of spokes in our setup can be observed with the simultaneous use of optical imaging and strip probe monitoring, as shown in figure 5.12 for an operating pressure of 0.14 Pa, pulse average power of E_p = 9.6 J and instantaneous discharge current of 210 A. In this case, the initial mode number is m = 3, with spokes identified as 1, 2 and 3. When we look again 3 μs later, spokes 2 and 3 have merged.

It can be observed that the latter two spokes (2 and 3) had very similar maximum plasma emission intensities before the merging process (see figure 5.12a). In the merged spoke (figure 5.12b), the plasma emission intensity is redistributed and its maximum is at the trailing edge of the spoke. The same pattern can be deduced from the strip probe waveforms in figure 5.12 c, with the current maxima of the leading spoke vanishing and the resulting current waveform resembling a single larger triangular shape. Spoke number 1 did not change its shape during the 3 μs delay time between the images shown in figure 5.12 a and b. The

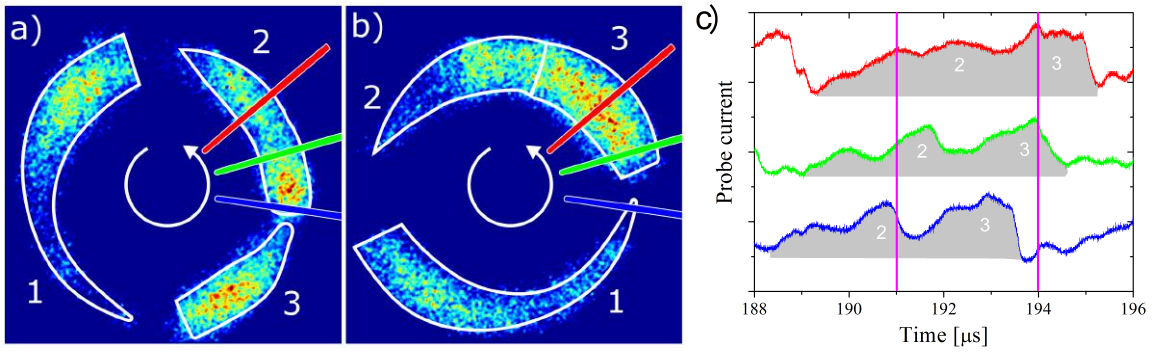

Fig. 5.12 In a) and b) two consecutive plasma emission images (3 μs apart) from one single pulse and c) the corresponding current waveforms from all three strip probes for an operating pressure of 0.14 Pa, pulse average power of E_p = 9.6 J, an instantaneous discharge current of 210 A and cathode voltage of 628 V. The vertical violet lines at time of 191 μs and 194 μs indicate times when the optical images a) and b) were taken.

angular shift between the trailing edges of the spoke 1 in figure 5.12a and figure 5.12b is 95° degrees.

The same angular shift is determined between the trailing edge of spoke 3 (figure 5.12 a) and the trailing edge of the merged spokes 2 and 3 (figure 5.12 b). Therefore it appears that spokes maintain their velocity during the merging process. This is in contrast to the mechanism proposed by Hecimovic et al [86], where the trailing spoke catches up with leading one due to its increased velocity. Our results imply that spoke merging may instead be due to azimuthal enlargement of the spoke (diffusion) in a reference frame rotating with spokes.

Spokes splitting (system two)

In our experiments, the number of spokes increases with the increase of the discharge current during a HiPIMS pulse, (figure 5.4). There seems to be two possible scenarios for the increase in the number of spokes: 1) spontaneous spoke creation in which a new spoke appears in a gap between two neighbouring spokes in order to provide the necessary ion current to the target; 2) a large spoke separates into two parts as it rotates. The former possibility however has not yet been detected, while the latter is reported [86].

In this study, spoke splitting is readily observed both optically and electrically [86], with a typical example shown in figure 5.13 a and b for an operating pressure of 2 Pa, a pulse average power of E_p = 11.6 J and an instantaneous discharge current of 220 A. The spoke in question is a well-developed triangular spoke identified as 1 in figure 5.13 a. In the time it takes to reach the red strip probe from the blue one (3 μs), the spoke has clearly split. In fact,

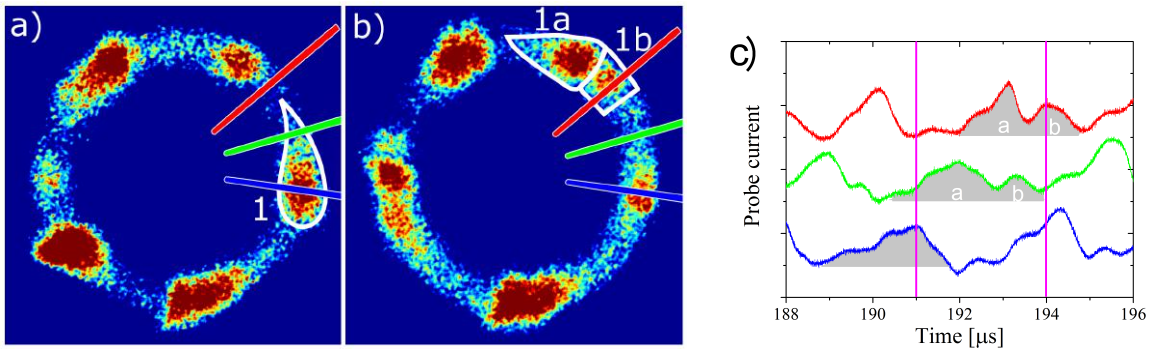

Fig. 5.13 In a) and b) two consecutive 2-D broadband emission images of the target from one single pulse and c) the corresponding current waveforms from all three strip probes for pressure of 2 Pa, pulse average power of E_p = 11.6 J, instantaneous discharge current of 220 A and cathode voltage of 580 V. The vertical violet lines at time of 191 μs and 194 μs indicate times when the optical images a) and b) were taken

differentiation of the structure begins at the green strip probe (1.5 μs) with the identification of two maxima in the strip probe current (figure 5.13 c). At this point, the leading maximum is more pronounced than the trailing one. As the spoke evolves from this point, the first maximum intensifies further and narrows in the azimuthal direction, while the trailing peak somewhat broadens. The total charge collected by the strip probe from the spoke corresponds to the area under strip probe signal depicted by grey colour in figure 5.13 c. For all strip probes, the total charge is the same. Thus, the charge is conserved during the spoke splitting.

5.4 Summary and Conclusions

The strip probe is a new diagnostic technique developed during this PhD which is able to measure the current drawn at a specific region of the target. In this chapter, the strip probe was used to detect perturbations in the HiPIMS discharge for both an aluminium and niobium target, with the intent of using this new diagnostic to obtain unique information about spokes. The strip probe was also used simultaneously with a fast imaging camera. Spokes were first identified using fast imaging and this remains the most common method of spoke identification.

The strip probe current showed clear perturbation at certain conditions during the HiPIMS discharge. The frequency and conditions at which these modulations were observed, combined with the fact that modulations were not present in the total discharge current, lead to the conclusion that the perturbations are due to spokes. Moreover, observations by a fast imaging camera, used simultaneously with the strip probe, have confirmed that these

perturbations are due to the presence of regions of high ionisation rotating above the target (spokes). There is also no evidence of the strip probes disrupting the discharge.

The strip probes give the unique measurement of the current drawn by the plasma above the target. This allowed the magnitude of the perturbation in the local discharge current due to the spokes to be measured for the first time in this experiment. The modulations were found to have a maximum amplitude of $\geq 50\%$ above its base value; this new finding contradicts some proposed models of spokes in which the spoke carries up to 100% of the total discharge current [87].

Strip probes were also used to track the velocity of the spokes throughout the pulse evolution. Fast imaging has been previously been used to measure spoke velocity; however, this method cannot make continuous readings throughout the pulse in the way that a strip probe can. It was found that when using an aluminium target at higher pressures of argon $\sim$0.69 Pa, the spokes' velocity approximately matches CIV for both argon and aluminium. The spoke velocity did appear to exceed the argon CIV towards the end of the pulse, and this is believed to be an effect of a changing r_0 reducing the distance the spoke travels, appearing to raise the velocity. However, at lower pressure, 0.18 Pa with a niobium target, the spoke velocities are far higher then the CIV, although similar spoke velocities have been observed at lower pressures.

New and different ways of plotting the measured strip probe current were shown; the strip probe current was plotted as an image and the camera images was shown linearised to match the strip probe current. These were found to match very closely; this new data led us to theorise that both I_p and optical emission are proportional to $n_e T_e^{1/2}$.

The strip probe has also been used in this chapter to investigate the splitting and merging of spokes. Observation of spoke merging, using for the first time the strip probe to measure the change in local current density during a spokes merging, has led to an updating of the existing theory. In the existing theory spokes are viewed as reducing in size and speeding up; however measurement of the local current density showed no reduction in size, leading to a new theory in which one or more spokes spread around the track.

Spoke splitting was also observed using both the strip probe and the ICCD camera. These results show spokes split to increase mode number with no cases of spontaneous spoke creation observed, supporting existing theory.

Chapter 6

Depositing niobium films

6.1 Introduction

Niobium is a superconductor, used in the construction of particle accelerators, specifically in superconducting radio frequency (SRF) cavities [11]. These cavities carry a resonant RF signal, creating a strong electric field which accelerates the ions or electrons. The RF signal is very high power with a high duty cycle; under these condition, non-superconducting cavities would be melted by the high power [116].

Normally, SRF cavities are made from bulk niobium [12]. However because the RF signal does not penetrate very deeply into niobium, in theory a thin niobium film, on a bulk cavity of copper (or other materials with desirable properties), would function as a SRF cavity [117].

Since the 1980s, there have been attempts to use niobium films coated onto copper instead of bulk niobium, as the films have better thermal and accelerator properties [13] ([116] and references there-in), but the use of coatings have yet to become standard in this application.

Attempts have been made to use DC-MS to create thin films however none have sufficiently improved on the bulk niobium cavities to become standard [118] [119] ([116] and references there-in). Later HiPIMS was tested [117]. As a form of ionised PVD (IPVD) HiPIMS has been shown to have some advantages over conventional sputtering [21], though it also has a lower deposition rate [120].

HiPIMS has long been known to produce high energy ions [121]; however until recently their origin was unknown. High energy ions have been shown to be advantageous, improving film density [122] and promoting growth [52]. To obtain the benefits of high energy ions, however, usually requires sample biasing [24]. The HiPIMS discharge has an ion energy

distribution function containing higher energy ions than the DC case as well as containing more of theses high energy ions. This increases the benefit of sample biasing [52].

The discovery of spokes [81] and the linking of spokes to high energy ions [29] represents the opportunity for a step forward. Work in chapter 5 as well as work by others [23] [39] [36] has shown that spoke behaviour changes with different backing gas pressures and pulse energies. Backing gas type and target material also has a strong effect on spokes [84]. In most cases, the spokes are chaotic at low powers and are not fully formed (the chaotic regime); however, as the power and pressure increase, the spokes become more stable and regularly repeating (the coherent regime). Eventually when the power and pressure are increased further the spokes disappear completely (the spokeless regime). These regimes of spokes have been associated with changes in the deposition rate [104] and ion energy [23] [103].

Additional spokes have been linked to ions of high energy given out in the direction parallel to the plane of the target [123] [103] [124]. The effects of these high energy ions from spokes, or ions given out to the side, on films have not yet been tested, except in general studies of HiPIMS [34] [124]. In particular, no specific investigations into the effect of spokes' regimes on the thin films themselves have been made.

This chapter will be devoted to the investigation of different conditions of spokes and their effect on the (unbiased) thin films that they deposit. In order to do this, first the spokes' conditions in response to current and power must be identified. Once this has been completed, a set of samples can be made at these conditions, at a set of angles to the target, to investigate the ions given off directly from the target and to the sides. These samples can then be analysed to see the effect of the spokes on film quality at different angles of deposition.

The chapter starts with this brief introduction, followed by a description of the experimental setup section. The results and analysis will be split into two sections; the first detailing the investigation into the spokes' conditions using the strip probe (described more fully in Chapters 4 and 5) and the second detailing the creation of a set of niobium thin films at a set of angles to the target and their analysis by focused ion beam (FIB), scanning electron microscopy (SEM) and x-ray diffraction (XRD).

6.2 Experimental setup

This experiment is conducted in two parts. Both used system one, described in chapter 3: the first part uses a segmented target to analyse the amplitude and regimes of spokes. The second created a series of films in the different regimes and the DC case, for a set of angles. These samples were then analysed to reveal the effects, if any, of the different conditions.

The film analysis was all done off-site, as it requires specialist equipment. Scanning electron microscope (SEM) and focused ion beam (FIB) was done at the Nanoinvestigation Centre at Liverpool, part of the University of Liverpool. XRD (X-ray diffraction) was also performed off-site at Manchester University, School of Materials. The SEM, FIB and XRD were all performed by third party researchers, the SEM and FIB by Dr. Tobias Heil and the XRD by Mr. Taaj Sain.

Spoke regimes setup

Setup system one, as described in section 3, is a purpose-built cylindrical vacuum vessel, 300 mm in length and 260 mm in diameter, pumped down to a base pressure of $< 10^{-3}$ Pa using a turbo molecular pump backed by a rotary pump. Argon was introduced into the vessel with flow rates ranging from 0 to 50 sccm (standard cubic centimetre per minute), determined and controlled using a capacitance pressure gauge (MKS 628A) and a mass flow controller (MKS 1179A) respectively. The general chamber configuration is shown in figure 6.1a. The magnetron used in this study was a circular unbalanced type, equipped with a 75 mm diameter niobium target of 6.35 mm thickness and 99.99% purity (racetrack = 21.5 $\pm$ 0.5 mm radius). Power supply B with a simmer source, as described in chapter 3, was used providing a maximum on-time power of 50 kW operated at a repetition rate of 1 Hz and a pulse width of 100 - 200 μs providing energies up to 10 J per pulse. This setup used three strip probes, as described in chapter 4. The three 2.00 $\pm$ 0.02 mm wide flush-mounted aluminium strip probes (with the same purity as the target) were placed in machined slots at 3 angular positions 25° around the target, see figure 6.1b.

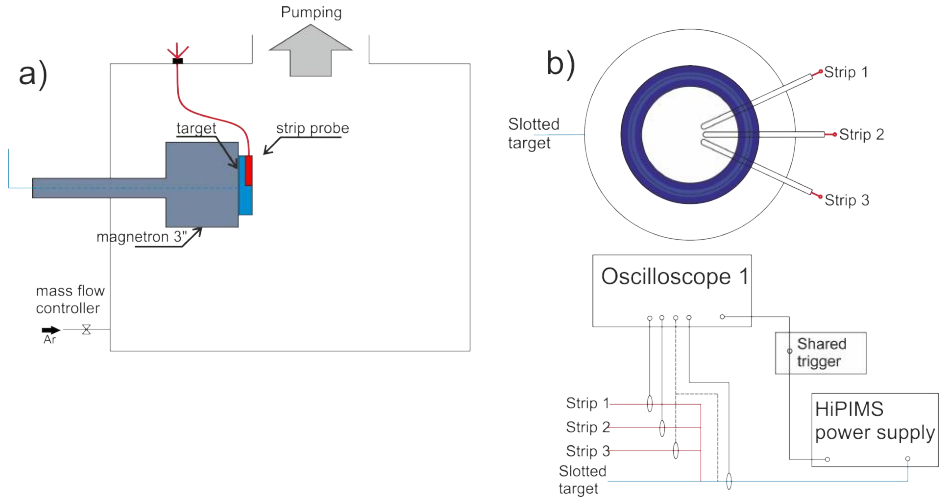

Fig. 6.1 Schematic diagrams of a) the magnetron and chamber set-up and b) the strip probes, power supply and current measuring arrangement.

The three strip probes filled the entire target track radius and extended past the target edge by 5 mm to allow electrical connections. The strip probes were electrically isolated from the rest of the target by a thin layer of polyimide tape of thickness of 0.07 ± 0.01 mm, placed around 3 sides of the probe, which provided a tight fit. This insulation thickness defined the gap between the strip probe and the target. The three strip probes were connected directly to the power supply as shown in figure 6.1b. In this configuration, they always remained at the same potential as the target, but with their contribution to the total current measured separately using Pearson current probes (Model 2877 with 1 V/A). The total target current, I_d, was measured using a larger Pearson probe (Model 3972 with 0.1 V/A). The four current waveforms were recorded using a digital oscilloscope (Tektronix DPO 3034 with 300 MHz bandwidth) in a single short mode, if not otherwise stated. The discharge voltage waveforms V_d were measured separately using a high voltage probe (Tektronix P5100) and in cases where both I_d and V_d need to be recorded, V_d replaces I_{p3}. This is shown in figure 6.1b.

Deposition setup

Deposition was performed in the same chamber and with the same instrumentation and HiPIMS power supplies setup, in addition an Advance Energy MDX 1.5 K supply to supply DC power when needed. Once the conditions of the spoke regimes have been identified a series of films, at a set of angles, are to be deposited in each region. To enable deposition at these different angles, an aluminium sample holder consisting of a full ring with two semi-circular arches intersecting at 90° such that samples could be held at 90°, 45° and 0°, relative to the centre of the rings was used. This ring was placed with the centre of the full ring 20 mm in-front of the magnetron centre as is shown in figure 6.2a. This means that samples can be held either facing the target centre directly (referred to as directly facing) at ∼45° (referred to as 45°) or perpendicular to the target 20 mm above it (referred to as side-on). The sample holder is such that only one sample can be made facing the target directly, while four can be made at both the side-on and ∼45° positions. The sample holder position is shown in figure 6.2a, as are the samples' position and numbering in figure 6.2b.

The sample positions are such that samples no. 1 to 4 (side-on) are 120 mm away from the target centre at 9°, samples no. 5 to 8 (45°) are 135 mm from the target centre at 45° and sample no. 9 is 140 mm from the target centre directly facing it, as shown in figure 6.2b. These differences in distance are an unavoidable result of the 20 mm distance between the target centre and the ring centre. This distance is maintained to avoid shadowing from the 3 mm raised target guard needed to keep the target in place (described in chapter 3).

The niobium was deposited onto silicon samples ∼10 mm square. The silicone was prepared by washing in acetone and then isopropanol in a sonic bath, before being dried with

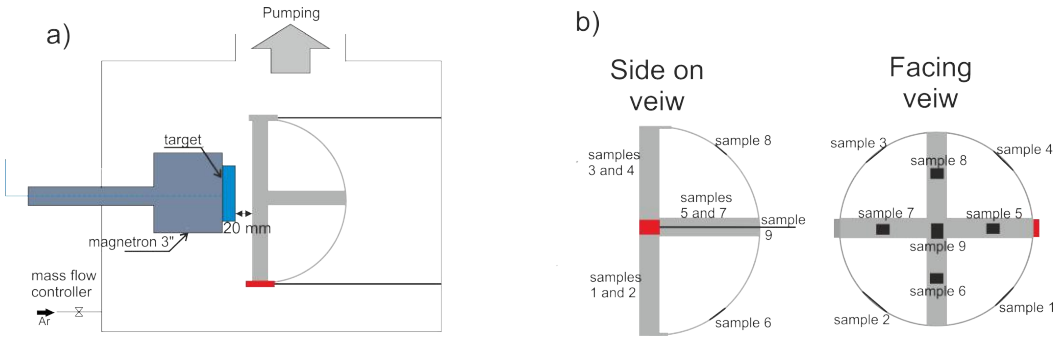

Fig. 6.2 Schematic diagrams of a) the magnetron and chamber with the deposition ring positioned as viewed from the top and b) the position of all samples on the deposition ring.

compressed air. The deposition ring has no cooling or heat apparatuses and was not biased, but conducting and in contact with the chamber wall and unified ground. Consequently the films are considered to be created at room temperature and 0 V bias. the plasma and deposition is expected to cause some heat effects however in similar experiments, on different system able to measure this heating effect, the temperature did not exceed 350 °k.

The sample deposition rate was found using a FIB; the film was cut away in one area by a focused ion beam. An image of the cut was then taken at 45°, from which the film thickness could be measured. A non-FIB set of SEM images was also taken at a normal to the surface and from this, the surface morphology was investigated. Furthermore XRD was used to investigate grain alignment and lattice dimensions.

6.3 Spoke regimes for an argon-niobium plasma

In chapter 5, strip probes were tested and established as a diagnostic technique for investigating spokes [90]. As part of this, the strip probes were used to draw a contour plot showing the variation of spoke amplitude, relative to the base strip probe current, as the pulse power and pressure of the HiPIMS discharge were changed. The strips were also successfully able to distinguish the three different regimes of spokes: chaotic, coherent and spokeless [36] [23]. The approximate boundaries at which these regimes transition is shown on the contour plot in chapter 5.

In this section, we further develop this technique to find a repeatable method of constructing a similar contour plot or set of contour plots for an argon-niobium plasma, which can then be used for depositing films at different spoke regimes and amplitudes.

The previous method

The contour plot in chapter 5 was produced by drawing an envelope around the oscillation in I_p and measuring ΔI_p, the current width of this envelope, against the minimum probe current of the envelope I_b. This was done at the time when the spokes were at a maximum t $\sim$40 μs. This method requires individual envelopes to be drawn around each I_p for them to be analysed, making analysis by this method labour-intensive as well as introducing two major flaws: First, the subjective judgements on whether certain peaks are outliers or not; and second, that the spoke amplitude is only measured at one specific time. These flaws are illustrated in figure 6.3

Figure 6.3 shows I_p from strip probe two (figure 6.1b) for a discharge at pressure 0.33 Pa, E_p = 4.2 J with a 100 μs long pulse. Figure 6.3a shows two oscillation envelopes; the blue envelope is drawn such that the extremely high/low peaks are disregarded as outliers, whereas the red envelope is drawn such that the high/low peaks are included. It can be seen that the two envelopes drawn by this method produce significantly different values, depending on which peaks are considered to be outliers, with the red envelope giving $\Delta I_p/I_b$ = 0.63 and the blue giving $\Delta I_p/I_b$ = 0.34.

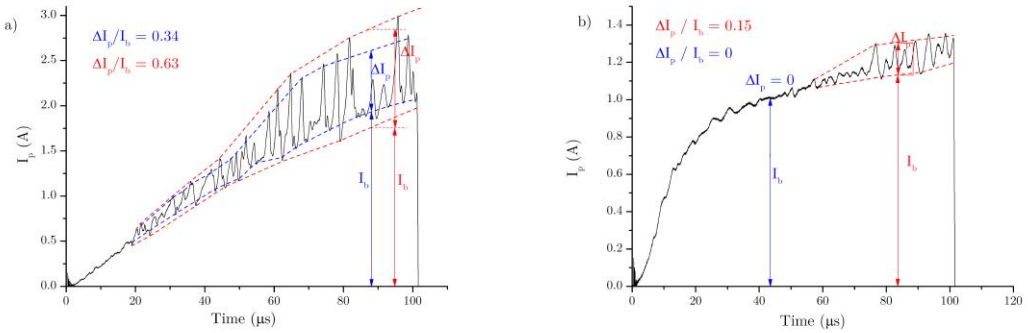

Fig. 6.3 Illustrating two shortcomings of the method used to calculate spoke amplitude in chapter 5, a) the subjectivity of the spoke envelope illustrated for a I_p at pressure, 0.33 Pa and E_p = 4.2 J, the minimum and maximum spoke envelopes and the calculated $\Delta I_p/I_b$ included and b) I_p at pressure, 1.3 Pa and E_p = 4.2 J $\Delta I_p/I_b$ calculated at t $\sim$40 μs and $\sim$80 μs with its values at both positions shown.

The second shortcoming of the method used in chapter 5 is that the width of the oscillation envelope (both absolutely and relative to I_b) varies throughout the pulse. Indeed, as can be seen in figure 6.3b, at some conditions the spokes only become visible near the end of the pulse. For the conditions of pressure 1.3 Pa and E_p = 4.2 J shown in figure 6.3b, depending on the time at which $\Delta I_p/I_b$ is measured the spoke could be considered spokeless or coherent.

This is shown in figure 6.3b with $\Delta I_p/I_b$ measured at ∼40 and ∼80 μs, where $\Delta I_p/I_b$ is zero at ∼40 μs and 0.15 at ∼80 μs.

Therefore in this chapter a new method is developed to give more consistent and objective results, and over a time range rather than at a specific time.

The new method

This section describes the MatLab program used in this chapter to calculate $\Delta I_p/I_b$ from the 10 000 data point current time trace output from the oscilloscope. The program consists of several steps. The first selects an appropriate range over which the spokes can be measured; as was seen in chapter 5 and figure 6.3a and b, true spokes do not form until later in the pulse, and require a time (t_{ramp}) ∼30 μs in figure 6.3a. However, this depends on conditions (with pressure being the major factor) and the maximum t_{ramp} under our conditions was t_{ramp} ∼40 μs. As the same time range is applied to all pulses, the time range t_{ramp} = 40 μs to pulse end, is chosen.

The element of modulation in I_p due to spokes is separated in the second step. I_p is the local target current density, and as such it is affected by changes to the total discharge current density, as well as to the presence of spokes. These two factors are separated by using a moving average smoothing function on I_p over the time range selected in step one. This is sufficient to remove the spoke, but leave the larger trends. The moving average smoothing function requires ∼500 points (∼5 μs , depending on the scale) to proceed in order to produce an acceptable smoothing. This reduces the time range over which this method can be measured to between 45 μs and 5 μs before the pulse end. Subtracting I_p from the smoothed I_p gives the pure spokes' modulation component of I_p in this new time range.

I_b and ΔI_p are calculated from finding the local maxima and minima in the pure spokes component of I_p in the desired time range. This time range can be altered to any range inside that to investigate $\Delta I_p/I_b$ at specific time ranges. Because of the unusual distribution of maxima and minima in the pure spoke component of I_p, a simple average of maximum and minimum did not yield satisfactory results. An arbitrary factor was introduced such that the calculated maximum and minimum matched the data. To check that the function then gives the appropriate values of ΔI_p and I_b, the values are checked by visual inspection.

As this new method is automated, it can be used to analyse a lot of results relatively quickly to give a high degree of accuracy. Here this method is used to analyse all three strip probe currents over ten repetitions per condition.

Contour plots

The contour plots were chosen from a set of 5 pressures varying from 0.33 to 1.7 Pa in steps of 0.33 Pa and average target on-time powers from 18 kW to 50 kW (0.39 to 1.1 kW cm^{-2}) in steps of 16 kW (0.35 kW cm^{-2}). These ranges of values covered all three regimes of spokes. The first contour plot, figure 6.4, shows $\Delta I_p/I_b$ against pressure and E_p for a 100 μs pulse calculated by the old method at t = 50 μs. This figure can be compared to figure 6.5, a contour plot of $\Delta I_p/I_b$ against pressure and E_p again, also for a 100 μs. For figure 6.5, the time range t = 45 to 95 μs is calculated by the new method. Figures 6.4 and 6.5 are different, though not completely dissimilar. The reasons for this difference is explained in the previous sections. It should be noted that the visual inspection performed on individual plots strongly indicates that figure 6.5 is a more accurate representation of the data. Because of this, discussion of contour plots henceforth will be based only on the new method.

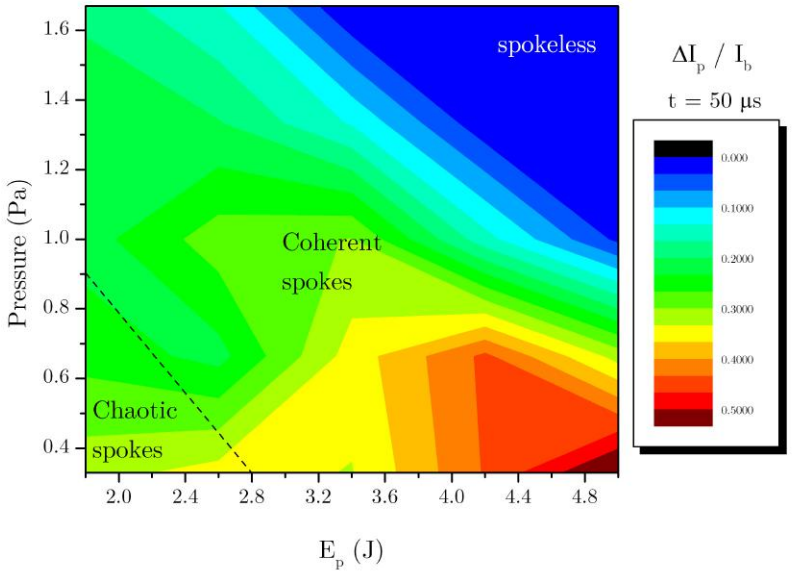

Fig. 6.4 A contour plot showing $\Delta I_p/I_b$ for a set of 100 μs pulses with pressure varying from 0.33 to 1.7 Pa and E_p from 1.8 to 5 J. With $\Delta I_p/I_b$ measured at t = 50 μs calculated by the method in chapter 5. Also shown are approximate boundaries separating the chaotic, coherent and spokeless regimes.

Figure 6.5 has many features in common with the contour plot for aluminium, despite the different methods used. Because of the full range of powers available in figure 6.5 (but not in the contour plot for aluminium), the patterns can be seen more clearly. It can be observed in figure 6.5 that there is an optimal level of power at which spokes have a peak

amplitude, though this optimum changes with pressure; increasing the pressure has the effect of diminishing the spokes in all cases.

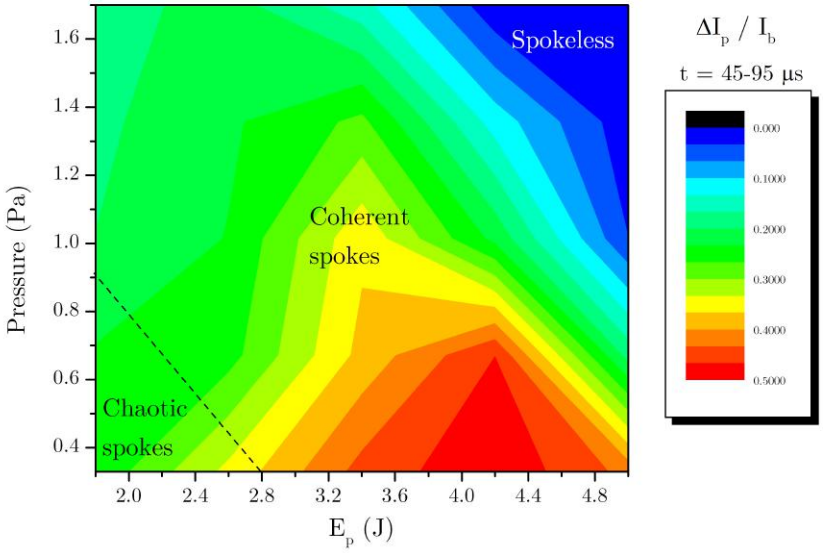

Fig. 6.5 A contour plot showing $\Delta I_p/I_b$ for a set of 100 μs pulses with pressure varied from 0.33 to 1.7 Pa and E_p from 1.8 to 5 J. With $\Delta I_p/I_b$ averaged by a function between 45 and 95 μs. Also shown are approximate boundaries separating the chaotic, coherent and spokeless regimes.

As demonstrated in figure 6.3b, the amplitude of spokes changes through the discharge, which implies that the discharge over different ranges would be expected to be different. Figure 6.5 shows the maximum range over which spokes can be meaningfully measured 45 - 95 μs. Figures 6.6a and b show the first and last 25 μs in the range 45 - 95 μs (45 - 70 μs and 70 - 95 μs) to show the differences between these time ranges.

It can be immediately seen that figure 6.6a is the most similar to the aluminium parameter scan in chapter 5. This is as one would have expected, given that spokes in aluminium were calculated at ~40 μs. However, this suggests that all target materials have the same general pattern though the power and pressure at which they occur may vary. However, more experimentation is required to prove this proposition.

The effects shown in figure 6.3b, with the spoke only emerging later at higher pressure, is illustrated by the fact that figure 6.6a has a larger spokeless region then figure 6.5, extending most obviously at the higher pressure region. Figure 6.6b is more similar to figure 6.5. Taking both plots in figure 6.6 as a whole, it can be seen that power has a greater effect on $\Delta I_p/I_b$ at earlier times (45-70 μs), with pressure having the same effect at all times.

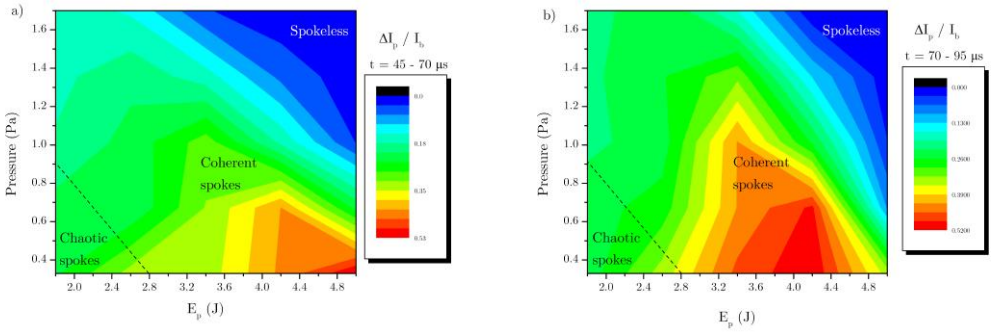

Fig. 6.6 A pair of contour plots showing $\Delta I_p/I_b$ for a set of 100 μs pulses with pressure varied from 0.33 to 1.7 Pa and E_p from 1.8 to 5 J. With $\Delta I_p/I_b$ averaged by a function between a) 45 to 70 μs and b) 70 to 95 μs.

The purpose of this experiment is to investigate the effects of spokes on thin films. As can be seen from figure 6.3, the initial ~30 μs (depending on conditions) are free from spokes. It follows that pulses where spokes are present for longer times would be desirable to study the effects of spokes on deposited films. To this end, 200 μs long pulses are studied, as this is the longest pulse length which can be constantly supplied by the power supply.

Figure 6.7a shows a contour plot for a 200 μs pulse with spokes measured from 45 - 195 μs. It can be seen that the figure 6.7a, while similar to figure 6.5, has a more notable central optimal power at 34 kW (at E_p = 6.8), which does not change, and this effect also remains visible at higher pressures. Figure 6.7b shows the contour plot in a 200 μs pulse with the spoke amplitude calculated over the same range as figure 6.5. There are notable differences between figure 6.5 and 6.7b. Figure 6.7b has a larger spokeless region and shows a pattern less indicative of an optimum power and more of a maximum spoke amplitude at higher powers, although these are more similar to figure 6.5 than in figure 6.7a.

The differences observed between figure 6.5 and 6.7b are explained by the differences in I_d seen in figure 6.8. While the average pulse powers are the same for both pulses, there is a set t_{ramp} as the current I_d grows from zero. In both the 100 and 200 μ pulses, t_{ramp} is approximately the same at the same conditions. However t_{ramp} is a longer proportion of the short pulse; therefore to compensate, I_d post-ramp must be higher to produce the same average.

Given that higher pressures have been associated with a higher current, one might imagine a system where pressure causes I_b to increase, reducing $\Delta I_p/I_b$ to the point where the spokes disappear. However, as can be seen from figure 6.9a of I_p at E_p = 10 J for a set of pressures, the effect of pressure seems to limit the height of the peak I_p, rather than raise the valley I_b.

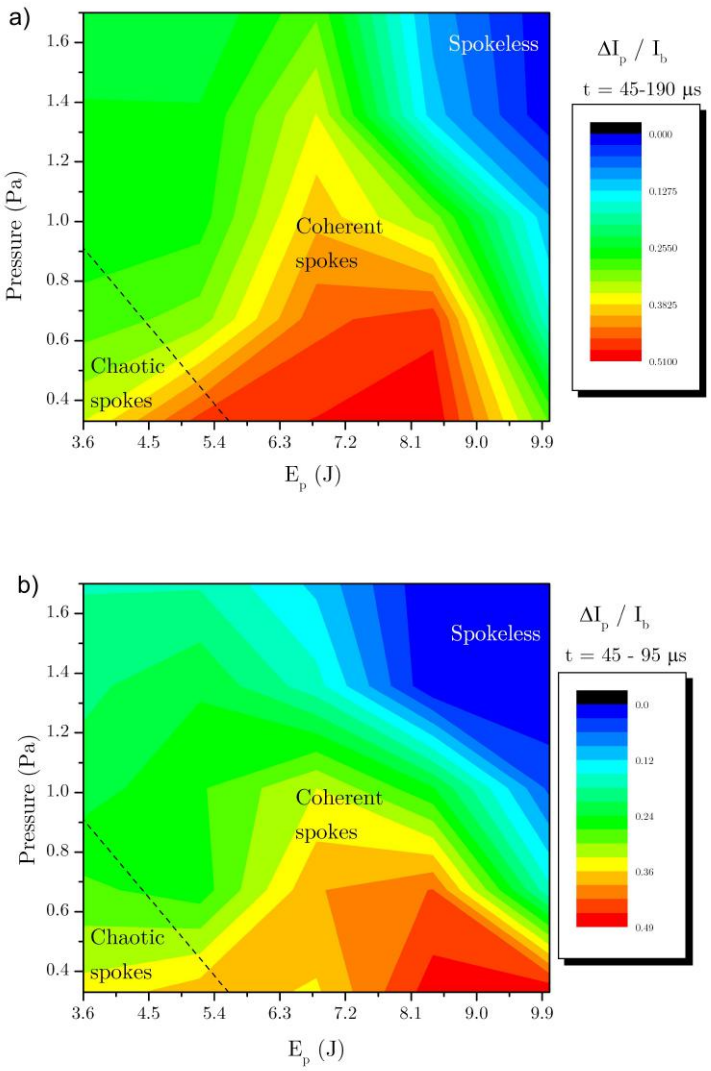

Fig. 6.7 A pair of contour plots showing $\Delta I_p/I_b$ for a set of 100 μs pulses with pressure varied from 0.33 to 1.7 Pa and E_p from 3.6 to 10 J. With $\Delta I_p/I_b$ averaged by a function between a) 45 to 195 μs and b) 45 to 95 μs.

The 1.7 Pa condition is not included in figure 6.5a; it follows the same trends as the 1.3 Pa condition, but at a higher current and thus obscures the image.

Figure 6.9b shows I_p at 1 Pa for a set of E_p. It can be seen that as E_p grows, so does the amplitude of the spoke. However the peak I_p does not exceed I_p drawn by the spokeless conditions; this would explain the optimum power effect seen in the contour plots. This effect holds true for all pressures where the spokeless condition is observed.

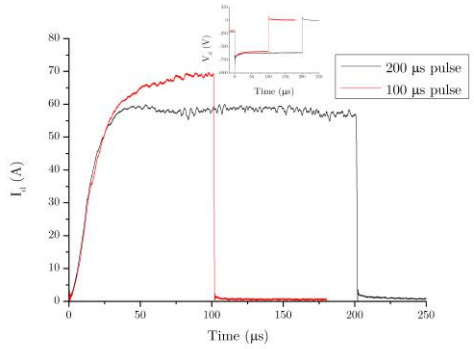

Fig. 6.8 I_d for a 100 and 200 μs pulse with V_d shown, at pressure 1 Pa E_p = 3.4 J and 6.8 J.

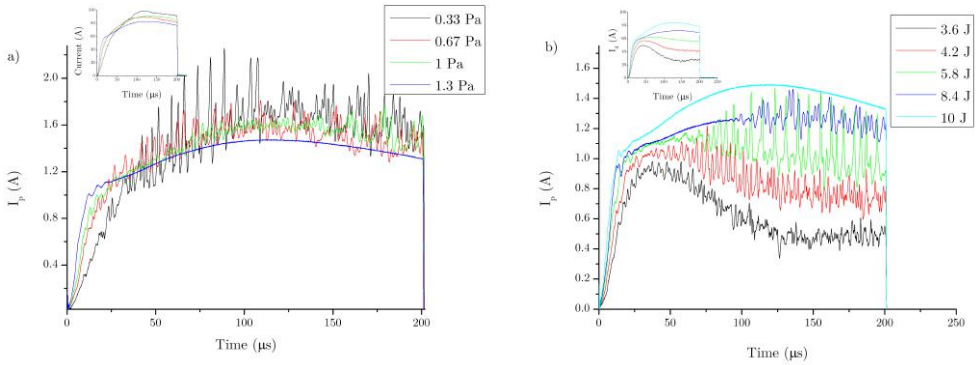

Fig. 6.9 I_p for a) a set of pressures at E_p = 10 J and b) a set of E_p at a pressure of 1 Pa. I_d is included for both figures.

Figure 6.9 gives us insights into the factors causing the form of the contour plot. At low powers and pressures, the spokes are chaotic and low in amplitude, but the spokes become coherent as the power increases, and this allows their amplitude to grow. However because I_p in the coherent regime does not exceed I_p in the spokeless regime, the spoke amplitude cannot grow indefinitely. Spoke amplitude reaches a maximum when this limiting effect first becomes a factor. Increasing pressure lowers the power required to achieve the spokeless condition, and hence increasing pressure has the effect of lowering the peak spoke amplitude. As a result, one can identify an optimum power at which spokes' amplitude is at a maximum for every pressure.

From these results a range of conditions for a 200 μs pulse representing the chaotic, coherent and spokeless regimes are chosen.

- The chaotic condition is at pressure 0.33 Pa E_p = 3.6 J.
- The coherent condition is at pressure 0.33 Pa E_p = 6.8 J.
- The spokeless condition is at pressure 1.7 Pa E_p =10 J.

An argument could be made for using a pressure of 0.33 Pa and E_p = 8.4 J for the coherent condition, however at E_p = 8.4 J there is an increased risk of arcing, which has a negative effect on films.

Spokes regimes in the deposition setup

The deposition ring shown in figure 6.2 will introduce a new and potentially disruptive source of grounding. Given our incomplete understanding regarding spoke formation and spoke regimes, it is important to study the effects of this grounding on the spokes.

Figure 6.10 shows I_p for all the chosen discharge conditions, measured both with and without the deposition ring. For figure 6.10a and b, the I_p obtained with the deposition ring has been given an arbitrary vertical displacement (+0.2 A for the chaotic figure 6.10a and +0.5 A for the coherent figure 6.10b), so the data could be directly compared. In figure 6.10c, no vertical displacement is used.

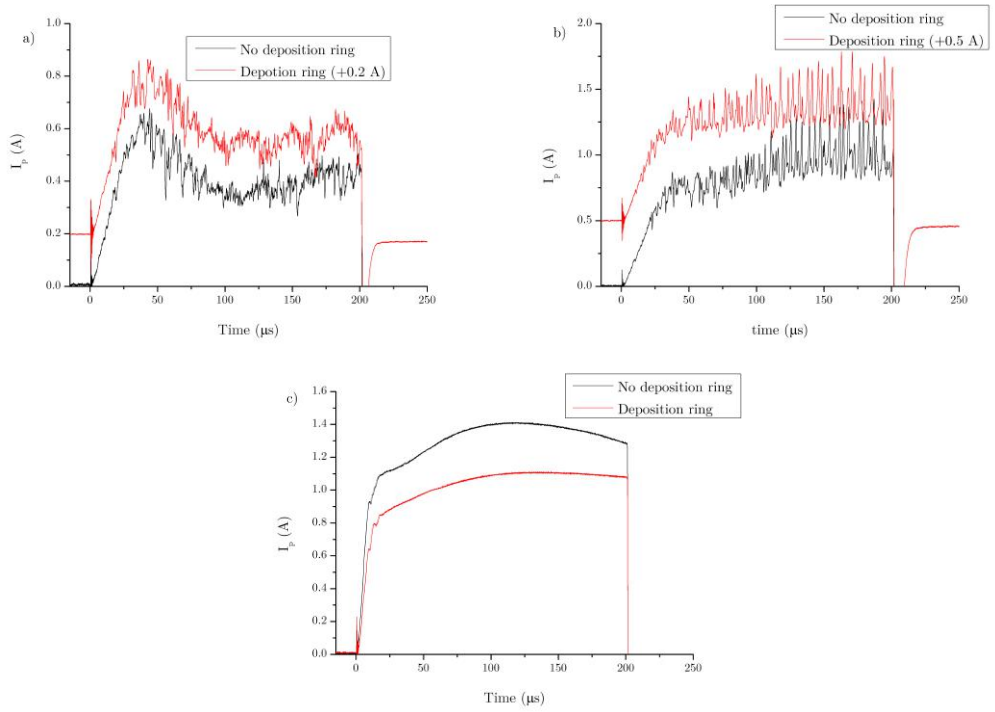

Fig. 6.10 I_p both with and without the deposition ring for a) pressure 0.33 Pa E_p = 3.6 J b) pressure 0.33 Pa E_p = 6.8 J c) pressure 1.7 Pa E_p =10 J.

The two I_p traces shown in figure 6.10a and b are not identical however. This is due to the unpredictable nature of spokes, whereby no two different pulses match exactly. Given this, the differences between figure 6.10a and b are not significant.

Figure 6.10c, the spokeless condition, however, does show a significant difference between I_ps which depends on whether the deposition ring is used or not. I_p without the deposition ring is significantly higher than I_p with the deposition ring. However both clearly show the discharge to be in the spokeless regime. This difference seen in figure 6.10c suggests that the presence of the grounding ring increases the racetrack radius (r_0). As described in chapter 4, because the strip probe is a slot rather than a wedge, this change in r_0 changes the percentage of the racetrack (which carries the majority of I_d) that passes over the strip. Therefore I_p receives an increased fraction of I_d.

The presence of the deposition ring seems to have little or no effect on either the chaotic or coherent discharge conditions. The spokeless discharge in figure 6.10c is somewhat affected, probably as a result of the grounding ring changing r_0. However, given the focus of this study is to investigate spokes rather then racetrack radius, it is concluded that the deposition ring does not change the spoke regime.

6.4 Deposition

Deposition conditions

The deposition was setup as described in section 6.2, with 9 samples for each condition (the conditions are chosen to represent each regime of spokes) at positions shown in figure 6.2. In addition to the three spoke regimes, DC samples are depositioned at both 0.33 and 1.7 Pa. All samples are deposited for 3 hours 30 minutes at 250 W average power, and the repetition frequency f of the HiPIMS discharge is varied so that pulses of different E_p can have the same averaged power. The full set of conditions are given below, with f and average current (I_A) for the full pulse cycle (off and on times) included:

- The chaotic condition, at pressure 0.33 Pa, E_p = 3.6 J, f = 70 Hz and I_A = 0.39 A
- The coherent condition, at pressure 0.33 Pa, E_p = 6.8 J, f = 37 Hz and I_A = 0.37 A
- The spokeless condition, at pressure 1.7 Pa, E_p = 10 J, f = 25 Hz and I_A = 0.34 A
- The low pressure DC, at Pressure 0.33 Pa, I_A = 0.7 A
- The high pressure DC, at Pressure 1.7 Pa, I_A = 0.9 A

I_d and V_d for the three HiPIMS discharges are shown in figure 6.11 averaged over 252 pulses, and the average on-time current is shown. No I_d and V_d traces are given for the DC discharge as it supplies a constant current rather than a pulse.

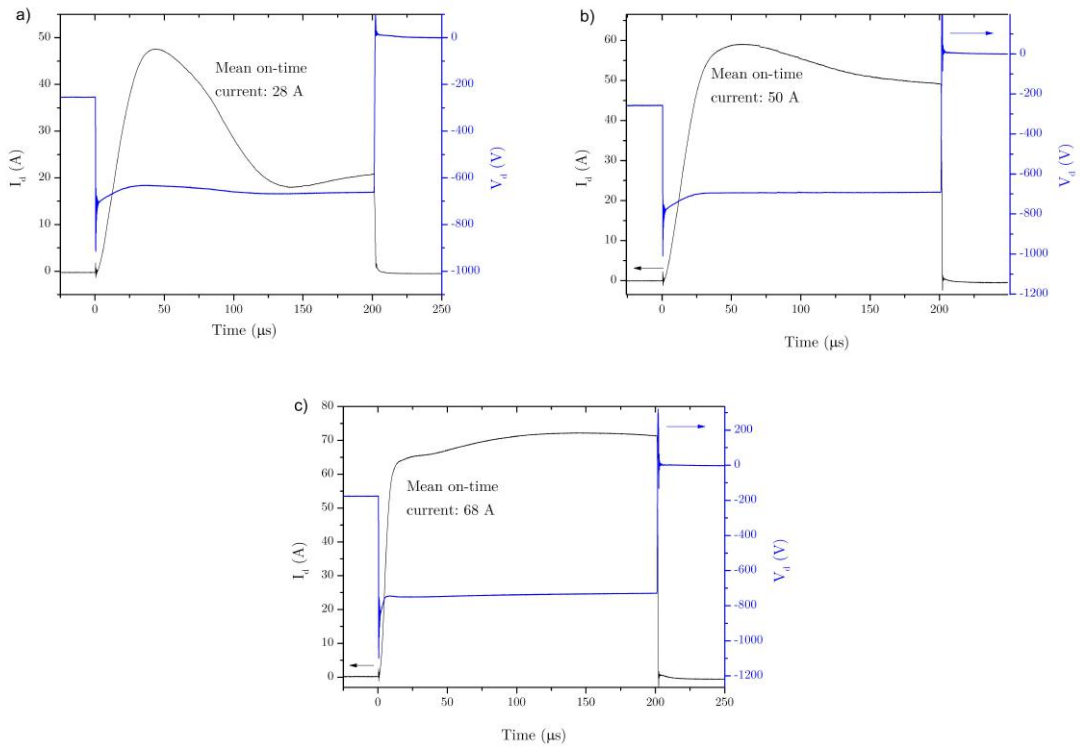

Fig. 6.11 The discharge I_d and V_d traces averaged over 252 pulses with average current per pulse shown for the a) chaotic b) coherent and c) spokeless condition.

Deposition rates

The first and most basic investigation is into the deposition rate. The deposition rate was determined from the SEM images of the samples using the FIB technique, which cuts away the film and then images are taken at 45° displaying a clear cut through the film to the substrate. The width of the film can then be measured from this image using the image scale and accounting for the 45° angle. The precision in this is limited by the pixel number; values are accurate to 3 significant figures. The thickness of all films is shown in table 6.1 in μm, alongside the averaged thickness at each position and condition.

Because all films were sputtered at the same power (250 W) and for the same time (3.5 hours), the results in table 6.1 can also be considered a deposition rate in units of μ per 250 W per 3.5 hours.

The deposition rate can be given in terms of either the total target power, or I_A. While all discharge conditions were performed at the same average power, they had different I_A. Table 6.2 shows the deposition rate in terms of nm of deposition h^{-1}(hour^{-1}) A^{-1}.

Sample No. / position	DC 0.33 Pa (μm)	DC 1.7 Pa (μm)	Chaotic (μm)	Coherent (μm)	spokeless (μm)
1	1.61	2.46	0.578	0.465	0.945
2	1.74	2.60	0.496	0.653	0.981
3	1.31	2.90	0.549	0.492	1.22
4	1.44	2.87	0.559	0.461	1.01
5	5.63	6.51	1.61	1.38	2.12
6	5.74	6.75	1.67	1.36	2.11
7	5.80	7.10	2.69	1.4	2.21
8	6.33	6.96	2.04	1.46	2.31
9	4.37	5.84	1.65	1.57	1.78
side-on	1.52	2.71	0.546	0.563	1.04
45°	5.88	6.83	2.00	1.40	2.19
directly facing	4.37	5.84	1.65	1.57	1.78

Table 6.1 The total film thickness for all samples at all conditions, with the average at each position.

It is useful to show results for all samples, in order to identify asymmetry in the chamber leading to positions where the local deposition rate is higher. While a slight preference can be seen for the samples in position 7 and 8, in general the sample thickness is relativity constant between samples at the same positions.

Sample No.	DC 0.33 Pa (nm h^{-1} A^{-1})	DC 1.7 Pa (nm h^{-1} A^{-1})	Chaotic (nm h^{-1} A^{-1})	Coherent (nm h^{-1} A^{-1})	spokeless (nm h^{-1} A^{-1})
1	658	781	422	411	794
2	710	826	362	577	825
3	536	920	400	434	1030
4	589	911	407	407	853
5	2300	2070	1180	1220	1780
6	2340	2140	1220	1200	1770
7	2370	2250	1960	1240	1850
8	2590	2250	1480	1290	1940
9	1780	2210	1210	1390	1500
side-on	623	860	398	457	876
45^o	2400	2180	1460	1240	1840
directly facing	1780	2210	1210	1390	1500

Table 6.2 The deposition rate normalised to I_A for all samples at all conditions.

It is apparent from Table 6.1 and 6.2 that the DC condition has a higher deposition rate than HiPIMS in all cases, as would be expected [77].

This effect is reduced by normalising the deposition rate to I_A rather than the average power. The deposition rate normalised to current in the spokeless condition is nearly the same as in the DC at the same pressure. Of the two DC conditions, the lower pressure condition has a lower deposition rate normalised to power, but a higher deposition rate normalised to I_A (at 45°). Of the HiPIMS conditions, the spokeless regime always has the highest deposition rate when controlled for both power and I_A. There is little difference in the deposition rates of the chaotic and coherent regimes.

The difference in deposition rates at different positions: Side-on (S-O) to target; 45° to target centre (45°); and facing the target centre (FT), can be seen in tables 6.1 and 6.2. However for a less complicated and sharper comparison, the average deposition rates from these positions are compared relative to each another, S-O and FT to 45° and S-O to FT, as is shown in Table 6.3).

The effect of pressure can be seen in Table 6.3 as both the spokeless and high pressure DC conditions have deposited over wider angles than in the low pressure condition. The chaotic condition also seems to have a deposition rate at a distribution similar to the DC case at the same pressure. However, the coherent regime shows the FT sample having the highest deposition rate, the only condition where this is the case, and it also shows a relatively high S-O deposition rate

Sample position ratio	DC 0.33 Pa	DC 1.7 Pa	Chaotic	Coherent	spokeless
S-O : 45°	0.26	0.40	0.27	0.37	0.48
FT : 45°	0.74	0.86	0.82	1.1	0.81
S-O : FT	0.35	0.46	0.33	0.33	0.58

Table 6.3 The ratio of the deposition rates at different positions for all conditions.

It was expected that the two cases with spokes would have a higher deposition rate to the side than the DC case, given the high energy ions observed being given out to the side,and attributed to spokes [28]. However as can be seen in table 6.3, this is not the case, pressure seeming to be a more important factor than the angle of the deposition.

SEM imaging

In this section, SEM images of the thin films are investigated since this represents the simplest way to investigate surface morphology. It is suggested that the high energy ion HIPIMS [25]

will lead to smoother, more dense films with small grains rather then a columnar structure. Here we look at all the sample conditions and positions to see if the conditions or angles of deposition have a significant effect on the surface morphology.

All images in this section are taken at the same scale, where the full image size is $\sim$2 μm wide, 500 nm marked on each image.

All conditions at 45°

Figure 6.12 shows the 45° (sample 7 figure 6.2b) images for all conditions at low pressure (0.33 Pa). In this section, the images are separated by pressure, with the 0.33 Pa, low pressure, DC compared to the coherent and chaotic spokes in figure 6.12, and the 1.7 Pa, higher pressure DC, compared to the spokeless condition in figure 6.13.

It can be seen that all three low pressure samples show a similar morphology; of a dense film with no columnar structure; consistent with zone T. The grain size in all images is small and has an elongated faceted grain, rather then a columnar structure. The film in figure 6.12a, the DC condition, might appear to have a slightly larger grain than the two HiPIMS conditions, though this might be due to better focusing in figure 6.12a than b and c. Even if this were the case, the DC condition seems to show evidence of high energy ions, normally observed in HiPIMS.

Figure 6.13 shows both (a) the DC high pressure and (b) the spokeless conditions. The differences between figures 6.12 and 6.13 are very apparent. A much more columnar structure is immediately apparent in figure 6.13, indicating a far less dense film. The DC high pressure condition has grain sizes on the scale 500 nm, whereas the spokeless condition seems to have smaller columns, $\sim$100 nm, implying a denser structure; however this is hard to tell as only the top of the columns is visible. The smaller grains imply the spokeless film is denser, indicating some presence of high energy ions, but it still shows the same columns as in the DC case.

SEM images at different positions

Figure 6.14 shows all the low pressure conditions, for all position, sample 1 for all condition is in figure 6.14a-c, sample 7 for all condition is in figure 6.14d-f and sample 9 for all condition is in figure 6.14g to i.

It can be seen from figure 6.14 that there is strong uniformity between the samples regardless of position. It is possible that the side-on samples (sample 1 figure 6.14a-c) have slightly smaller grains; however this once again could be an effect of better focusing. It also seems that like figure 6.12, the DC film is slightly less dense with larger grains, than either

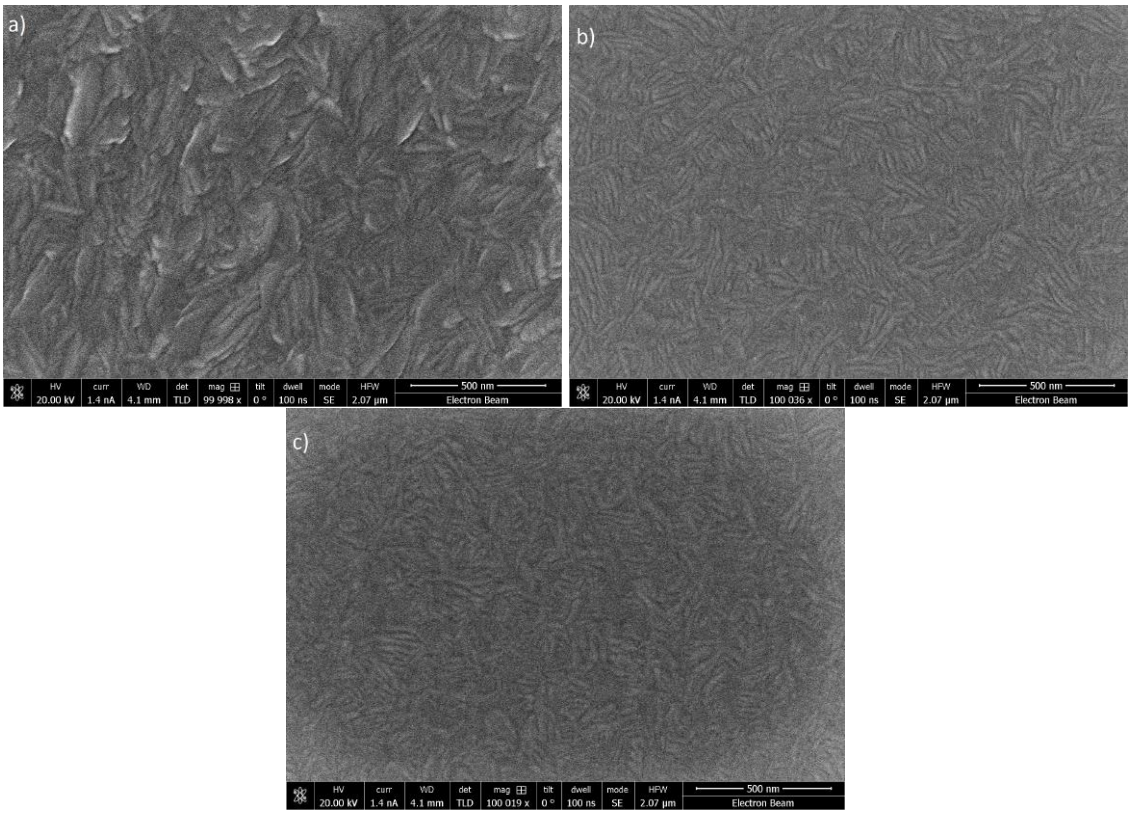

Fig. 6.12 SEM images for sample 7 made at 0.33 Pa at a) DC condition, b) chaotic condition and c) coherent condition.

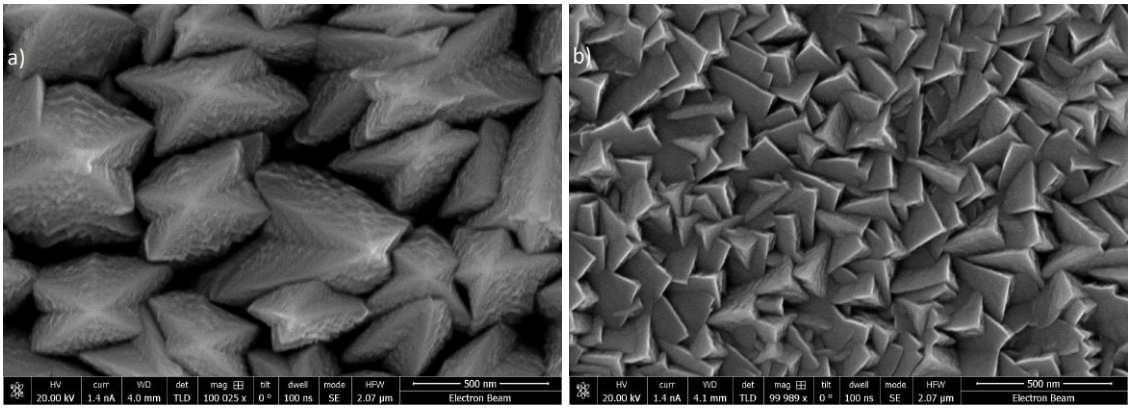

Fig. 6.13 SEM images taken directly facing the target for sample 7 made at 1.7 Pa at a) DC condition, b) spokeless condition.

of the HiPIMS conditions, though again this cannot be distinguished from focusing. The two HiPIMS conditions (at lower pressure) produce very similar, indistinguishable, films in terms of surface morphology.

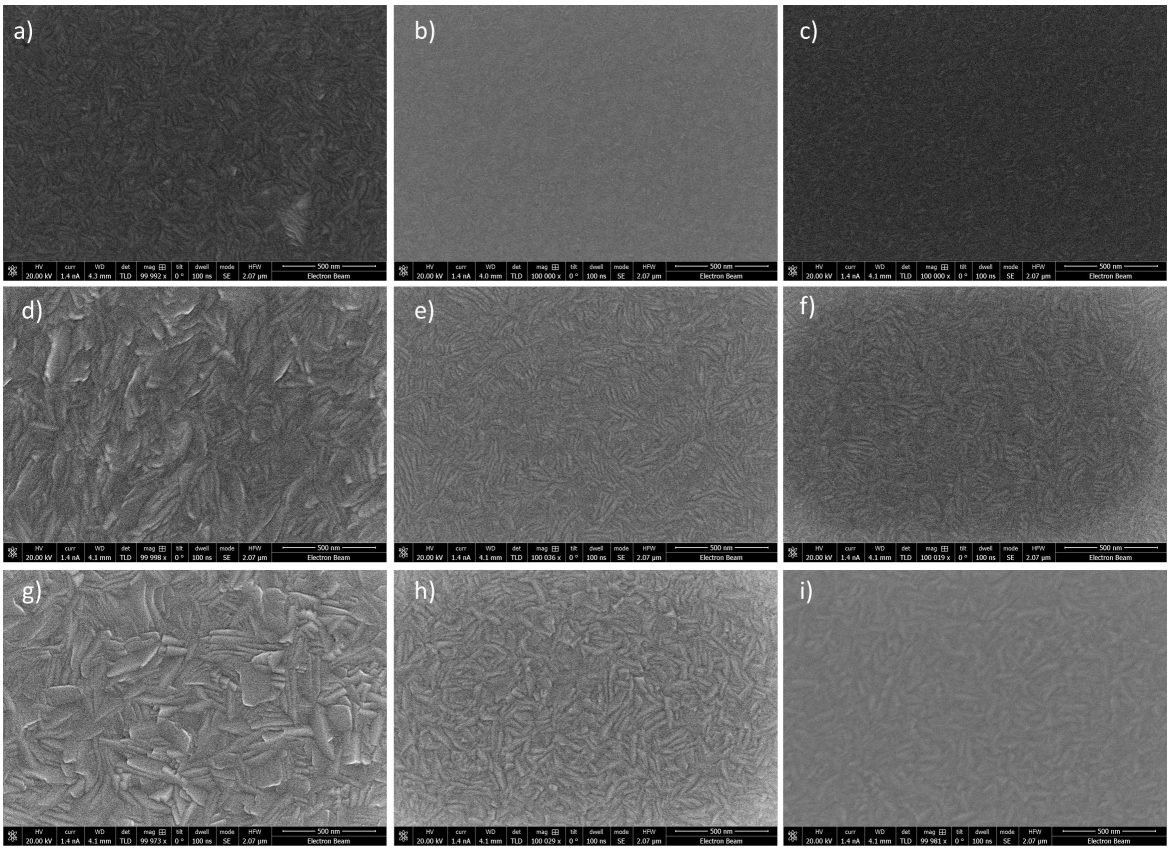

Fig. 6.14 SEM images taken directly facing the target for sample no. 1 of a) DC condition, b) chaotic condition, c) coherent condition, sample no. 7 of d) DC condition, e) chaotic condition, f)coherent condition and no. 9 of g) DC condition, h) chaotic condition, i)coherent condition.

The two higher pressure films are shown in figure 6.15 at all positions, sample 1 facing side-on (figure 6.15a and b), sample 7 at 45° to the target (figure 6.15c and d) and sample 9, facing the target directly (figure 6.15e and f).

The samples in figure 6.15 show a more apparent effect from position than figure 6.14. The side-on position (slide 1 figure 6.15a and b) shows the smallest visible columns film for both conditions. In the spokeless condition, 45° sample (sample 7 figure 6.15d) shows largest grain size. The DC 45° and directly facing (samples 7 and 9 figure 6.15c and e) have approximately the same grain size. The spokeless condition again shows consistently smaller grains, implying higher density, at all sample positions, compared to the DC condition.

Conclusions

The SEM images show that pressure has a greater effect on surface morphology than the discharge conditions or sample position; this can be seen from comparing figures 6.12 and

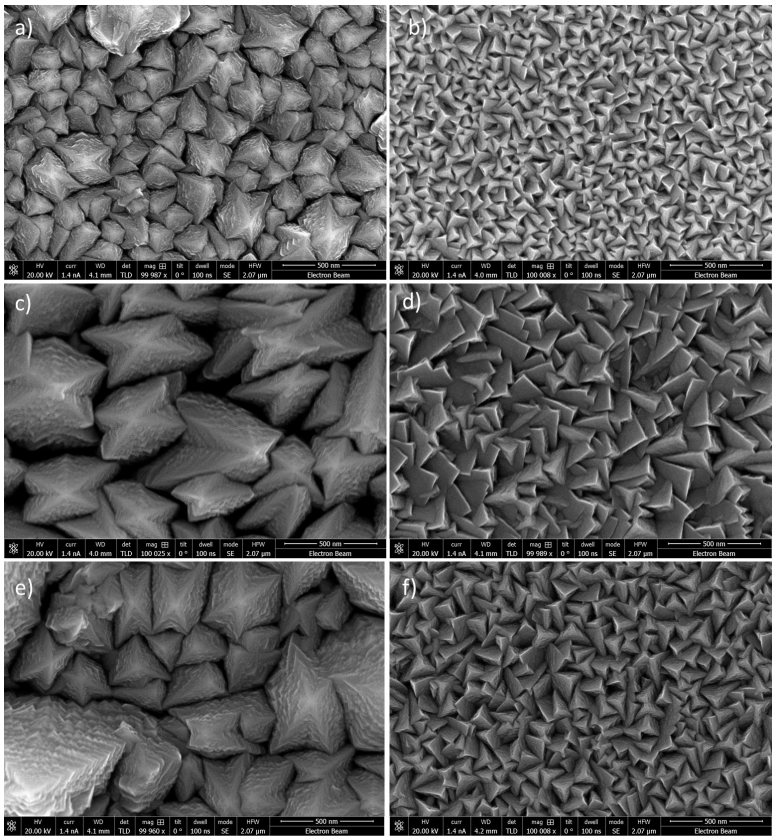

Fig. 6.15 SEM images taken directly facing the target for sample no. 1 of a) DC condition, b) spokeless condition, sample no. 7 of c) DC condition, d) spokeless condition and no. 9 of e) DC condition, f) spokeless condition.

6.13. The differences caused by pressure visible in the SEM images are so great that the high and low pressure HiPIMS conditions cannot be compared.

At lower pressures, all films, even in the DC condition, show no sign of columnar structure. The effect of the spokes or different spoke regimes cannot be identified based on the SEM images in figure 6.12. Similarly the effect of position does not have have a detectable impact on surface morphology.

However at higher pressures, the spokeless regime does lead to significantly denser films than the DC condition, although both show signs of columnar structures. Also there is a more definite effect of position, with the side-on deposition showing the smallest grain size in both the DC and spokeless regime.

Analysis by XRD

Introduction to XRD

In this section, the films are analysed by XRD; samples 7 and 9 are analysed for all conditions and sample 1 is analysed for the coherent condition only. The XRD measurements were taken on a Bruker D8 Discover at a glancing incidence of 2 degrees; the low angle is used because some of the films are relatively thin. XRD is used to measure the atomic spacing in the lattice structure, as the X-rays are refracted at angles relative to lattice spacing, as described by Bragg's law [125].

The lattice spacing measured in the samples are compared to their equivalent powdered reference results (ICDD 00-035-0789). Niobium has a simple cubic structure where the preferred grain orientation is (1 1 0). Only the preferred grain orientation is shown as being the most accurate measurement of lattice spacing; as the most prevalent orientation, it is therefore the most important result for characterising the general film. The angle of diffraction is measured to 5 significant figures, the results here are given to 4 significant figures.

Results and analysis of XRD

The results of the XRD are given in table 7.3 for the (1 1 0) orientation, which is the preferred grain orientation for all; under these conditions the reference lattice conditions is 3.3062 Å. The coherent directly facing result (sample 9), was not included as its XRD results indicated a niobium oxide, rather than a plain niobium film. This means that the coherent condition sample 9 cannot be compared to the remainder of the results in table 6.4 or figure 6.16.

Sample conditions	Side-on (Å)	45° (Å)	Directly facing (Å)
0.33 Pa DC	-	3.297	3.286
Chaotic conditions	-	3.332	3.317
Coherent conditions	3.330	3.331	-
1.7 Pa DC	-	3.320	3.319
Spokeless conditions	-	3.359	3.295

Table 6.4 The lattice spacing for the XRD analysed samples at side-on, 45° and directly facing under all conditions.

If the samples have a longer lattice spacing than the reference lattice spacing, it is a sign that the film is under compressive stress. Inversely, if the lattice spacing is shorter than the

reference spacing, then it is a sign of tensile stress. The results from table 6.4 are shown in figure 6.16

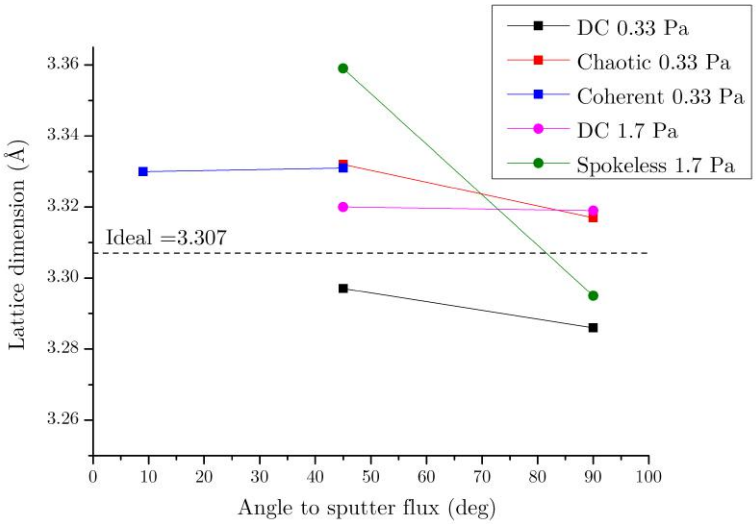

Fig. 6.16 Showing the lattice spacing of samples deposited under different conditions at different angles, with the powder lattice reference (ICDD 00-035-0789) marked.

Compressive stress has been suggested to be the result of ion bombardment inserting out-of-plane ions into the lattice structure, increasing sample density [52] [126] (by way of [127]).

All the HiPIMS samples show signs of this compressive stress, indicating that they have been subjected to ion bombardment. The DC case shows a more confusing picture with the DC at high pressure showing signs of compressive stress, but at low pressure showing tensile stress. The reverse would be expected from the SEM images and previous results [127] [52]. However these differences are all within $\sim$1 % of the ideal powder value, and hence do not reveal a significant effect; elsewhere values of $>$ 2 % have been shown under similar conditions [127].

In general there is little difference in lattice spacing at different angles for the same conditions. The only significant difference is in the spokeless case. This might be expected as the spokeless case shows the greatest if not the only difference in film morphology due to the angle of deposition.

6.5 Summary and conclusions

Summary

This experiment was conducted in two parts and the first part in section 3 looked at the regimes and amplitudes of spokes in an argon-niobium discharge. As expected, there were found to be three regimes of spokes: chaotic at lower power and pressure, spokeless at higher power and pressure and the coherent regime in-between.

It was discovered that there exists an optimum power at which spoke amplitude is at a maximum. When the power is increased from this maximum, the spoke amplitude decreases until the spokeless regime is reached (power supply permitting). The power required to access the spokeless regime is reduced at higher pressures.

The reason for this pattern was theorised to be connected to the regimes of spokes. At lower power and pressure, only chaotic low amplitude spokes are observed. As the power increases, the spokes become uniform and grow in size. However the maximum I_p of a spoke is limited, in such a way that I_p during a spoke cannot exceed the I_p during the spokeless condition. This leads to an optimum power for the high amplitude spokes' pattern. Pressure affects the power at which the discharge regimes change.

From section 4, a set of film samples at positions from side-on to directly facing the target were deposited. This was done under three discharge conditions representing the chaotic, coherent and spokeless conditions respectively; at pressure 0.33 Pa, E_p = 3.6 J (chaotic) and E_p = 6.8 J (coherent) and pressure 1.7 Pa, and E_p = 10 J (spokeless). In addition, two sets of DC films were deposited at 0.33 and 1.7 Pa, as a basis for comparison. All films were created at an average power of 250 W with a deposition time of 3 hours 30 minutes.

The deposition rate of all samples, in all positions, were investigated with respect to both power and average current. While the DC case always had the highest deposition rate, the spokeless condition was similar when normalised to current.

The deposition rate at different angles was also measured. It was found that the samples deposited at 45 $^\circ$ to the target had the highest deposition rate, except in the case of coherent spokes where the highest deposition rate was found for samples directly facing the target. The spokeless and coherent conditions both showed a higher proportion of deposit to the side than the DC cases, though pressure was the dominant factor.

SEM images were made to investigate surface morphology. It was found that pressure has a much larger effect on the films than the discharge conditions. At lower pressures (0.33 Pa), all the samples show a dense film with no sign of a columnar structure,indicating zone T

film growth. There was strong consistency between deposition at all conditions and positions at lower pressure. However the side-on position and two HiPIMS films may show slightly greater density, though this difference could be due to focusing in the images rather than the film properties.

The higher pressure conditions clearly showed the columnar structure for both the DC and spokeless case. However the spokeless condition produced a significantly denser film with smaller grains. Additionally both high pressure films showed a greater variation with respect to position, the 45° position being the least dense and the side-on one being the most dense, for both conditions. The effect of position was most obvious for the spokeless condition.

The films were analysed by XRD; from this the lattice spacing of the preferred grain orientation (1 1 0) in all spoke conditions showed signs of ion bombardment, though the low pressure DC case did not. The angle of deposition did not have a major effect, outside of the spokeless case. There was little effect from different spoke conditions, with the greatest differences in the results being due to pressure.

Conclusions

The results gathered in this study seem to indicate that spoke conditions do not have a major effect on surface morphology compared to other effects such as pressure. The results also showed that the angle of deposition does not have a major effect on the surface morphology, at least at low pressures. However the spoke conditions and angle of deposition do affect the deposition rate.

These results give an indication of the effect of spoke conditions on film formation. While it clearly shows that pressure has a greater effect than the spoke regimes, one piece of research missing from this study is the comparison of the spokeless to other spoke regimes at the same pressure. Future studies should take care that deposition in the chaotic, coherent and spokeless regimes are all performed at the same pressure. The power supply used in this study could not reach the spokeless regime at low pressures, meaning further studies would require either a power supply able to supply a higher output power, or the coherent condition at higher pressure where spokes have a lower amplitude.

Chapter 7

Triple probe in a HiPIMS discharge

7.1 Introduction

In the 1990s, high power impulse magnetron sputtering (HiPIMS) was developed as a way to increase the ionisation rate of the sputtered particles used for ionised PVD (IPVD) [24] [128]. This was achieved by increasing the power during the magnetron on-time up to 10 kW m^{-2}. However, the target would be damaged by arcs or overheat/melt if left at such high powers for long time periods [10] so, in order to avoid this, the magnetron is pulsed with a low duty cycle [14] and on-times of around 100 μs. This high ionisation rate causes several effects during the HiPIMS pulse that are not seen in lower power pulsed DC depositions. The high levels of power that generates these high rates of ionisation also cause rarefaction [63] [56] because the high deposition rate causes an increase of pressure and heat above the target. This leads the background gas to be pushed out of the target region [129].

Additionally, the high rate of ionisation of sputtered flux can lead to self-sputtering [78] where neutrals, sputtered from the target, are ionised and re-attracted to the target, hence sputtering it. This self-sputtering has the effect of reducing the deposition rate [120]. However at higher powers this can also result in runaway self-sputtering. This is where self-sputtering creates more sputtered particles than are returned to the target, causing the discharge current to grow exponentially [63].

All of these result in a distinctive HiPIMS pulse evolution. Pulse time evolutions have been studied in depth by Langmuir probes [130] [33], emissive probes [131], the target current-voltage (IV) trace [17] and computer modelling [57]. The basic HiPIMS pulse evolution is:

- When the target is first switched on, it has a high negative potential which induces a highly negative plasma [132]. High energy electrons [33] have been observed at this time.
- Soon after, there is a large increase in the discharge current and plasma density because the high energy electrons become trapped in the ExB drift/Hall currents, leading to high ionisation.
- This large increase in current and ionisation leads to a sputter-wind causing a high degree of rarefactions which vacates the target area of neutrals [57]. Due to the lack of neutrals, the target current decreases to a maintainable lower power for the remainder of the discharge.

Or.

- The background gas neutrals are replaced by sputtered target neutrals, so the discharge current is either maintained or enters runaway self-sputtering [56].

A newly discovered aspect of the HiPIMS discharge is the phenomenon of high ionisation zones rotating in the ExB direction on the target, known as spokes [81]. As spokes have been linked to the production of high energy ions [29] [28] in HiPIMS, their study has been the focus of many investigations. The majority of these have used fast imaging [85], often combined with another method, such as mass spectrometry with high time resolution [23] [104], monitoring of the discharge current-voltage [36], and electrical probes [86] [38] [97]. Embedded current target probes have also been used instead of ICCD imaging by Poolcharuans et al [90].

From these readings, spokes have been theorised to have regions of runaway ionisation [85] [31] whereby an increase in density makes further ionisation more likely [84]. This leads to high rates of ionisation, which in turn leads to high rates of local rarefaction [87], reducing the neutral availability. As the ionisation rate increases, the spokes become positively charged and surrounded by a double or triple layer [102] [89]. The spoke eventually completely runs out of neutrals available to ionise and therefore terminates. [87]. Thus, the rotation of spokes is less the motion of high density plasma and more a phase velocity as described above [84]. Plasma or electron flares have also been seen above the spokes, indicating that they have some kind of associated heating mechanism [31]. This mechanism could either be high energy secondary electrons from the target, electrons accelerated through the pre-sheath or even electrons accelerated though the positive potential of the spokes themselves [100].

As well as considering spokes in their own right, the conditions under which spokes form and the amplitude and regimes of the spokes are also of interest. Work by Poolcharuans et al

[90] and Breilmann et al [23] found three distinct regions of spokes at different discharge conditions. At lower power and pressure, spokes were chaotic and lower amplitude in nature, but as the power and pressure increased the spokes became regular and periodic. However if the power and pressure were increased sufficiently, the spokes disappeared. This is discussed in greater detail in the literature review, chapter 2.

While the above techniques used in conjunction with computer modelling have provided a good insight into spokes, there have been no un-averaged, time-resolved plasma measurement for spokes inside the magnetic trap. In this chapter, we therefore use a triple probe to investigate the HiPIMS discharge inside the magnetic trap. The triple probe, originally proposed by Chen et al [110], can take readings on n_e and T_e with sufficient time resolution to investigate spokes.Triple probes are commonly used on systems that cannot employ normal Langmuir systems. This is because they require data which have not been time-averaged, such as tokamak reactors [133] [111], Columbia linear machine such as PANTA [134] and streaming plasma [123].

Triple probes have been used in pulsed DC [135], modulated pulsed power [136] and HiPIMS [137]. However these studies all gave time-averaged results; in no study has a triple probe been used to investigate spokes or the discharge conditions at which spokes occur. In this chapter, we will use a triple probe to investigate the HiPIMS discharge in relation to the conditions at which spokes occur, as well as to look specifically at spokes.

This section has contained a brief introduction to the HiPIMS discharge, spokes and the triple probe. Section two will discuss the design and testing of the triple probe. Section three will detail the experimental setup for the completed triple probe design. Sections 4 and 5 contain the results; section 4 will detail the use of the triple probe to investigate the whole HiPIMS pulse while section 5 will investigate the spokes only. Conclusions are presented in section 6.

7.2 Preliminary experiments and testing

The triple probe used in this section was built and tested in-house. This section details that building and testing. While triple probe theory has been long established and is outlined in chapter 4, there is no established standard equipment or circuitry in the way that there is for Langmuir probes. In order for the triple probe to be used, one must find an appropriate battery potential for operating conditions; choose the best triple probe mode (either voltage mode or current mode); test the readings taken by the triple probe against more established techniques (such as a Langmuir probe); and design and test a triple probe circuit.

Finding suitable battery biases

The initial experiments were intended to select suitable values for the battery bias for the triple probe in the voltage mode (in current mode, any battery bias can be chosen). This has to be done first because one needs to know the approximate voltage and currents expected in the circuit, before it can be designed.

In order for the results to be valid, the value of V_{31}, the battery bias, in voltage mode is subject to the condition $V_{31} >> T_e$ (in electron volts). To meet this condition, V_{31} must be such that the negatively biased probe draws the ion saturation current I_{isat}. However if V_{31} is too large, it will result in sheath expansion giving a falsely high value of I_{isat}, which means that the calculated value n_e will also be falsely high. However values of T_e will be almost entirely unaffected. This error is discussed further in chapter 4.

It would be expected that as the V_{13} rises from zero to an arbitrarily high value, the measured value of I_{isat} would initially increase rapidly, as the increase in voltage moves through the transition region, slowing as it begins to draw close to the true I_{iast}. Furthermore it is expected that, even once I_{isat} is drawn, an increase in V_{31} will still cause an increase in our measured value of I_{31}, through sheath expansion in the I_{isat} region.

To find an appropriate value of V_{31} ,a battery pack with a variable output voltage was used in a triple probe circuit, as shown in figure 7.1. The triple probe was placed in the bulk plasma then placed 50 mm in front of the centre of the magnetron also shown in figure 7.1. The voltages are measured at points indicated on figure 7.1 and recorded by three Tektronix TPP 0201 voltage probes on a Tektronix DPO 3034 oscilloscope, averaged over 124 pulses. Resistor R is of value 10 kΩ

The battery bias was increased from 2 to 59 V in steps of ∼5 V; for a 100 μs pulse at 1.2 Pa pressure, a 50 Hz power supply with no pre-ioniser was used. The battery pack output voltage was dictated by a set of batteries with a potentiometer circuit and did not give finite changes in output bias. The readings were averaged over 124 pulses.

I_{isat} is calculated using using Ohms law across the resistor R, with results being shown in figure 7.2.

As can be seen from figure 7.2, increasing the battery bias between 3 and 15 V causes a noticeable increase in the measured value of I_{isat}. However, after that point, the increases become more gradual in the range 23 - 43 V, and subsequently the increase becomes almost non-existent for $V_{31} > 43$ V.

Rather then an exact value for V_{31}, figure 7.2 gives a range of values suitable for V_{31} of 23 - 43 V. As can be seen from figure 7.2, the errors due to having V_{31} that are too low are

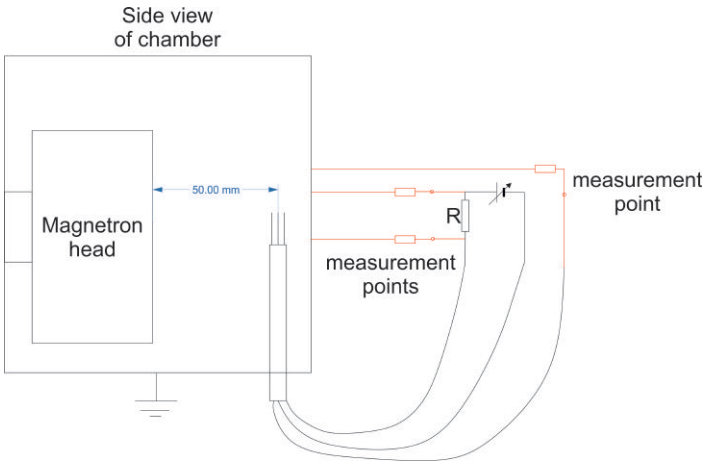

Fig. 7.1 The triple probe setup used to find an appropriate value of V_{31} using a variable battery pack with measure points indicated; resistor R is of value 10 kΩ. Also showing the triple probe alignment and position relative to the magnetron.

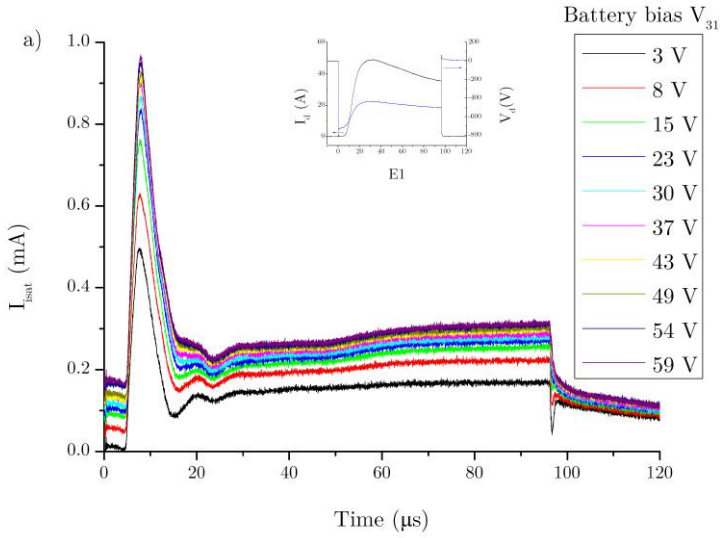

Fig. 7.2 The values of I_{isat} in the bulk plasma calculated by Ohms law across a 10 kΩ resistor for a 100 μs averaged over 124 pulses is used to find an appropriate value of V_{31}. A discharge I-V is included.

worse than for those where V_{31} is too high (as has been explained more fully in chapter 4). Therefore values of 30 V $< V_{31} <$ 40 V are chosen for the remaining experiments.

Current mode against voltage mode

The triple probe was tested in both DC and HiPIMS discharge, using both current and voltage modes. While both modes gave reasonable results, given their early stage of development, only the voltage mode was developed further in our experiments.

This choice was made because of the available means of measuring the current. In current mode, a Tektronix TCP 0030 and Pearson 2277, both wound ten times, are required to record in the range of 0.1 to 10 mA, although their finest resolution is at $\sim$ 0.1 mA. In contrast, the probes required for voltage mode, a set of Tektronix TPP 0201 probes, are far more accurate in the required range -20 to +5 V with an error of around 1 mV.

Testing the triple probe against the Langmuir probe

To establish confidence in the triple probe, the results taken by the triple probe should be compared to results taken under the same conditions by other, more established methods. The Langmuir probe can be used to take readings of the same values as the tripe probe so it is the obvious choice to make such comparisons. If results obtained using the triple probe method match those obtained using the Langmuir probe, within error, under the same conditions, this would validate future triple probe results. As discussed in chapter 4, the many factors affecting the Langmuir probe are covered by a standard error of $\pm$ 20%. Additionally, the triple probe takes readings for a single pulse and the Langmuir probe requires averaging over thousands of pulses, which requires the power supply to be continuously running for $\sim$ 30 minutes.

Even under the same conditions, the values obtained by the triple probe change over repeat readings. This is not necessarily due to an error in the readings but may occur because no two HiPIMS pulses are exactly the same. By comparing repeated triple probe readings taken under the same conditions, an error of $\pm$ 10 % is found.

If the results from the triple probe and the Langmuir probe are within error of one another and more importantly have matching general trends over changing conditions, this will give us confidence in future triple probe results. For this test, the triple probe and the single Langmuir probe were positioned in the null point of the magnetic field (30 mm from the centre of the target). The null point is chosen as it will be free from the influence of magnetic fields. Power supply B was used with a pre-ioniser to supply a range of power for a 100 μs long pulse with a repetition rate of 50 Hz.

The triple probe circuit used was of an older design. All probes have the same root to the ground (there is a unified ground with the chamber wall), shown in figure 7.3, where R_1 = 3.3 MΩ, R_2 = 330 kΩ, R_3 = 1 MΩ, R_4 = 100 kΩ and R_5 = 2 kΩ with Tektronix TPP

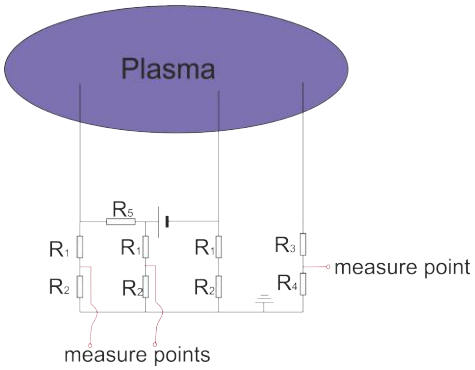

Fig. 7.3 The triple probe circuit tested against the Langmuir probe system, with a fixed battery bias of 34 V where R_1 = 3.3 MΩ, R_2 = 330 kΩ, R_3 = 1 MΩ, R_4 = 100 kΩ and R_5 = 2 kΩ.

0201 voltage probes attached to each measure point connected to a Tektronix DPO 3034 oscilloscope. Voltage traces are measured at all points shown on figure 7.3 and from these, values of T_e are then calculated.

The Langmuir probe tip was of the same dimensions as the triple probe (0.08 mm diameter, 5 mm long). The Langmuir probe capture system was an ALP system operated in time resolve mode with a time resolution of 40μs, producing 3 Langmuir I-V characteristics between 0 and 120 μs after the pulse. T_e is calculated using the methods described in chapter 4.

The operating conditions are varied, with pressures of 0.33 and 1 Pa and pulse discharge energy E_p of 0.2, 3.8 and 5.6 J, (these values were chosen based on their peak currents). This allows us to analyse the trends as well as the measured values themselves.

Of the three time ranges measured, the 40-80 μs range gave the clearest results, so the values of T_e recorded over this time range were compared to values of T_e from the triple probe averaged between 40-80 μs.

It would be expected that, as the power and pressure of the discharge increases, T_e would decrease. This is exactly the trend seen in figure 7.4 for the readings measured by both the triple probe and Langmuir probe.

Although the trends seen in figure 7.4 are as expected for both the triple probe and the Langmuir probe, we note that the absolute values are not exactly the same in each case. However, they are always within error of one another. This is strong evidence confirming the triple probe results.

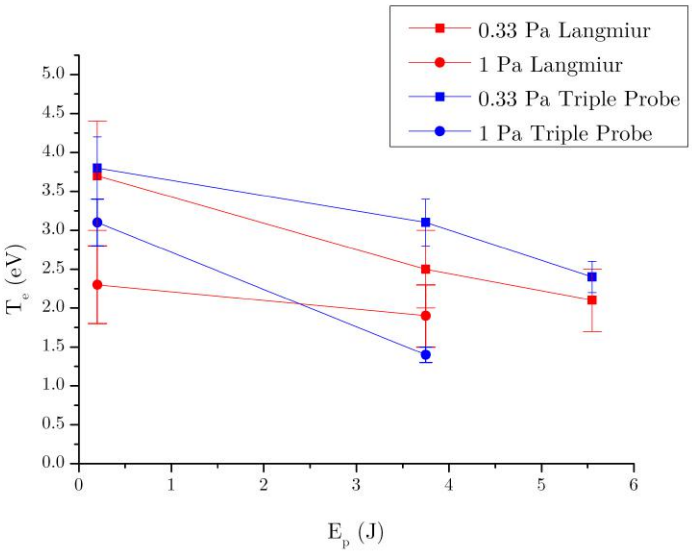

3

Fig. 7.4 Measurements of T_e obtained using both the triple probe and Langmuir probe, taken at the null point of the plasma in the time range 40-80 μs at a set of pressures and powers.

The triple probe circuit

The triple probe circuit used in figure 7.3 was designed with the intention that all probes should have the same resistance to ground. While ideally the probe circuit would be floating (no connection to ground), the use of voltage probes introduced an unavoidable source of grounding. As differences in value are most important in the triple probe circuit, it is argued that introducing a unified route to ground of $\sim$1.1 MΩ is less disruptive than a unknown uneven route to ground at some points but not others.

However, testing of the circuits such as those in figure 7.3 revealed un-physical oscillations at the start and end of the pulse. This is believed to be due to the interaction of the stray resistance and capacitance to ground. The reason we think this is that, when we use a simple circuit with no resistors to ground except for the ones in the probes themselves, the un-physical oscillation disappeared or were greatly reduced. In this simple circuit, the current was measured directly by a Tektronix TCP 0030 current monitor (wound ten times) and the voltage probes were connected directly to the probes.

The oscillations produced by the grounding circuit shown in figure 7.3 do not affect the results beyond the first $\sim$30 μs, meaning that results taken with the grounding circuit in figure 7.4 also apply to the simple circuit.

Conclusions

From the experiments reported in this section, a simple voltage mode triple probe circuit where the voltage is measured directly and the current is found by a ten times wound current monitor has been designed.

The selection of voltage mode operation for this experiment was based mainly on the practicality of measuring voltage over current.

In the voltage mode, a battery bias of 30-40 V was found to give the ion saturation current with minimum sheath expansion, as can be seen in figure 7.2.

The triple probe was tested in the null point of the plasma against the single Langmuir probe under the same conditions. The results from the triple probe and Langmuir probe were found to match within error and showed the same general trends.

Various triple probe circuits were tested, and it was found that more complex circuits produced an un-physical oscillation at the start of the pulse. As a result, a simple circuit was selected.

Taken together, these experiments provide a strong basis to design a triple probe experiment capable of obtaining valid results.

7.3 Experimental setup

On the basis of the preliminary experiments described above, this experiment and the triple probe was designed. The triple probe has probe tips which are made from tungsten wire 5 mm long and 0.08 mm in diameter, separated by $\sim$1 mm. The probes are insulated by ceramics leaving gaps no bigger then 0.01 mm. The triple probe circuit is shown in figure 7.5, with the resistance (10 MΩ) of the voltage probe included.

The main rig, system one, is used in the experiment with argon backing gas and a pair of targets, both niobium 99.95 % purity. One target was unaltered, the other had three 2.14 mm slots cut, to be filled by three 2 mm niobium strip probes; the same dimensions as the strips covered on three sides with polyimide tape of thickness of 0.07 $\pm$ 0.01 mm. A basic schematic of this rig with the strip probes and triple probe position is shown in figure 7.6a. The strip probes are width 2 mm and separated by an angle $\theta = 25^\circ$ separation, shown in figure 7.6b. The strip probes draw current from the same power supply as the target meaning that they are at the same potential. However, the strip probe current can be measured separately by a set Pearson 2277 current monitor.

Power supply B was used to deliver a 200 μs pulse with a repetition rate of 1-2 Hz, and to maintain this low frequency a simmer source is used. The power was recorded differently

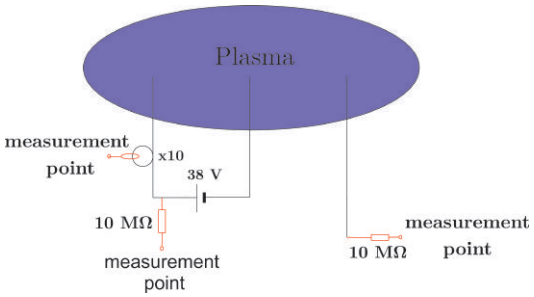

Fig. 7.5 The simplified triple probe circuit, with measure points shown.

depending on whether the slotted or unaltered target is used.

When the unaltered target is used, a Tektronix DPO 3034 oscilloscope is used to measure the target discharge current I_d, voltage V_d. The triple probe voltage and current traces are also recorded on the oscilloscope, which required three of the four channels, leaving only on channel permanently free (used to record I_p). To get around this, one oscilloscope channel was switched between recording I_{isat} and V_d on separate pulses, shown in figure 7.6c.

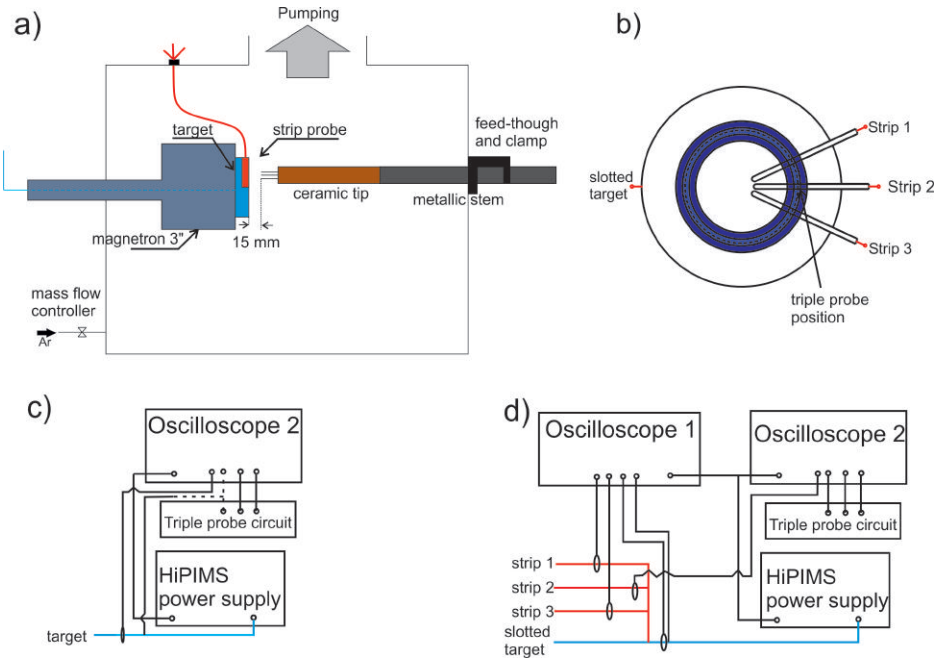

Fig. 7.6 Schematic diagrams of a) the magnetron chamber, with triple probe inserted, b) the strip probe and slotted target, c) the triple connection only and d) the triple probe and strip probe connection.

When the strip probes and slotted target are employed, a Tektronix DPO 4034 oscilloscope is used to measure I_d and V_d and the strip probe current of strips I_{p1} and I_{p3}. The Tektronix

DPO 3034 oscilloscope was used to measure I_{p2} and all three triple probe values, shown in figure 7.6d.

The simmer-source plasma, analysed by a single Langmuir probe, has $n_e \sim 10^{14-15}\ m^{-3}$ and $T_e \sim 10$ eV; under these conditions, the sheaths from the probe tips are likely to overlap and this results in a falsely high reading of T_e (under these condition I_{isat} is too low to be measured by current probes). T_e must therefore go through a transition from the falsely high values to the true values of T_e. Research by Poolcharuansin et al [33] found very high electron temperatures during the early part of the pulse. For $T_e \geq 10$ eV our assumption for $V_{31} >> T_e$ is invalid. For this reason the initial high T_e readings where $T_e \geq 10$ eV are not investigated.

The triple probe is placed directly over racetrack facing the target with the probes all aligned along in the radial direction in such a way that they all lie on one magnetic field line. When the slotted target is used, the triple probe is placed above the middle spoke (strip probe 2 figure 7.6b). The triple probe is positioned inside the magnetic field as shown in figure 7.7.

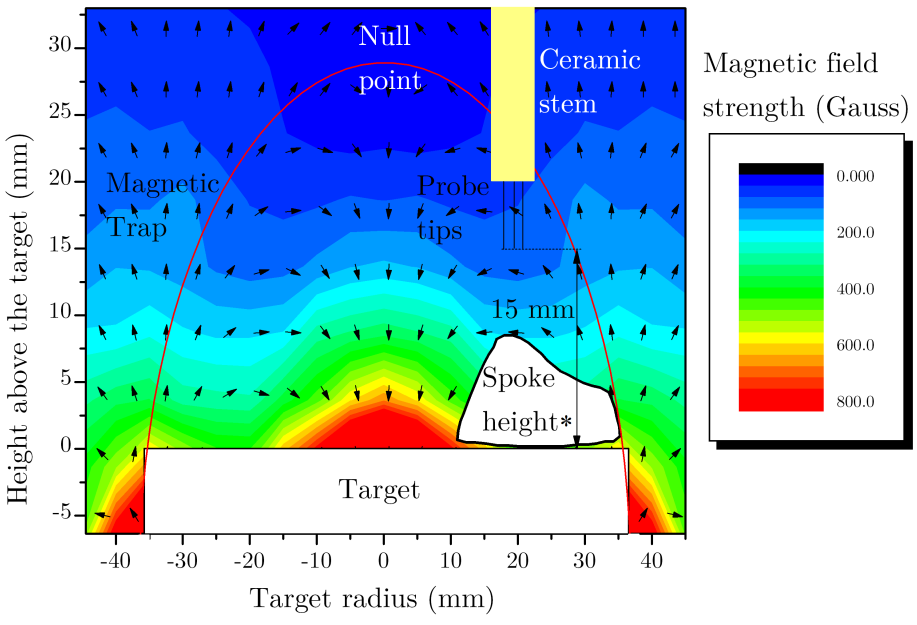

Fig. 7.7 The position of the triple probe inside the magnetic field trap. All three probes are aligned along a single magnetic field line. The 5 mm probe tips are 15 mm from the target surface. The boundary of the magnetic trap is shown in red, as is the target, the approximate spoke height is also shown. *Approximate spoke height as derived from [1]

From [136] [33] [24] we can predict at this position plasma densities $n_e \leq 10^{19}\ m^{-3}$ and $T_e \leq 10$ eV which would give $\lambda_D < 0.01$ mm. For this value of λ_D, our probe separation is sufficient in the sense that the probe sheaths do not overlap, and plasma cannot penetrate the gaps in the ceramic.

At these conditions, the plasma response time, T_p, which is the effective time resolution of the triple probe given by $T_p = \omega_p^{-1} \sim 1$ ns is easily sufficient to measure spokes, $\sim 1\ \mu$s. However in our experiment, the time resolution was limited by the oscilloscope, which collected 10,000 points over a time range of 400 μs. However, where appropriate, the results were smoothed to remove excess noise; smoothing was only employed when it did not affect the results, unless otherwise stated.

7.4 Results and analysis from a plain niobium target

Single pulse

Measurements of T_e, n_e, V_f and V_p were made for a typical pulse at pressure 1 Pa and E_P = 6.8 J with a plain Niobium target, 15 mm above the target as shown in figure 7.8.

Oscillation can be observed beginning around 75 μs into the pulse. Given the position of the probe, the target conditions and the frequency of these oscillations, this can be attributed to the effects of spokes. Oscillations are seen in all measured values appearing at the same time. The triple probe will be used to analyse spokes further in later sections.

There is an initially high peak in T_e, which falls quickly at the start of the pulse, n_e then rapidly increases to a peak at $\sim$30 μs, after which it gradually drops. Inversely, T_e reaches a minimum of $\sim$2 eV at $\sim$30 μs. T_e then increases gradually, plateauing between 80-120 μs just below 3 eV. This plateau is strongly correlated with the onset of spokes. n_e follows inversely to T_e and decreases from its initial peak; however the decrease in n_e is far more rapid, and the plateau at $\sim$120 μs $n_e \sim 2\times10^{19}\ m^{-3}$ is more sudden.

The peak in n_e corresponds to the maximum discharge current (I_d), seen in figure 7.9, as does the plateau region seen $\sim$120 μs. However I_d has a plateau between 30-75 μs during which time n_e has a rapid drop.

There are two possible explanations for this. The first is that this fall is an un-physical phenomenon. The calculation of n_e is based on I_{isat} and T_e, with factors for probe area, ion charge and ion mass. In the calculation on n_e for figure 7.8, the ion mass is assumed to be Ar^+. The composition of the plasma just above the target, however, is expected to change through the pulse from argon (Ar) dominated at the start of the pulse to be dominated by

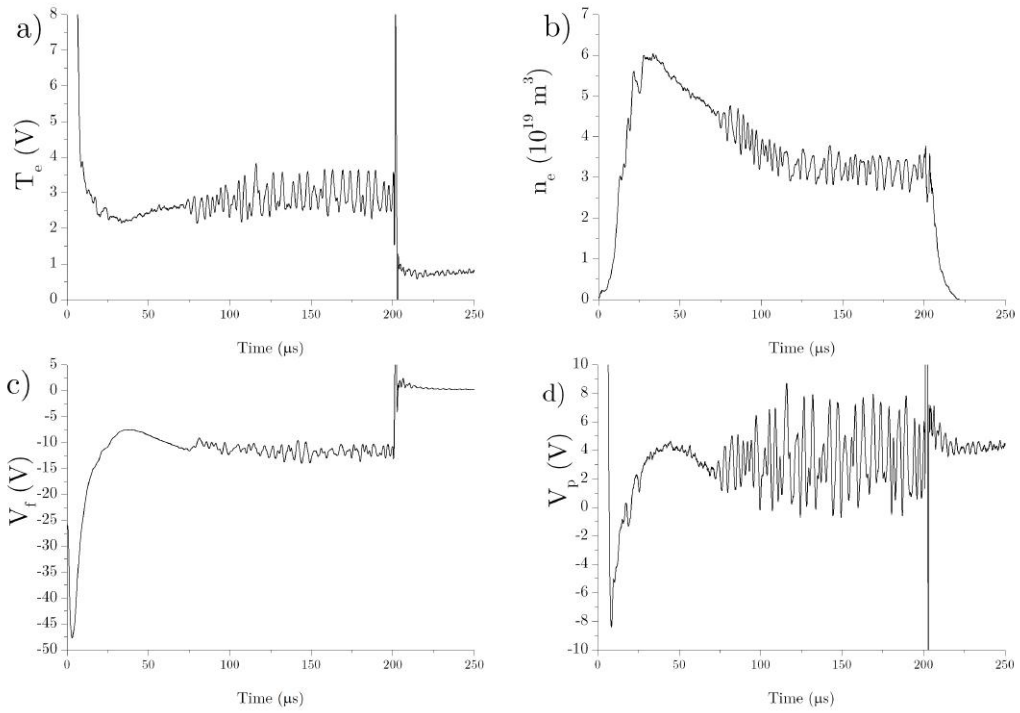

Fig. 7.8 In a)T_e, b)n_e, c)V_f and d)V_p measured by a triple probe 15 mm above the racetrack for a 200 μs E_p = 6.8 J and 1 Pa pressure.

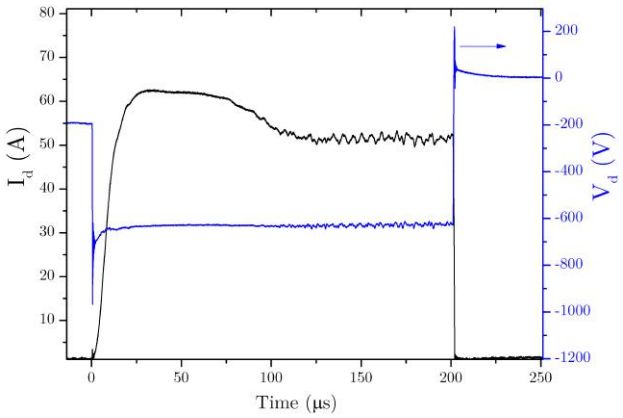

Fig. 7.9 The current (I_d) voltage (V_d) discharge profile for the E_p = 6.8 J 1 Pa pulse shown in figure 7.8.

sputtered metal (Nb) later, followed by a final Ar refill [67]. In figure 7.10 $I_d$is co-plotted with n_e calculated for both an Ar and Nb plasma.

The second explanation is that the peak in n_e is higher due to the high I_d causing rarefaction, thus reducing n_e near the target and forcing ions into the triple probe region. As the discharge progresses, this refraction decreases as the gas refills, causing the decrease in n_e.

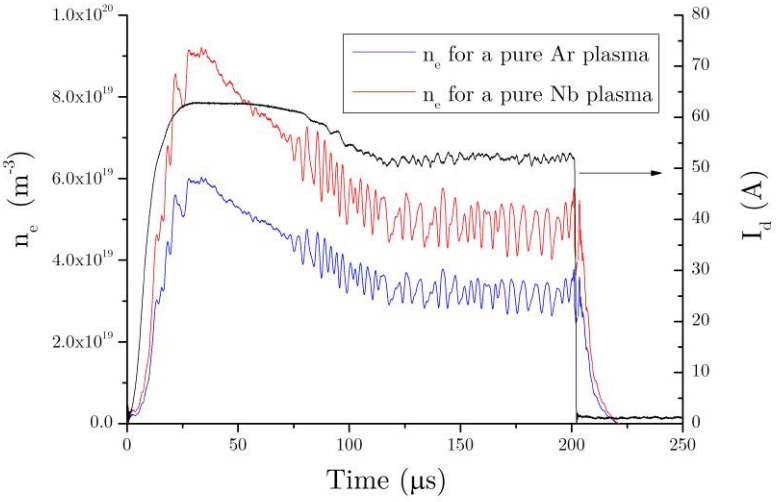

Fig. 7.10 The current (I_d) co-plotted with measured 15 mm above the racetrack n_e calculated for both an argon and niobium dominated plasma for a 200 μs E_p = 6.8 J 1 Pa pulse.

It can be seen from figure 7.10 that even a small change in plasma composition could be responsible for the apparent decrease in n_e between 30-70 μs.

The floating and plasma potentials act as expected based on previous studies; both are initially very negative, but level out as the current reaches a peak. The plasma potential is calculated from equation 7.1,

$$V_p = V_f - \alpha_1 T_e \tag{7.1}$$

Where α is 5.2 for an Ar plasma (5.5 from an Nb plasma). Based on these inputs with V_f $\sim$ -12 V and $T_e \sim$ 3 eV seen in figure 7.8, we get $V_p \sim$ +3 V. It should be noted that V_p starts as a high positive value because of the physical high initial T_e. This may also be why V_p does not reach the extreme negative values expected.

Positive values inside spokes has been predicted [29]. However the V_p values as seen in figure 7.8 are always positive, which has not been predicted. V_p in HiPIMS has been investigated using an emissive probe [131] [60] where the time average V_p has been measured at the position of the triple probe in figure 7.7 and found to be negative.

As a calculated value, if V_p is incorrect then this must be due to either the measured T_e or V_f also being incorrect. While T_e is in line with expected values [33] [32] [138], the measured value of V_f is higher than has been observed, [82]. Therefore it is appropriate to confirm our value of V_f. This is done by using a simple unbiased single wire (the dimensions are the same as for the probe used by the Langmuir system) which is positioned in the plasma at the same point as the triple probe, with the V_f measured by a Tektronix TPP 0201 voltage probe.

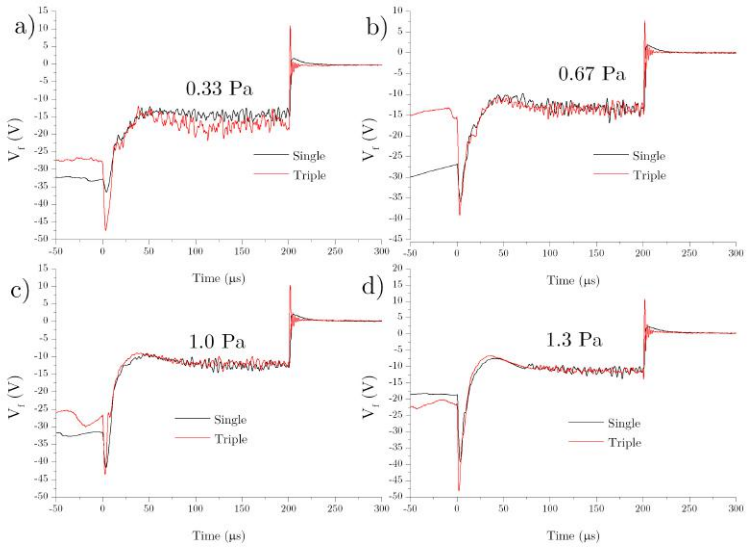

Fig. 7.11 The floating potential measured 15 mm above the target racetrack by a triple probe and a single probe co-plotted for a 200 μs E_p = 6.4 J at a) 0.33 Pa b) 0.67 Pa c) 1 Pa and d) 1.3 Pa

Figure 7.11 shows that the values of V_f measured by the triple probe are not significantly distorted compared to values measured by a simple single probe. This confirms the measured values of V_f and therefore the calculated values of V_p.

Electron temperature

In this section, the evolution and values of T_e measured at different discharge conditions are compared. T_e is shown in figure 7.12 for a set of E_p at 1 Pa and a set of pressures E_p = 8.4 J in figure 7.13, the corresponding I_d traces are shown in figures 7.12c and 7.13c.

As can be seen in figure 7.12a, the oscillations (thought to be due to spokes), make the trends in T_e hard to determine. To counteract this, figure 7.12b shows the same data as in

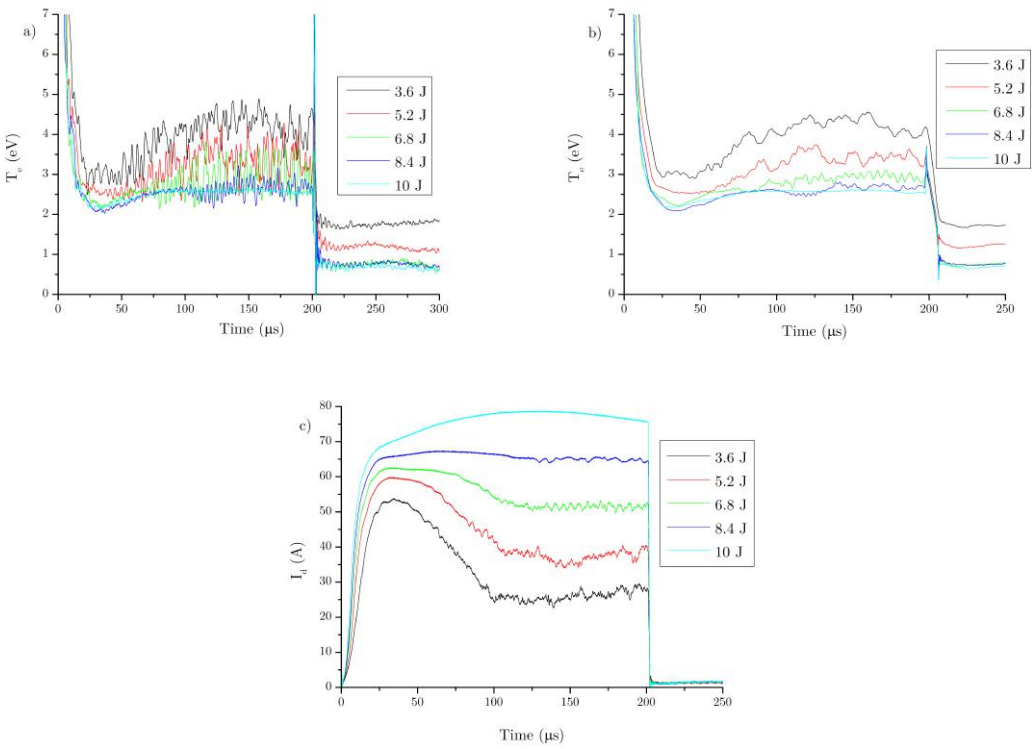

Fig. 7.12 T_e measured by triple probe 15 mm above the target racetrack for a set of 1 Pa pulses ranging in power from E_p = 3.6-10 J for a) a single pulse, b) featuring heavy smoothing and c) the discharge currents.

figure 7.12a, smoothed over 201 points (8 μs) by an adjacent average function. While figure 7.12b still does show traces of the oscillation, they do not obscure the data in the way that they do in figure 7.12a. Additionally the I_d for all conditions is shown in figure 7.12c.

Figure 7.12a and b show the electron temperature at 1 Pa over a range of pulse powers from 3.6-10 J in steps of 1.6 J. The same general trend in T_e is seen at all powers; an initial high peak, followed by minimum ~25 μs, which corresponds to the peak I_d. From there T_e gradually rises, eventually reaching a plateau, except in the case of E_p = 3.6 J which never plateaus. It is during the post-minimum rise that spokes are first observed. It can be seen from figure 7.12 that the power has a significant effect on T_e throughout the pulse. The lower is E_p, the higher T_e at all points; however as E_P increases, this effect becomes less pronounced, reaching the point where T_e for E_p = 8.4 J and 10 J have almost the same T_e . Another effect of power is on the time at which spokes appear. From figure 7.12a, it can be seen that at lower E_p, spokes appear earlier in the pulse. Additionally at lower powers, the plateau in T_e occurs later in the pulse, to the point at which T_e doesn't plateau at E_p = 3.6

J. It would be expected that pulses with higher I_d will have higher plasma densities, which would be explain why T_e is lower at higher I_d and E_p.

Figure 7.13a and b shows the T_e for a set of pressures at E_p = 8.4 J per pulse in figure 7.13b, T_e like in figure 7.12b has been smoothed by a 201 points (8 μs) adjacent average, to allow us to observe the data clearly without the effect of spoke perturbation. As expected at higher pressure, T_e is lowered as there is a higher neutral and ion density, and therefore more collisions, lowering T_e. The initial peak in T_e, is also wider at lower pressures. This effect is borne out on the current profiles in figure 7.13c as the lower the pressure, the longer it takes for the I_d to reach its peak. This slower I_d rise is likely due to the reduced availability of neutrals resulting in slower ionisation.

A common effect seen in both figures 7.12 and 7.13 is that at both lower powers and lower pressures, the spokes can be seen starting at earlier times. This indicates that T_e is a significant factor in spokes formation because spokes are mostly absent when $T_e < 2.5$ eV and have mostly formed and are present at $T_e > 3$ eV, with a transition region at 3 eV $< T_e <$ 2.5 eV.

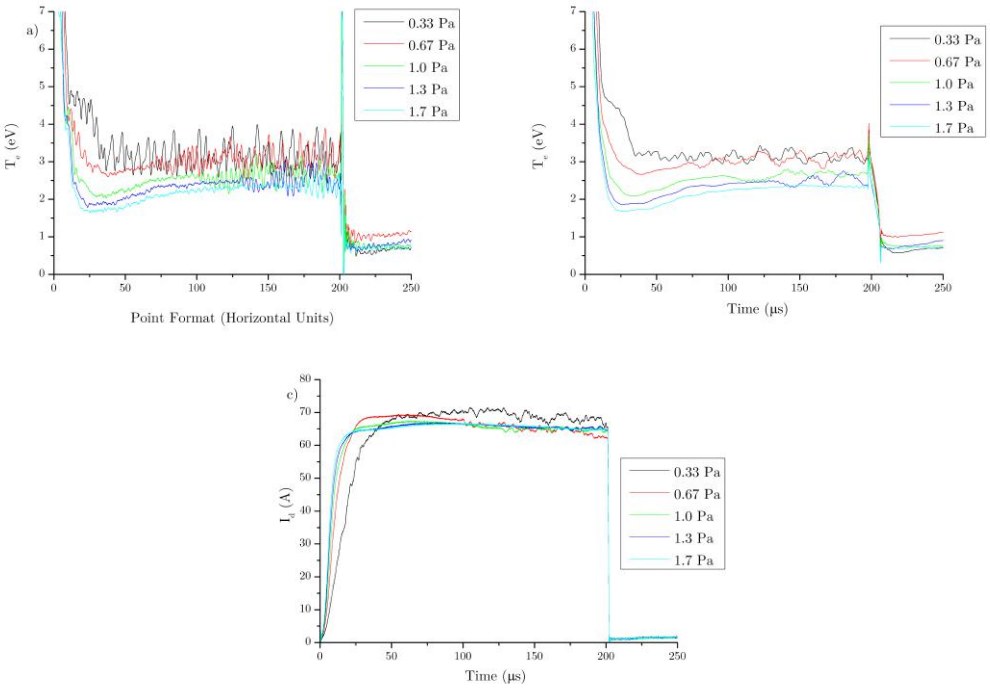

Fig. 7.13 T_e measured by tripe probe 15 mm above the target racetrack for a set of pulses ranging in pressure from 0.33 to 1.7 Pa for E_p = 8.4 J, showing a) a single pulse, b) featuring heavy smoothing and c) with the discharge currents.

Plasma density

The plasma density n_e is shown in figure 7.14 for a set of E_p at 1 Pa and a set of pressures E_p = 8.4 J; the corresponding I_d traces are shown in figures 7.12c and 7.13c. Figure 7.14a can be shown without the need for smoothing though figure 7.14b has smoothing over 301 points (12 μs) using an adjacent average function.

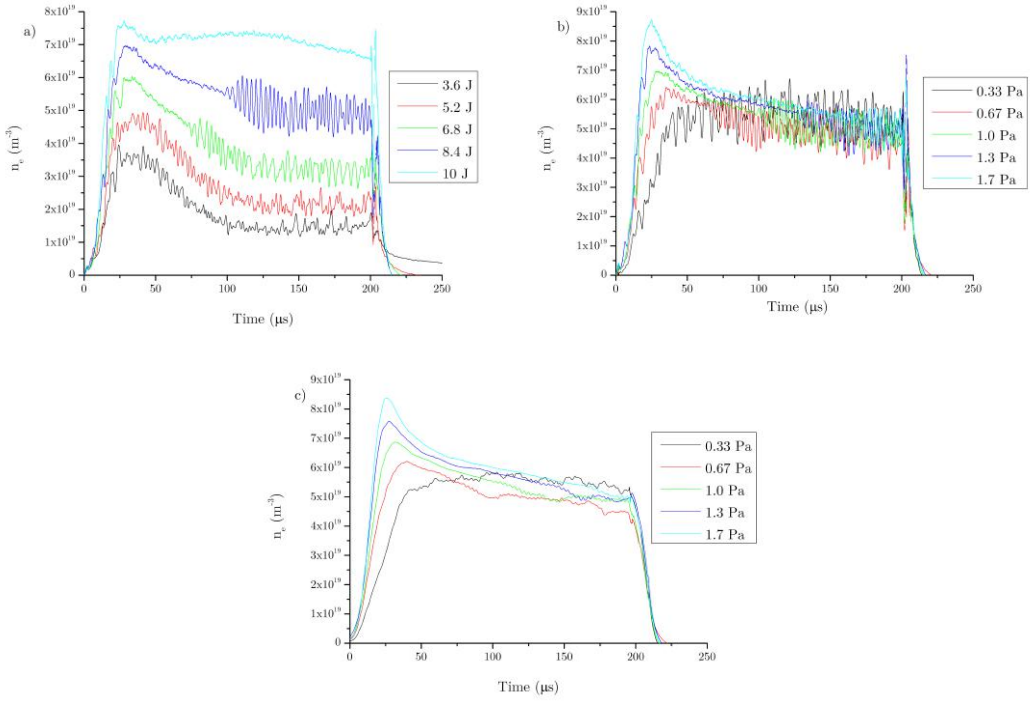

Fig. 7.14 n_e measured 15 mm above the target racetrack for a 200 μs pulse a) for a range of powers from 3.6 - 10 J at 1 Pa, single pulse for a range of pressures at E_p = 8.4 J b) for a single pulse and c) for a single pulse with heavy smoothing (reducing the presence of spokes).

As can be seen from figure 7.14, the major factor affecting n_e is E_p (or I_p) rather than pressure, with pressure only having a major effect on the initial current rise. n_e shows similar trends to I_d, however n_e shows high peaks not seen in I_d. These peaks are more distinct at higher powers and pressures. The fact that these peaks are not seen on the I_d trace could indicate a non-physical phenomenon, such as a change in ion composition (figure 7.10), or that the ions responsible for this peak never reach the target. At this point during the HiPIMS pulse, there is expected to be a high level of rarefaction; this would match an increase in n_e not seen in I_d.

There is also a much sharper decrease in n_e than in I_d.This trend has been observed in figure 10 and is explained by either rarefaction or a change in plasma composition.

Spoke regimes

There are three distinct 'regimes' of spoke that have been observed in the HiPIMS discharge,and each appears under different conditions (regimes). At lower power and pressure, the chaotic regime's spoke mode number is inconsistent and spoke size is constantly varying. As the power increases, spokes become regular and periodic, which is known as the coherent regime. Finally, at higher power the spokes disappear completely,and this is know as the spokeless regime.

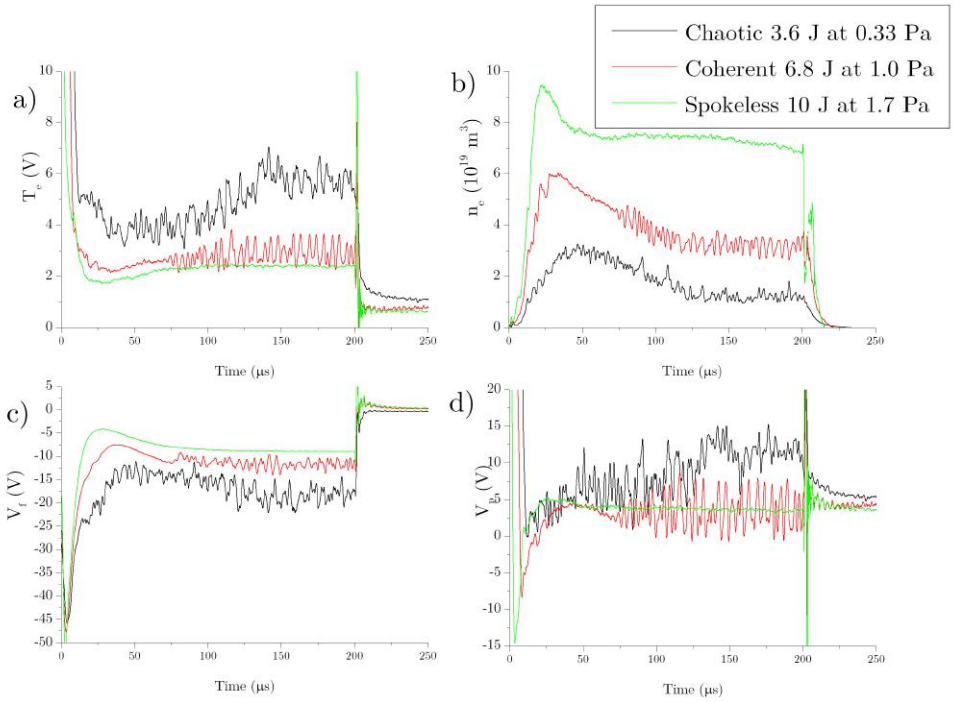

Fig. 7.15 a)T_e b)n_e c)V_f and d)V_p measured by a triple probe 15 mm above the racetrack for three 200 μs pulses representing the chaotic, coherent and spokeless regimes. E_p = 3.6 J, 6.4 J and 10 J at pressures 0.33, 1 and 1.7 Pa.

The values of T_e, n_e, V_f and V_p for typical examples of the chaotic (E_p = 3.6 J, 0.33 Pa), coherent (E_p = 6.8 J, 1 Pa) and spokeless (E_p = 10, J 1.7 Pa) discharges are shown in figure 7.15. The values of I_d and V_d are shown in figure 7.16.

The T_e values are shown in figure 7.15a. As can be seen the coherent and spokeless regimes have reasonably similar values, T_e ~2 - 2.5 eV. However the chaotic regime has T_e $\geq$ 4 eV which is far higher than in either of the other regimes.

The spokeless regime has the highest power and pressure, and as expected it also has the highest n_e. Like the high power cases seen in figure 7.14, there is a peak in n_e during the

peak I_d. However, unlike in the other two cases, this is not followed by a drop in n_e which is not seen in I_d.

Given that the drop in n_e was attributed to a change in plasma composition 7.10, this would imply there is no change in the plasma composition during the spokeless discharge. It can also be observed that the I_d evolution for the spokeless discharge matches that which has been observed for self sputtering [17] [10].

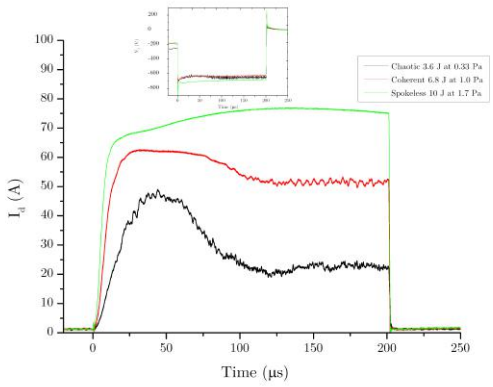

Fig. 7.16 The discharge currents I_d and voltage V_d for a set three 200 μs pulses representing the chaotic, coherent and spokeless regimes. E_p = 3.6 J, 6.4 J and 10 J at pressures 0.33, 1 and 1.7 Pa, shown in figure 7.15

Despite the spokeless regime having nearly twice the level of n_e of the coherent regime, they have very similar T_e.

Conclusions

In this section, the triple probe was used to examine the full HiPIMS pulse at different conditions.

From these findings, a picture of the pulse evolution was derived, whereby T_e is initially high and V_f and V_p are initially negative, and as the pulse continues n_e increases, reaching a peak at the peak I_d. From this peak n_e falls, eventually plateauing. T_e moves inversely, reaching a minimum at the peak I_d, and from there rising to a plateau (except in the E_p = 3.6 J case), however doing so more gradually. V_p and V_f both become less negative after the initial negative peak, while V_f stays negative, and V_p ends positive or $\sim$0 V. These findings are in line with what has been reported elsewhere [136] [137].

The triple probe is further used to investigate the presence of spokes. It was observed that the higher the power and pressure, the later in the pulse the spokes arrive. It was also observed that, while n_e has little effect on spoke, spokes and spokeless discharges are both

seen at the similar values of n_e in figure 7.14b. T_e seems to be the major indicator of spokes, with them found to be mostly absent when $T_e < 2.5$ eV and to have mostly formed at $T_e > 3$ eV, with a transition region at 3 eV $< T_e <$ 2.5 eV.

There was an observed dip in n_e, post peak, not seen in I_p. This dip has two possible explanations; one is that during the peak there is higher density at the triple probe than at the target, which then dissipates (so n_e decreases while I_p remains constant). Alternatively this is an un-physical phenomenon, caused by a change in plasma composition as shown in figure 7.10. Similarly at higher pressures there is a distinct 'peak' in n_e not seen in I_p which is attributed to rarefaction. Both of these effects can be seen simultaneously in figure 7.14.

Investigation of the spokes regimes has shown the chaotic regime having a very high T_e, while the spokeless region has a very high n_e. Despite this high n_e, the coherent and spokeless region both have a similar T_e. While the spokeless condition has the distinctive 'peak' in n_e not seen in I_p, there is no sign of the more gradual fade, which implies that, aside from the initial peak, there is no rarefaction and no change in plasma composition. This would be expected in the self-sputtering regime; additionally the current discharge is similar to the expected I_d in the self-sputtering regime [10].

7.5 Results and analysis from slotted niobium target and strip probes

Discharge parameters

This section is devoted to the use of the triple probe for the study of the oscillations seen in previous sections, the spokes, themselves. Spokes modulation with high amplitude and regular mode number is required for these experiments and these conditions were found to be best satisfied at E_p = 8.4 J and pressure 0.33 Pa. Figure 7.17 shows the I_d and V_d at these conditions.

All the experiments in this section were conducted under these discharge conditions and were conducted using the slotted target and strip probes.

Modulation due to spokes

In the previous section, modulations in the strip probe current I_p were directly linked to spokes. The strip current I_{p1}, I_{p2} and I_{p3} for all strip probes spaced by an arbitrary current separation, are co-plotted on figure 7.18. From this figure, the spoke angular velocity ω = 3.79×10^5 rad s^{-1} and tangential velocity, v = 8.35 km s^{-1} can be calculated as shown, by

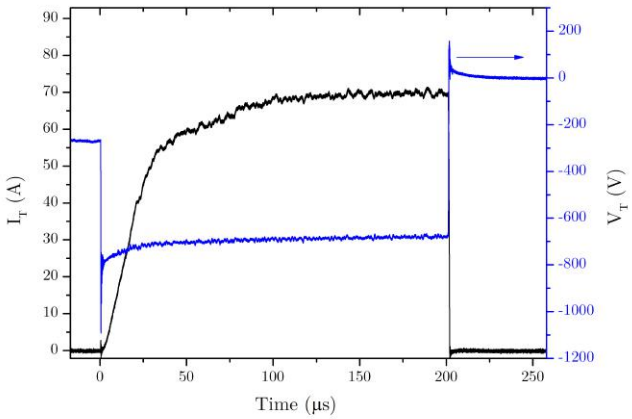

Fig. 7.17 I_d and V_d for a 200 μs pulse at 0.33 Pa and E_p = 8.4 J

measuring the time delay between spoke peaks. This technique is explained in more detail in chapter 5. From this, the mode number can also be determined. The mode number (m = 3) is shown on figure 7.18 as a green trapeze, of width T (one rotation period) = 16.6 μs.

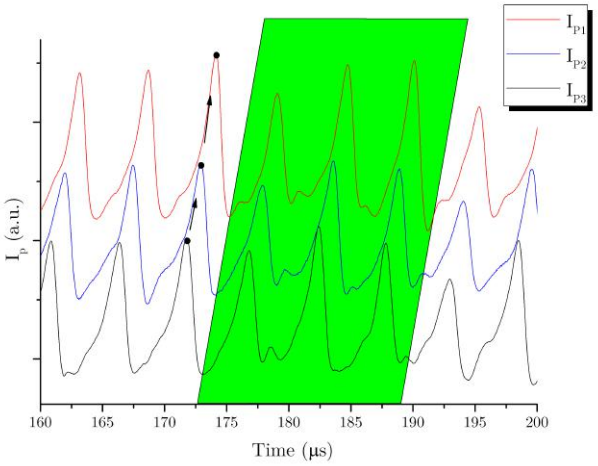

Fig. 7.18 All strip probe currents I_{p1}, I_{p2} and I_{p3} given an arbitrary separation, for a 200 μs pulse at 0.33 Pa and E_p = 8.4 J. The method of calculating spoke velocity is shown, as is one period of rotation which is calculated from the spoke's velocity.

The amplitude of the modulation ΔI_p is 0.54 A. As the peaks in I_p represent the additional current drawn above the base level, it is compared to the minimum value I_b = 0.79 A, meaning ΔI_p / I_b = 68%.

The modulations of all values measured by the triple probe (T_e, n_e, V_p and V_f) are shown in figure 7.19. These modulations were analysed by fast Fourier transform and all were found to have peak frequency ∼180 kHz, matching the frequency of modulation in I_p.

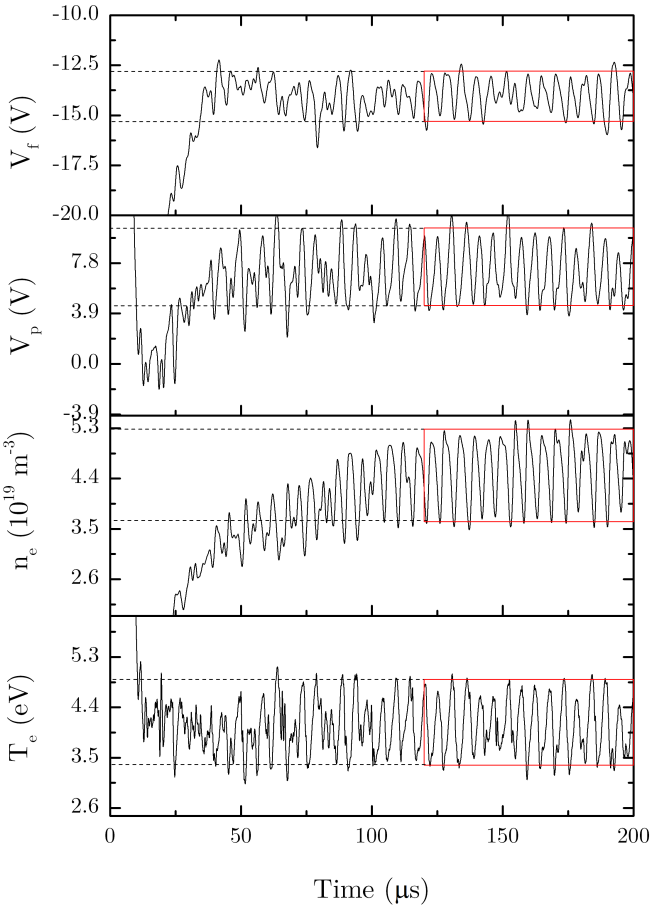

Fig. 7.19 The oscillation in V_f, V_p, T_e and n_e highlighted for a 200 μs pulse at 0.33 Pa and E_p = 8.4 J. with the oscillation amplitude marked.

The amplitudes of the modulations in figure 7.19 are calculated for all values of V_f, V_p, T_e and n_e. The modulations in n_e, like those in I_p, represent additional ionisation above the base level I_p, so they are compared to the minimum value of n_e. Other values like V_f and V_p can only exist as a potential difference and so have no base value to which one can compare. In the case of T_e, its relationship with spokes has yet to be established. T_e modulation is compared to both the mean T_e ($|T_e|$) and $T_{e.b}$, the minimum T_e value.

Δn_e = 1.6 $\times 10^{19}$ m^{-3}, where the minimum n_e, ($n_{e.b}$) = 3.6 $\times 10^{19}$ m^{-3}; giving Δn_e / $n_{e.b}$ = 44 %. ΔT_e = 1.5 eV the modulations in T_e compared to the average T_e ($|T_e|$) = 4.2 eV and the minimum T_e ($T_{e.b}$ = 3.4 eV which yield ΔT_e /$|T_e|$ = 36 % and $\Delta T_e/T_{e.b}$ = 44 % respectively.

V_p and V_f are both potentials and so have no absolute values. ΔV_f = 2.5 V and ΔV_p = 6.0 V.

Phase relationships

All values measured by the triple probe for the last 30 μs of the pulse are shown in figure 7.20, co-plotted with I_{p2} the strip probe current for the strip directly beneath the triple probe. The individual spokes, as defined by the strip probe, are separated in the figure. Because the strip probes are embedded and have been confirmed by the ICCD camera (Chapter 5), they are used as our reference for spokes.

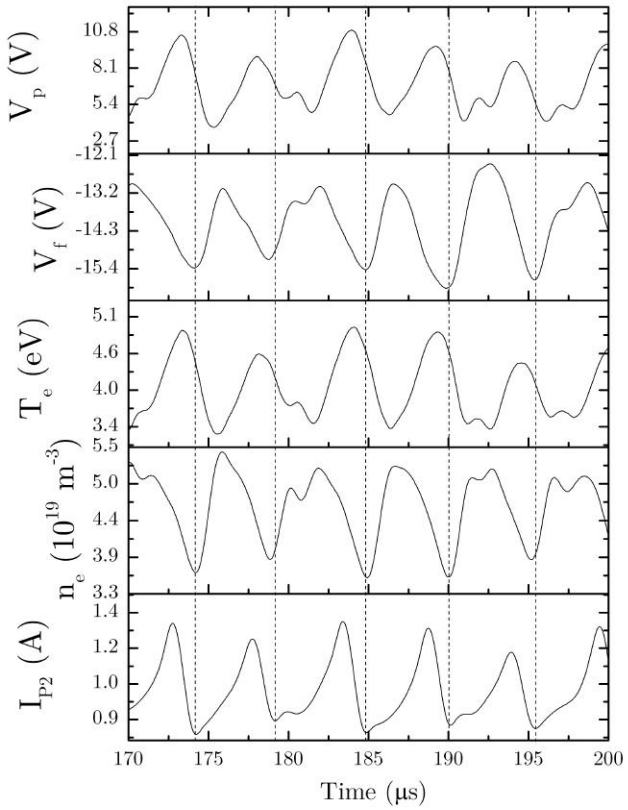

Fig. 7.20 All values measured by the triple probe 15 mm above the target racetrack. Plotted with reference to the strip probe current, for the strip directly beneath it. The spokes are separated by dashed lined for a 200 μs pulse at 0.33 Pa and E_p = 8.4 J.

Figure 7.20 is clearly in agreement with the fast Fourier transform results, showing that the oscillations in I_p, n_e, T_e, V_p and V_f all have very similar frequencies. However these values do not share a single common phase. It can clearly be seen in the figure that there are actually multiple phase relations, with some values seeming to be in phase and some in anti-phase. With all the data presented together as in figure 7.20, the important correlations are hard to isolate. In order to investigate this issue further, figure 7.20 is broken down to show the individual correlations more closely and to compare specific values whose phase or anti-phase are correlated.

Plasma density phase

The peaks in I_{p2} result from spokes with high n_e passing over the strip; therefore it would be expected that n_e and I_{p2} would closely matching in phase. Figure 7.21 shows n_e co-plotted with I_{p2}, as can be seen the valleys of both are closely correlated, with the valleys marked by a dashed line. However the peaks in n_e and I_{p2} come at very different times, with the peak in n_e coming $\sim$1.8 μs before the peak in I_{p2}.

A notable feature of figure 7.21, aside from the phase relations, is that of secondary peaks; these are observed at time 180, 191 and 197 μs on figure 7.21. These secondary peaks are seen as only a slight perturbation in I_p; however they appear as peaks equal to or even exceeding the main peak in n_e.

I_{p2} is a measure of the ion flux through the target side edge of the sheath and it will depend on $n_e T_e^{1/2}$, rather then just n_e. Therefore a better comparison would be between I_{p2} and I_{isat} which is dependent on both n_e and $T_e^{1/2}$. I_{isat} is also shown in figure 7.21, while the introduction of T_e on I_{isat} can be seen because I_{isat}'s peaks occur later then those of n_e, though for the majority of the time the difference is slight ($\Delta t > 0.2$ μs) (although it can be up to 1 μs). However I_{isat} is still more closely correlated to n_e than to I_{p2}.

It appears therefore that the values of n_e directly on the target (the strip probe location) and at the triple probe location (15 mm above the target) are different. Given that in chapter 5 the strip probe current was correlated with camera emission intensity and given the lack of correlation between I_{isat} and I_{p2}, these results strongly suggest that the origin of the optical emissions responsible for spokes are closer then 15 mm from the target.

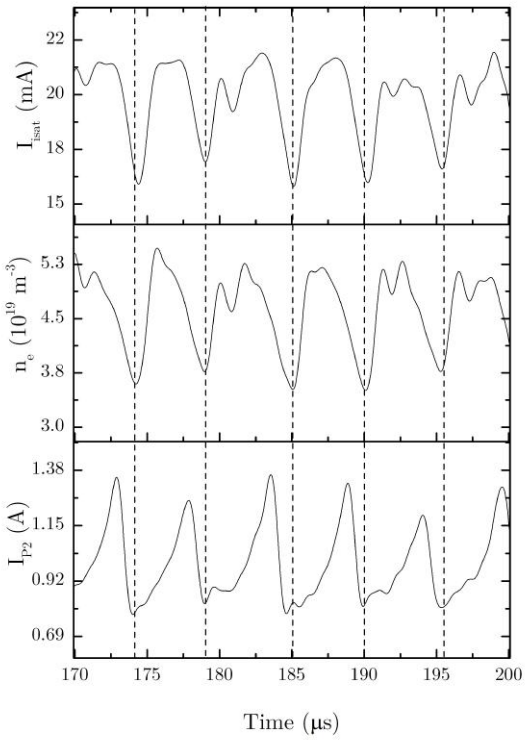

Fig. 7.21 n_e and I_{isat} measured 15 mm above strip probe 2 plotted with reference to the strip probe current I_{p2}. For a 200 μs pulse at 0.33 Pa and E_p = 8.4 J.

Electron temperature phase

Figure 7.22 shows T_e co-plotted with both n_e and I_{p2}; dashed-lines are used here to mark both the peaks and valleys in T_e.

T_e would be expected to be directly out of phase with n_e and it can be seen that the valleys in T_e, either coincide or occur slightly (with a negligible time difference) before the peaks in n_e. However the peaks in T_e occur a significant time ($\sim$0.8 μs) before the valleys of n_e.

While n_e would normally be directly out of phase with T_e, as seen in section 4, spokes have been associated with a variety of heating mechanisms, [100]. Therefore it might be expected that the spokes (as indicated by I_{p2}) would coincide with heating in the plasma around the triple probe. Figure 7.22 shows that the peak in T_e and a peak in I_{p2} occurs at similar times, with the peak in I_{p2} leading by $\sim$0.5 μs.

The delay between the peak in I_{p2} and T_e could be attributed to the thermalisation time for hot electrons. For electrons to have a thermalisation time $\sim$0.5 μs, at plasma density $\sim \times 10^{19}$ m^{-3}, they would need to have a starting energy of $\sim$50 eV [31].

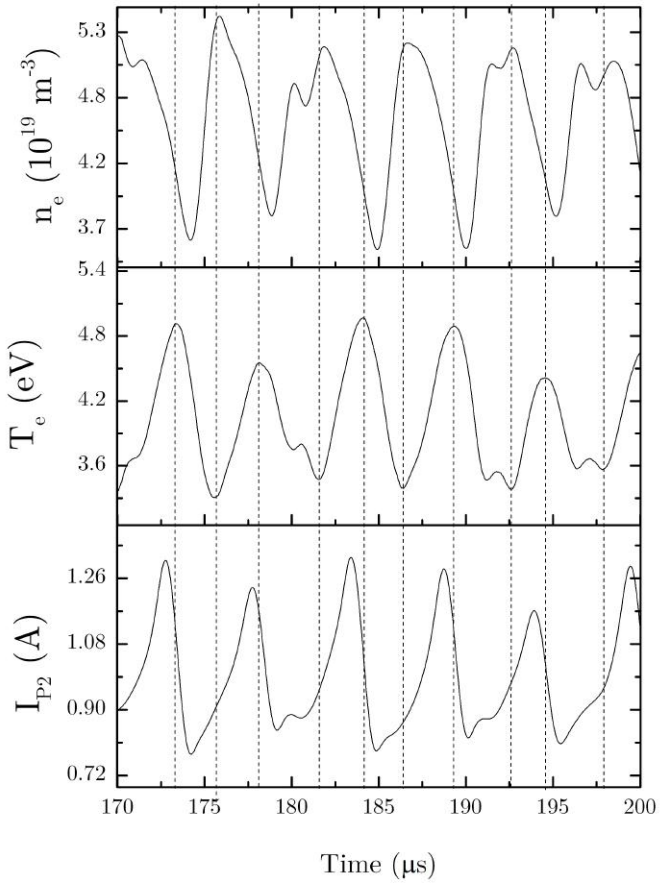

Fig. 7.22 T_e co-plotted with n_e measured 15 mm above strip probe 2 plotted with reference to the strip probe current I_{p2}. For a 200 μs pulse at 0.33 Pa and E_p = 8.4 J, with the peaks and valleys of T_e marked.

An alternative explanation that would not require a thermalisation time would be a jet of hot plasma, either with a travel time to the triple probe position or if given out towards the end of the spoke.

One disadvantage of the triple probe is it only gives a single reading of T_e, so therefore the triple probe cannot detect investigate a secondary electron population.

Floating potential phase

V_f has been used to detect spokes [38] [97] and the triple probe allows us to check this relationship. Figure 7.23 shows V_f co-plotted with n_e. It can be seen that they are closely

correlated, and given the correlation between n_e and I_p seen in figure 7.22, this result indicates that V_f is a good indicator of spokes.

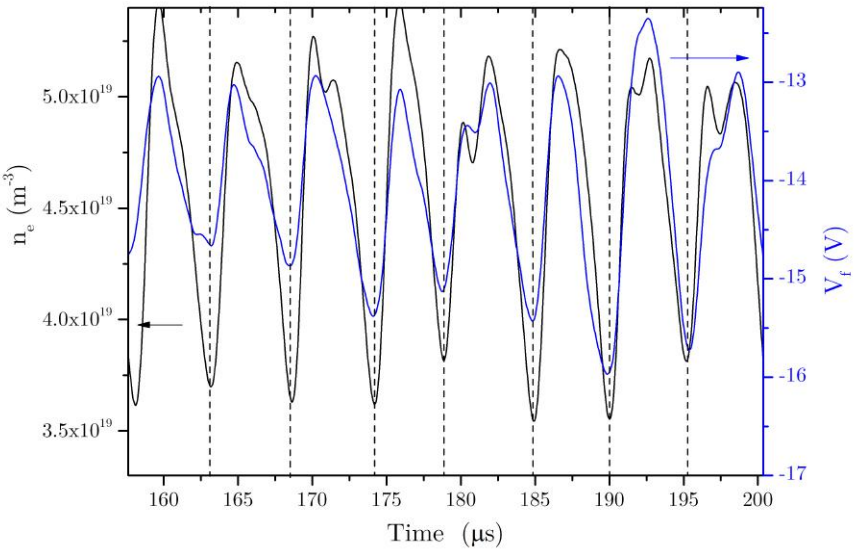

Fig. 7.23 V_f and n_e 15 mm above strip probe 2 co-plotted, with dashed lines showing the correlation, for a 200 μs pulse at 0.33 Pa and E_p = 8.4 J.

Plasma potential phase

V_p is not measured directly, but rather is calculated from V_f and T_e using equation 7.1. For this reason, figure 7.24 shows V_p co-plotted with its two component V_f and T_e. Because V_p is the sum of V_f and 5.2 times T_e, the T_e term dominates.

This means that T_e and V_p are closely correlated, while V_f and T_e (and therefore V_p) seem almost directly out of phase. As V_f and n_e have matching phases, it follows that T_e, and therefore V_p are directly out of phase with V_f. It has been proposed that spokes have a high plasma potential surrounded by a double or triple layer [87] [29] [102], so therefore it would be expected that V_p would be correlated with I_{p2}. It is proposed that the triple probe is too far away to detect this peak in V_p caused by the spoke, as was found in the case of n_e.

7.6 Model of triple probe data

Given the differences between n_e and I_{p2}, it seems apparent that the triple probe measures the plasma just above the spoke rather then the inside of the spoke itself. By taking into account

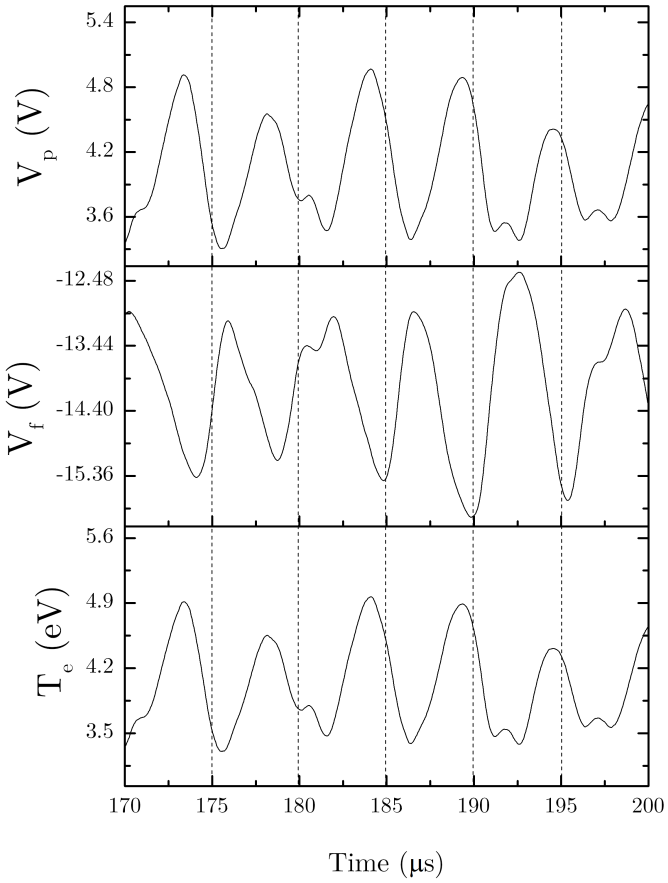

Fig. 7.24 V_f, V_p and T_e measured 15 mm above strip probe 2 plotted with for a 200 μs pulse at 0.33 Pa and E_p = 8.4 J, with dashed lines every 5 μs.

the phase between all the values measured by the triple probe and I_{p2}, a basic model of this region of the plasma and the effect of spokes can be made.

It is proposed that the reason n_e and I_{p2} share valleys is that the passing of the spoke causes rarefaction in the region above. This causes a drop in both n_e and the neutrals available leading to a rise in both T_e and V_p. As time progresses, n_e increases, leading to a decrease in T_e. Eventually the spoke passes, causing rarefaction, decreasing n_e, and causing heating, increasing T_e.

This idea matches existing theory as spokes have been predicted to cause both rarefaction and heating [100] [86].

7.7 Summary and Conclusion

Section 2 of this chapter details the process by which the final design of the triple probe was reached. It details how and why voltage mode, the battery bias (V_{31} of 30-40 V) and the simple circuit design (figure 7.6), were chosen. The results of testing the triple probe against the more standard single Langmuir probe technique are also detailed. From the various tests, it was shown that the triple probe gave results within error of the standard Langmuir probe results, without the need to be averaged over multiple pulses.

While measurements of V_f and V_p could be obtained by other means, the only way to measure T_e and n_e during a single pulse is by using the triple probe. This makes the triple probe a very useful technique for measuring spokes.

The triple probe was setup as described in section 3, and used to investigate T_e, n_e, V_f and V_p for a set of HiPIMS pulses. In section 4, we reported results and general trends found during the pulse, as well as many matching results from previous studies which use single Langmuir probes or other equipment. These investigations were followed up by investigating more directly the effects of power and pressure on n_e and T_e.

From these findings, a picture of the pulse evolution was derived, whereby T_e is initially high and V_f and V_p are initially negative. As the pulse continues n_e increases, reaching a peak at the peak I_d. From this peak, n_e falls, eventually plateauing. T_e moves inversely, reaching a minimum at the peak I_d, and from there rising to a plateau (except in the low power case), however doing so more gradually. V_p and V_f both become less negative after the initial negative peak, while V_f stays negative, and V_p ends positive or $\sim$0 V.

There is a drop in n_e after the peak (not mirrored in I_d). This could either be due to the ion composition changing from Ar to Nb or due to refraction having given a higher n_e away from the target during the initial I_d peak falling off.

The onset of spokes was found to be more related to T_e, with spokes unlikely to be absent if $T_e < 2.5$ eV and very likely to be absent if $T_e > 3$ eV.

To investigate this further, T_e, n_e, V_f and V_p for three HiPIMS pulses representing the chaotic, coherent and spokeless regimes respectively were plotted. The chaotic condition was found to have the highest T_e and V_p. T_e was lower for the spokeless condition but seemed however not to be significantly lower than for the coherent case. Another notable feature of the spokeless condition was the lack of a n_e drop after the initial peak and apart from a peak in n_e at the peak I_d.

This indicates that the mechanism behind the fall in n_e, whether it be change in plasma composition or rarefaction, is absent in the spokeless condition.

In section 5, three strip probes were used with the triple probe to investigate spokes for a 200 μs pulse at 0.33 Pa and E_p = 8.4 J. The magnitude of perturbations due to spokes was investigated first and it was found that $\Delta n_e/n_{e.b}$ = 44 % and $\Delta T_e/|T_e|$ = 42 %, $\Delta T_e/T_{e.b}$ = 54 % at conditions where $\Delta I_p/I_b$ = 68%.

Investigation of the oscillation phases revealed n_e to be in phase with V_f, and sharing valleys with I_p. However the peaks in I_p and n_e (as well as I_{isat}) occur at different times indicating that the perturbations seen in the the triple probe are not direct measurements of spokes, but rather of the plasma above the spokes.

T_e shows signs of anti-phase with n_e, though the peaks in I_{p2} also seem to have an influence on T_e, indicating a heating effect from the spokes, as predicted by Anders [100]. V_p was calculated from equation 7.1 so naturally V_p was closely correlated with T_e and therefore out of phase with n_e.

This was summarised in a model where spokes cause heating and rarefaction in the plasma above them.

While measurements of V_f and V_p could be obtained by other means, the only way to measure T_e and n_e during a single pulse is using the triple probe. Here a relatively limited study of the effect of the plasma just above the spokes is presented, yet as shown above interesting and unique conclusions can still be drawn. This established that the triple probe is a valuable tool for investigating spokes.

Chapter 8

Conclusions and suggested future work

8.1 Conclusions

The purpose of this study was to investigate spokes in HiPIMS, and to use the knowledge gained through this investigation to advance the HiPIMS deposition technique, with the specific focus of improving thin niobium film. To this end, a variety of diagnostic techniques were both developed and used. The strip probe is a new diagnostic technique developed during this project, and it is able to detect spokes by the change in local discharge current that they cause.

The use of strip probe to detect spokes is discussed in chapter 5. Perturbations were detected in the strip probe current I_p which were not observed on the total discharge current I_d. At low power or near the beginning of the pulse, the perturbations in I_p were small or non-existent. However later, during higher power pulses, the perturbations in I_p became regular and were attributed to the effect of spokes. The strip probe was used simultaneously with fast imaging to confirm that the presence of the perturbation in I_p coincided with spokes visible on the target. Using three strip probes on one target, the spokes' velocity could be measured. It is measured from the time delay between the current peaks over different strips, with strips having an angular separation. The spoke velocity measured by the strips in fact matched closely the spoke velocity measured by two camera images taken 3 μs apart, further confirming the perturbations in the strip probe to be spokes.

Unlike the camera, the strip probe gives a continues reading for the whole HiPIMS pulse, which means that the spoke velocity throughout the pulse can be measured. It was found that the spoke velocity on an aluminium target increases from 6.95 km s^{-1} when spokes are first detected (around 20 μs into the pulse), to 9.79 km s^{-1} by the end of the pulse. This change in velocity was attributed to a change in the backing gas from being argon dominated to being dominated by sputtered metal. The final velocity of 9.79 km s^{-1} is higher then the

CIV of either argon or aluminium and it is proposed that this is the result of the racetrack radius changing throughout the pulse. However, in the case of a niobium target, a spoke velocity of 13.5 km s^{-1} was recorded, far higher then the CIV of either argon or niobium. These results were taken at very low pressure, 0.14 Pa, and this low pressure was given as the reason for the spoke velocity far exceeding that of the CIV.

The amplitude of the perturbations was observed to change in response to power and to pressure; as well as the amplitude response, the perturbations also seemed to change in nature. At low power and pressure, the perturbations were chaotic and of low amplitude (the chaotic regime), but as the current and power was increased, the perturbations became higher in amplitude and more periodic (the coherent regime). At the highest power and pressure, the spokes disappeared completely (the spokeless regime). The maximum spoke amplitude was $\Delta I_p/I_b = 0.52$ and occurred at $E_p = 1.6$ J and 0.7 Pa for an aluminium target with argon backing gas. This result was surprising as it has been proposed that the spokes carry up 100% of the target current.

The strip probe and optical imaging techniques were found to be complementary; the strip probes can be used to detect spokes at a specific point on the target for the entire discharge, whereas the camera takes an image of the whole target at a single moment in time. However, using the spoke velocity, the strip probe output over one period of rotation can be convolved with a Gaussian radial distribution to produce an "image" of the spokes. Similarly, by taking a track around the racetrack circumference, an 1D optical intensity against time trace, comparable to I_p, can be made. The 1D optical intensity trace was found to be very closely correlated with I_p over the same time interval. This leads to the theory that both I_p and the optical emission intensity are proportional to $n_e T_e^{1/2}$ above the target.

Finally, the strip probe was used with optical emission intensity to investigate spoke splitting and merging. It has been proposed that during spoke merging, the leading spoke expands, causing the spoke which follows to shrink and then catch up to the lead spoke. The strip probe observed examples of spoke merging but found the following spoke did not reduce in size. This finding led to a new theory of spokes spreading to merge being proposed.

Spoke splitting was observed as the only mechanism whereby the spoke mode number increases, rather than spontaneous spoke creation. The total target current before and after this split was found to be the same.

In Chapter 6, an investigation into the effects of altering the power and pressure on the amplitude of spokes was conducted using a niobium target. These experiments were done with an enhanced power supply, to access a fuller range of conditions. This investigation was conducted with the intention of finding the trends in spoke amplitude in reaction to power and pressure. It was found that at each pressure, there exists an optimum power at which

the spoke amplitude is at a maximum. It is suggested that this is related to the different spoke behaviours: like in aluminium, there are three regimes of spokes; chaotic, coherent and spokeless. It was found that I_p in the coherent regime cannot exceed I_p in the spokeless regime. As the pressure increases, the power required to enter the spokeless regime reduces, so the optimum power at which there is a maximum spoke amplitude changes.

The effect of the different spoke regimes on sputtered films was investigated in comparison to DC sputter films at the same pressure. A set of films were created at:
The chaotic condition, at pressure 0.33 Pa, E_p = 3.6 J, f = 70 Hz and I_A = 0.39 A.
The coherent condition, at pressure 0.33 Pa, E_p = 6.8 J, f = 37 Hz and I_A = 0.37 A.
The spokeless condition, at pressure 1.7 Pa, E_p = 10 J, f = 25 Hz and I_A = 0.34 A.
Where I_A is the average power. Two films were made using a DC discharge at the same average power at pressures of 0.33 Pa (I_A = 0.7 A) and 1.7 Pa (I_A = 0.9 A) respectively. All samples were deposited at 250 W for 3.5 hour; 9 samples were made per depositing run at angles of: 9° (side-on), 45° and directly facing the target.

The deposition rate of the samples were analysed by FIB and SEM, while the surface morphology was analysed by SEM and XRD was used to investigate the lattice dimensions. The DC case always had the highest deposition rate, though the rate was similar in the spokeless condition when normalised to current.

The deposition rate at different angles was also measured. It was found that the samples deposited at 45 ° to the target had the highest deposition rate. The only exception was the case of coherent spokes, where the highest deposition rate was found for samples directly facing the target. The spokeless and coherent conditions both showed a higher proportion of deposit to the side than in the DC cases, though pressure was always the dominant factor.

Investigations of surface morphology revealed that the pressure was the dominant effect. The films deposited at low pressure showed a dense film with a small grain size, and with no apparent difference between the chaotic and coherent regimes. In contrast, the higher pressure conditions show a columnar structures for both the spokeless and DC cases, though the spokeless case shows a smaller grain size and more dense film. The spokeless case is also the only film which shows significant signs of different morphogenesis at different angles, with the smallest grains observed at the side on position and the largest at 45°.

The films were further analysed by XRD. This revealed that in all spoke conditions, the lattice spacing of the preferred grain orientation (1 1 0) shows signs of ion bombardment, though the low pressure DC case did not. Outside of the spokeless case, the angle of deposition did not have a major effect. There was also little effect from different spoke conditions, with the greatest differences in the results being due to pressure.

Overall these investigations showed that pressure has a greater effect on the surface morphology and deposition rate of films than the regimes of spokes.

Another plasma analysis tool capable of investigating HiPIMS is the triple probe, which is able to take readings of n_e, T_e, V_p and V_f with time resolution limited only by ω_p, the plasma frequency. In chapter 7, the triple probe is used to take plasma measurements inside the magnetron trap 15 mm above the target racetrack. The triple probe is used in a range E_p from 3.6 to 10 J and a pressure from 0.33 Pa to 1.7 Pa, both in steps of five.

First the triple probe is used to investigate a full HiPIMS pulse at E_p = 6.8 J and a pressure of 1.0 Pa. The findings are used to derive a picture of the pulse evolution, whereby T_e is initially high and V_f and V_p are initially negative, and as the pulse continues n_e increases, reaching a peak at the peak I_d. From this peak, n_e falls, eventually plateauing. T_e moves inversely, reaching a minimum at the peak I_d, and from there rising to a plateau (except in the E_p = 3.6 J case), though doing so more gradually then n_e. V_p and V_f both become less negative after the initial negative peak, while V_f stays negative, and V_p ends positive or $\sim$0 V. These findings are in line with what has been reported elsewhere in the previous literature using different techniques.

The triple probe is further used to investigate the presence of spokes. It was observed that, the higher are the power and the pressure, the later in the pulse that the spokes arrive. It was also observed that spokes can either be present or not at similar values of n_e, indicating n_e has less effect on their formation. T_e appears to be the major indicator of spokes; they are mostly absent when $T_e < 2.5$ eV and have mostly formed when $T_e > 3$ eV, with a transition region at 3 eV $< T_e <$ 2.5 eV.

Investigation of spokes' regimes revealed that the chaotic regime had a very high T_e, while the spokeless region had a very high n_e. Despite the difference in n_e, the coherent and spokeless region have similar T_e, although T_e is lower in the spokeless case.

The triple probe was then used simultaneously with the strip probe to investigate spokes directly, in particular the phase and the relationship between different measured values for a pulse at E_p = 8,4 pressure 0.33 Pa (n_e T_e V_p and V_f). This revealed that n_e is in phase with V_f, and also shares valleys with I_p. However the peaks in I_p and n_e (as well as I_{isat}) occur at different times, indicating that the perturbations seen in the triple probe are not direct measurements of spokes, but rather the plasma above the spokes.

T_e shows signs of anti-phase with n_e, though the peaks in I_{p2} also seem to have an influence on T_e, indicating a heating effect from the spokes; this idea is supported by the literature. Since V_p was calculated from a dominant factor of T_e, it is unsurprising that V_p is closely correlated with T_e and therefore out of phase with n_e.

Given the differences between n_e and I_{p2}, it seems apparent that the triple probe measures the plasma just above the spoke rather then the inside of the spoke itself. By taking into account the phase between all the values measured by the triple probe and I_{p2}, a basic model of this region of the plasma and the effect of spokes can be made.

It is proposed that the reason n_e and I_{p2} share valleys is that the passing of the spoke causes rarefaction in the region above. This causes a drop in n_e, leading to a rise in both T_e and V_p. As time progresses, n_e increases as the area refills, leading to a decrease in T_e. Eventually the spoke passes again, causing rarefaction, decreasing n_e, and causing heating which increases T_e.

8.2 Suggested future work

Future work in the field of spokes

The main purpose of this thesis has been to investigate HiPIMS with a specific focus on the new discovery of spokes. Before the start of this PhD, it had been found that ions are ejected asymmetrically side-on from the target. This asymmetrical ion ejection was linked to rotating regions of high energy ionisation (spokes), making them an area of great interest, due to the importance of high energy ions in the production of higher quality thin films.

Over the time of this PhD, the understanding of spokes in HiPIMS has been advanced greatly. The major areas of progress have been the development of a theory of spoke motion and formation as well as a theory explaining the generation of high energy ions in spokes. Both of these theories are presented in chapter 2. The scope of spokes research has been significantly altered by the discovery that spokes are present in nearly all DC magnetron discharges, not just in HiPIMS. However the spokes during the low power (DC) discharge behave very differently from the spokes observed in HiPIMS. Additional work here and by others has shown that even in HiPIMS, the spokes have different regimes and even if the spokes are not present in the 'spokeless' regime, high energy ions can be detected.

The initial interest in spokes was due to their link to the production of high energy ions. However spokes are observed in low power DC where there are no high energy ions, and high energy ions are observed in the spokeless HiPIMS regime. Thus, their study may become less relevant unless research can link spokes to the production of a better quality of thin films.

Due to the wide range of conditions at which spokes are observed, they are likely to remain an area of academic interest until there is a theory explaining the difference in spoke behaviour at different discharge powers, spoke regimes and the transitions between them.

While there has been preliminary work, including this thesis, to investigate spoke transitions and the effect of spokes on thin films, much more work is needed in both areas.

Future applications of work in this project

Chapter 5 used the strip probe alongside ICCD imaging to demonstrate that the strip probe is able to detect spokes' velocity as well as their amplitude and regime. As cameras can often be expensive or require impractical optics, the research in Chapter 5 suggests that the strip probe can be used as an alternative method to imaging for detecting spokes, and this is successfully implemented in later chapters. Future work can use strip probes in the same way.

Chapter 6 uses the strip probe to detect the chaotic, coherent and spokeless regimes for argon and niobium discharge. These results were similar to the Aluminium case. This suggests that all discharges have the same spoke amplitude and regime trends; a further study which investigates the multiple spoke amplitude and regimes using multiple target materials and backing gases could be useful for industry, where magnetrons are used but no diagnostics capable of measuring spokes can be fitted. For the same reasons, analysing the effect of factors such as magnetic field strength and target wear on spoke regimes would also be of interest.

The degree of interest would depend whether spokes' regimes or amplitudes can be shown to have a significant effect on film deposition. The results in chapter 6 did not indicate that there was any significant differences due to spokes, especially when compared to pressure. The experiments conducted in chapter 6 were very early stage ones, and future experiments, conducted in a purpose built deposition rig which was able to conduct sample heating, biasing and study all three spoke regimes at the same pressure, may yield different results. Moreover determining the ion energy distribution at different angle and spoke conditions before deposition would allow the effect of spoke conditions to be more directly related to surface morphology.

Finally, future work could also build from the limitations of chapter 6. One such limitation was that the triple probe only outputs one value of T_e. The most obvious further work to be recommended would therefore be to place a Langmuir probe in the triple probe position. This would allow the electron energy distribution function (EEDF) to be measured. While this result will not be able to measure the effect of individual spokes, it would be able to measure the EEDF of high energy electrons in the plasma, which the triple probe is unable to detect.

References

[1] P. A. Ni, C. Hornschuch, M. Panjan, and A. Anders, "Plasma flares in high power impulse magnetron sputtering," *Applied Physics Letters*, vol. 101, no. 22, 2012.

[2] F.F.Chen, *Introduction to plasma physics and controlled fusion*, vol. 53. 1989.

[3] I. Langmuir, "Oscillations in ionied gases," vol. 14, pp. 627–637, 1928.

[4] D. Pines and J. Schrieffer, "Collective Behaviour in solid-state plasmas," *Physical reveiw*, vol. 124, no. 5, p. 1387, 1961.

[5] G. Livadiotis and D. J. McComas, "Electrostatic shielding in plasmas and the physical meaning of the Debye length," *Journal of Plasma Physics*, vol. 80, no. 03, pp. 341–378, 2014.

[6] R. M. Kulsrud, J. W. K. Mark, and A. Caruso, "The hose-pipe instability in interstellar plasma," *Astrophysics and Space Science*, vol. 14, no. 1, pp. 52–55, 1971.

[7] W. D. Westwood, "Glow discharge sputtering," *Progress in Surface Science*, vol. 7, no. 2, pp. 71–111, 1976.

[8] R. K. Waits, "Planar magnetron sputtering," *Journal of Vacuum Science and Technology*, vol. 15, no. 2, pp. 179–187, 1978.

[9] W. D. Gill and E. Kay, "Efficient low pressure sputtering in a large inverted magnetron suitable for film synthesis," *Review of Scientific Instruments*, vol. 36, no. 3, pp. 277–282, 1965.

[10] J. T. Gudmundsson, N. Brenning, D. Lundin, and U. Helmersson, "High power impulse magnetron sputtering discharge," *Journal of Vacuum Science & Technology A: Vacuum, Surfaces, and Films*, vol. 30, no. 2012, p. 030801, 2012.

[11] S. Calatroni, "20 Years of experience with the Nb/Cu technology for superconducting cavities and perspectives for future developments," *Physica C: Superconductivity and its Applications*, vol. 441, no. 1-2, pp. 95–101, 2006.

[12] H. Padamsee, "The science and technology of superconducting cavities for accelerators," *Superconductor Science and Technology*, vol. 14, no. 4, pp. R28–R51, 2001.

[13] C. Benvenuti, N. Circelli, and M. Hauer, "Niobium films for superconducting accelerating cavities," *Applied Physics Letters*, vol. 45, no. 5, pp. 583–584, 1984.

[14] V. Kouznetsov, K. Macák, J. M. Schneider, U. Helmersson, and I. Petrov, "A novel pulsed magnetron sputter technique utilizing very high target power densities," *Surface and Coatings Technology*, vol. 122, no. 2-3, pp. 290–293, 1999.

[15] P. Poolcharuansin, M. Bowes, T. J. Petty, and J. W. Bradley, "Ionized metal flux fraction measurements in HiPIMS discharges," *Journal of Physics D: Applied Physics*, vol. 45, p. 322001, 2012.

[16] J. Bohlmark, J. Alami, C. Christou, a. P. Ehiasarian, and U. Helmersson, "Ionization of sputtered metals in high power pulsed magnetron sputtering," vol. 18, no. 2005, 2005.

[17] A. Anders, "Discharge physics of high power impulse magnetron sputtering," *Surface and Coatings Technology*, vol. 205, pp. S1–S9, 2011.

[18] J. Lin, W. D. Sproul, J. J. Moore, Z. Wu, S. Lee, R. Chistyakov, and B. Abraham, "Recent advances in modulated pulsed power magnetron sputtering for surface engineering," *Jom*, vol. 63, no. 6, pp. 48–58, 2011.

[19] K. Sarakinos, J. Alami, and S. Konstantinidis, "High power pulsed magnetron sputtering: A review on scientific and engineering state of the art," *Surface and Coatings Technology*, vol. 204, no. 11, pp. 1661–1684, 2010.

[20] S. M. Rossnagel, "Metal ion deposition from ionized mangetron sputtering discharge," *Journal of Vacuum Science & Technology B: Microelectronics and Nanometer Structures*, vol. 12, no. 1, p. 449, 1994.

[21] J. Alami, P. O. a. Persson, D. Music, J. T. Gudmundsson, J. Bohlmark, and U. Helmersson, "Ion-assisted physical vapor deposition for enhanced film properties on nonflat surfaces," *Journal of Vacuum Science & Technology A: Vacuum, Surfaces, and Films*, vol. 23, no. 2, p. 278, 2005.

[22] J. T. Gudmundsson, "Ionized physical vapor deposition (IPVD): magnetron sputtering discharges," *Journal of Physics: Conference Series*, vol. 100, no. 8, p. 082002, 2008.

[23] W. Breilmann, a. Eitrich, C. Maszl, a. Hecimovic, V. Layes, J. Benedikt, and a. von Keudell, "High power impulse sputtering of chromium: correlation between the energy distribution of chromium ions and spoke formation," *Journal of Physics D: Applied Physics*, vol. 48, no. 29, p. 295202, 2015.

[24] U. Helmersson, M. Lattemann, J. Bohlmark, A. P. Ehiasarian, and J. T. Gudmundsson, "Ionized physical vapor deposition (IPVD): A review of technology and applications," *Thin Solid Films*, vol. 513, pp. 1–24, 8 2006.

[25] A. Hecimovic, K. Burcalova, and A. P. Ehiasarian, "Origins of ion energy distribution function (IEDF) in high power impulse magnetron sputtering (HIPIMS) plasma discharge," *Journal of Physics D: Applied Physics*, vol. 41, no. 9, p. 095203, 2008.

[26] J. Vlček, P. Kudláček, K. Burcalová, and J. Musil, "Ion flux characteristics in high-power pulsed magnetron sputtering discharges," *Europhysics Letters (EPL)*, vol. 77, p. 45002, 2007.

[27] D. Lundin, M. Čada, and Z. Hubička, "Ionization of sputtered Ti, Al, and C coupled with plasma characterization in HiPIMS," *Plasma Sources Science and Technology*, vol. 24, no. 3, p. 035018, 2015.

[28] M. Panjan, R. Franz, and A. Anders, "Asymmetric particle fluxes from drifting ionization zones in sputtering magnetrons," *Plasma Sources Science and Technology*, vol. 23, no. 2, p. 025007, 2014.

[29] C. Maszl, W. Breilmann, J. Benedikt, and a. von Keudell, "Origin of the energetic ions at the substrate generated during high power pulsed magnetron sputtering of titanium," *Journal of Physics D: Applied Physics*, vol. 47, p. 224002, 2014.

[30] M. a. Raadu, I. Axnäs, J. T. Gudmundsson, C. Huo, and N. Brenning, "An ionization region model for high-power impulse magnetron sputtering discharges," *Plasma Sources Science and Technology*, vol. 20, no. 6, p. 065007, 2011.

[31] A. Anders, P. Ni, and A. Rauch, "Drifting localization of ionization runaway: Unraveling the nature of anomalous transport in high power impulse magnetron sputtering," *Journal of Applied Physics*, vol. 111, no. 5, 2012.

[32] A. Vetushka and A. P. Ehiasarian, "Plasma dynamic in chromium and titanium HIPIMS discharges," *Journal of Physics D: Applied Physics*, vol. 41, no. 1, p. 015204, 2008.

[33] P. Poolcharuansin and J. W. Bradley, "Short- and long-term plasma phenomena in a HiPIMS discharge," *Plasma Sources Science and Technology*, vol. 19, no. 2, p. 025010, 2010.

[34] J. Bohlmark, M. Östbye, M. Lattemann, H. Ljungcrantz, T. Rosell, and U. Helmersson, "Guiding the deposition flux in an ionized magnetron discharge," *Thin Solid Films*, vol. 515, pp. 1928–1931, 12 2006.

[35] G. Clarke, A. Mishra, P. J. Kelly, and J. W. Bradley, "Cathode current density distributions in high power impulse and direct current magnetron sputtering modes," *Plasma Processes and Polymers*, vol. 6, pp. 548–553, 2009.

[36] T. D. L. Arcos, V. Layes, Y. A. Gonzalvo, V. S.-v. D. Gathen, a. Hecimovic, and J. Winter, "Current–voltage characteristics and fast imaging of HPPMS plasmas: transition from self-organized to homogeneous plasma regimes," *Journal of Physics D: Applied Physics*, vol. 46, p. 335201, 2013.

[37] A. Hecimovic, C. Maszl, V. Schulz-von der Gathen, M. Böke, and A. von Keudell, "Spoke rotation reversal in magnetron discharges of aluminium, chromium and titanium," *Plasma Sources Science and Technology*, vol. 25, no. 3, p. 035001, 2016.

[38] a. Hecimovic, M. Böke, and J. Winter, "The characteristic shape of emission profiles of plasma spokes in HiPIMS: the role of secondary electrons," *Journal of Physics D: Applied Physics*, vol. 47, no. 10, p. 102003, 2014.

[39] G. J. . Winter, a. Hecimovic, T. . D. los Arcos, M. Böke, and V. Schulz-von der Gathen, "Instabilities in high-power impulse magnetron plasmas: from stochasticity to periodicity," *Journal of Physics D: Applied Physics*, vol. 46, no. 8, p. 084007, 2013.

[40] X. Chen and P. Han, "On the thermodynamic derivation of the Saha equation modified to a two-temperature plasma," *Journal of Physics D: Applied Physics*, vol. 32, no. 14, pp. 1711–1718, 1999.

[41] R. Wijsman, "Breakdown ProbabiTity of a Low Pressure Gas Discharge," *Physical Review*, vol. 75, no. 5, pp. 833–838, 1949.

[42] K. T. A. L. Burm, "Plasma: The fourth state of matter," *Plasma Chemistry and Plasma Processing*, vol. 32, no. 2, pp. 401–407, 2012.

[43] P. W. Blum and H. J. Fahr, "Interaction between Interstellar Hydrogen and the Solar Wind," *Astron. Astrophys.*, vol. 4, no. 2, pp. 280–290, 1970.

[44] A. L. Peratt, "Advances in numerical modeling of astrophysical and space plasmas," *Astrophysics and Space Science*, vol. 242, pp. 93–163, 1996.

[45] J. Nuckolls, L. Wood, A. Thiessen, and G. Zimmerman, "Laser Compression of Matter to Super-High Densities: Thermonuclear (CTR) Applications," *Nature*, vol. 239, p. 139, 1972.

[46] G. Bonizzoni and E. Vassallo, "Plasma physics and technology; Industrial applications," *Vacuum*, vol. 64, no. 3-4, pp. 327–336, 2002.

[47] B. J. Garrison, "Energy and angular distributions of atoms sputtered from polycrystalline surfaces: Thompson and beyond," *Nuclear Inst. and Methods in Physics Research, B*, vol. 40-41, no. PART 1, pp. 313–316, 1989.

[48] a. V. Phelps and Z. L. Petrovic, "Cold-cathode discharges and breakdown in argon: surface and gas phase production of secondary electrons," *Plasma Sources Science and Technology*, vol. 8, no. 3, pp. R21–R44, 1999.

[49] H. D. Hagstrum, "Theory of auger ejection of electrons from metals by ions," *Physical Review*, vol. 96, no. 2, pp. 336–365, 1954.

[50] R. A. Baragiola, E. V. Alonso, J. Ferron, and A. Oliva-Florio, "Ion-induced electron emission from clean metals," vol. 90, no. 1928, pp. 240–255, 1979.

[51] O. G. Schmidt, O. Kienzle, Y. Hao, K. Eberl, and F. Ernst, "Modified Stranski–Krastanov growth in stacked layers of self-assembled islands," *Applied Physics Letters*, vol. 74, no. 9, pp. 1272–1274, 1999.

[52] A. Anders, "A structure zone diagram including plasma-based deposition and ion etching," *Thin Solid Films*, vol. 518, no. 15, pp. 4087–4090, 2010.

[53] J. A. Thornton, "The microstructure of sputter-deposited coatings," *Journal of Vacuum Science & Technology A: Vacuum, Surfaces, and Films*, vol. 4, no. 6, p. 3059, 1986.

[54] S. M. Rossnagel, "Induced drift currents in circular planar magnetrons," *Journal of Vacuum Science & Technology A: Vacuum, Surfaces, and Films*, vol. 5, no. 1, p. 88, 1987.

[55] P. C. Zalm, "Some useful yield estimates for ion beam sputtering and ion plating at low bombarding energies," *Journal of Vacuum Science & Technology B: Microelectronics and Nanometer Structures*, vol. 2, no. 2, p. 151, 1984.

[56] C. Huo, M. A. Raadu, D. Lundin, J. T. Gudmundsson, A. Anders, and N. Brenning, "Gas rarefaction and the time evolution of long high-power impulse magnetron sputtering pulses," *Plasma Sour. Sci. Technol.*, vol. 21, no. 4, p. 045004, 2012.

[57] S. Kadlec, "Simulation of Neutral Particle Flow During High Power Magnetron Impulse," *Plasma Processes and Polymers*, vol. 4, pp. S419–S423, 4 2007.

[58] P. Vašina, M. Meško, L. de Poucques, J. Bretagne, C. Boisse-Laporte, and M. Touzeau, "Study of a fast high power pulsed magnetron discharge: role of plasma deconfinement on the charged particle transport," *Plasma Sources Science and Technology*, vol. 17, no. 3, p. 035007, 2008.

[59] A. Rauch and A. Anders, "Estimating electron drift velocities in magnetron discharges," *Vacuum*, vol. 89, no. 1, pp. 53–56, 2013.

[60] B. Liebig and J. W. Bradley, "Space charge, plasma potential and electric field distributions in HiPIMS discharges of varying configuration," *Plasma Sources Science and Technology*, vol. 22, no. 4, p. 045020, 2013.

[61] A. Mishra, P. J. Kelly, and J. W. Bradley, "The evolution of the plasma potential in a HiPIMS discharge and its relationship to deposition rate," *Plasma Sources Science and Technology*, vol. 19, p. 045014, 2010.

[62] N. Brenning, I. Axnäs, M. a. Raadu, D. Lundin, and U. Helmerson, "A bulk plasma model for dc and HiPIMS magnetrons," *Plasma Sources Science and Technology*, vol. 17, no. 4, p. 045009, 2008.

[63] A. Anders, J. Andersson, and A. Ehiasarian, "High power impulse magnetron sputtering: Current-voltage-time characteristics indicate the onset of sustained self-sputtering," *Journal of Applied Physics*, vol. 102, no. 2007, 2007.

[64] M. Palmucci, N. Britun, T. Silva, R. Snyders, and S. Konstantinidis, "Mass spectrometry diagnostics of short-pulsed HiPIMS discharges," *Journal of Physics D: Applied Physics*, vol. 46, p. 215201, 2013.

[65] V. Tiron, I.-L. Velicu, O. Vasilovici, and G. Popa, "Optimization of deposition rate in HiPIMS by controlling the peak target current," *Journal of Physics D: Applied Physics*, vol. 48, no. 49, p. 495204, 2015.

[66] K. Macak, V. Kouznetsov, J. Schneider, U. Helmersson, and I. Petrov, "Ionized sputter deposition using an extremely high plasma density pulsed magnetron discharge," *Journal of Vacuum Science & Technology A: Vacuum, Surfaces, and Films*, vol. 18, no. 4, p. 1533, 2000.

[67] C. Vitelaru, D. Lundin, G. D. Stancu, N. Brenning, J. Bretagne, and T. Minea, "Argon metastables in HiPIMS: time-resolved tunable diode-laser diagnostics," *Plasma Sources Science and Technology*, vol. 21, no. 2, p. 025010, 2012.

[68] J. Alami, P. Eklund, J. Andersson, M. Lattemann, E. Wallin, J. Bohlmark, P. Persson, and U. Helmersson, "Phase tailoring of Ta thin films by highly ionized pulsed magnetron sputtering," *Thin Solid Films*, vol. 515, pp. 3434–3438, 2 2007.

[69] D. Horwat and A. Anders, "Ion acceleration and cooling in gasless self-sputtering," *Applied Physics Letters*, vol. 97, pp. 5–7, 2010.

[70] M. Marinov, "Effect of ion bombardment on the initial stages of thin film growth," *Thin Solid Films*, vol. 46, no. 3, pp. 267–274, 1977.

[71] R. M. Bradley, J. M. E. Harper, and D. A. Smith, "Theory of thin-film orientation by ion bombardment during deposition," *Journal of Applied Physics*, vol. 60, no. 12, pp. 4160–4164, 1986.

[72] L. S. Yu, J. M. E. Harper, J. J. Cuomo, and D. A. Smith, "Alignment of thin films by glancing angle ion bombardment during deposition," *Applied Physics Letters*, vol. 47, no. 9, pp. 932–933, 1985.

[73] S. M. Rossnagel, "Directional and ionized physical vapor deposition for microelectronics applications," *Journal of Vacuum Science & Technology B: Microelectronics and Nanometer Structures*, vol. 16, no. 1998, p. 2585, 1998.

[74] a. Ehiasarian and W. Münz, "High power pulsed magnetron sputtered CrN x films," *Surface and coatings . . .*, vol. 164, pp. 267–272, 2003.

[75] A. Anders, "Metal plasmas for the fabrication of nanostructures," *Journal of Physics D: Applied Physics*, vol. 40, no. 8, pp. 2272–2284, 2007.

[76] A. Anders, J. Andersson, and A. Ehiasarian, "High power impulse magnetron sputtering: Current-voltage-time characteristics indicate the onset of sustained self-sputtering," *Journal of Applied Physics*, vol. 102, no. 11, 2007.

[77] J. Emmerlich, S. Mráz, R. Snyders, K. Jiang, and J. M. Schneider, "The physical reason for the apparently low deposition rate during high-power pulsed magnetron sputtering," *Vacuum*, vol. 82, no. 8, pp. 867–870, 2008.

[78] A. Anders, "Self-sputtering runaway in high power impulse magnetron sputtering: The role of secondary electrons and multiply charged metal ions," *Applied Physics Letters*, vol. 92, no. 20, 2008.

[79] J. Andersson and A. Anders, "Gasless sputtering: Opportunities for ultraclean metallization, coatings in space, and propulsion," *Applied Physics Letters*, vol. 92, no. 22, pp. 3–5, 2008.

[80] J. Andersson and A. Anders, "Self-sputtering far above the runaway threshold: An extraordinary metal-ion generator," *Physical Review Letters*, vol. 102, no. 4, pp. 1–4, 2009.

[81] a. V. Kozyrev, N. S. Sochugov, K. V. Oskomov, a. N. Zakharov, and a. N. Odivanova, "Optical studies of plasma inhomogeneities in a high-current pulsed magnetron discharge," *Plasma Physics Reports*, vol. 37, no. 7, pp. 621–627, 2011.

[82] a. P. Ehiasarian, a. Hecimovic, T. De Los Arcos, R. New, V. Schulz-Von Der Gathen, M. Bke, and J. Winter, "High power impulse magnetron sputtering discharges: Instabilities and plasma self-organization," *Applied Physics Letters*, vol. 100, no. 11, 2012.

[83] E. Chesta, C. M. Lam, N. B. Meezan, D. P. Schmidt, and M. a. Cappelli, "A characterization of plasma fluctuations within a Hall discharge," *IEEE Transactions on Plasma Science*, vol. 29, no. 4, pp. 582–591, 2001.

[84] N. Brenning, D. Lundin, T. Minea, C. Costin, and C. Vitelaru, "Spokes and charged particle transport in HiPIMS magnetrons," *Journal of Physics D: Applied Physics*, vol. 46, no. 8, p. 084005, 2013.

[85] A. Anders, "Self-organization and self-limitation in high power impulse magnetron sputtering," *Applied Physics Letters*, vol. 100, no. 22, pp. 2010–2015, 2012.

[86] a. Hecimovic, V. Schulz-von der Gathen, M. Böke, a. von Keudell, and J. Winter, "Spoke transitions in HiPIMS discharges," *Plasma Sources Science and Technology*, vol. 24, no. 4, p. 045005, 2015.

[87] S. Gallian, W. N. G. Hitchon, D. Eremin, T. Mussenbrock, and R. P. Brinkmann, "A phenomenological model for the description of rotating spokes in HiPIMS discharges," *Plasma Sources Science and Technology*, vol. 22, no. 5, p. 055012, 2013.

[88] N. Brenning and D. Lundin, "Alfvéns critical ionization velocity observed in high power impulse magnetron sputtering discharges," *Physics of Plasmas*, vol. 19, no. 2012, p. 093505, 2012.

[89] J. P. Boeuf and B. Chaudhury, "Rotating instability in low-temperature magnetized plasmas," *Physical Review Letters*, vol. 111, no. 15, pp. 1–5, 2013.

[90] P. Poolcharuansin, F. L. Estrin, and J. W. Bradley, "The use of segmented cathodes to determine the spoke current density distribution in high power impulse magnetron sputtering plasmas," *Journal of Applied Physics*, vol. 117, no. 16, p. 163304, 2015.

[91] U. V. Fahleson, "Experiments with Plasma Moving through Neutral Gas," *The Physics of Fluids*, vol. 4, no. 1, pp. 123–127, 1961.

[92] P. Poolcharuansin, B. Liebig, and J. W. Bradley, "More evidence for azimuthal ion spin in HiPIMS discharges," *Plasma Sources Science and Technology*, vol. 21, no. 1, p. 015001, 2011.

[93] J. Bohlmark, M. Lattemann, J. T. Gudmundsson, A. P. Ehiasarian, Y. Aranda Gonzalvo, N. Brenning, and U. Helmersson, "The ion energy distributions and ion flux composition from a high power impulse magnetron sputtering discharge," *Thin Solid Films*, vol. 515, no. 4, pp. 1522–1526, 2006.

[94] J. Andersson, P. Ni, and A. Anders, "Spectroscopic imaging of self-organization in high power impulse magnetron sputtering plasmas," *Applied Physics Letters*, vol. 103, 2013.

[95] A. Anders, P. Ni, and J. Andersson, "Drifting ionization zone in DC magnetron sputtering discharges at very low currents," *IEEE Transactions on Plasma Science*, vol. 42, no. 10, pp. 2578–2579, 2014.

[96] M. Panjan, S. Loquai, J. E. Klemberg-Sapieha, and L. Martinu, "Non-uniform plasma distribution in dc magnetron sputtering: origin, shape and structuring of spokes," *Plasma Sources Science and Technology*, vol. 24, no. 6, p. 065010, 2015.

[97] Y. Yang, X. Zhou, J. X. Liu, and A. Anders, "Evidence for breathing modes in direct current, pulsed, and high power impulse magnetron sputtering plasmas," *Applied Physics Letters*, vol. 108, no. 3, p. 034101, 2016.

[98] P. a. Ni, C. Hornschuch, M. Panjan, and A. Anders, "Plasma flares in high power impulse magnetron sputtering," *Applied Physics Letters*, vol. 101, no. 22, pp. 6–11, 2012.

[99] C. Huo, D. Lundin, M. a. Raadu, A. Anders, J. T. Gudmundsson, and N. Brenning, "On sheath energization and Ohmic heating in sputtering magnetrons," *Plasma Sources Science and Technology*, vol. 22, no. 4, p. 045005, 2013.

[100] A. Anders, "Localized heating of electrons in ionization zones: Going beyond the Penning-Thornton paradigm in magnetron sputtering," *Applied Physics Letters*, vol. 244104, 2014.

[101] P. Kudláček, J. Vlček, K. Burcalová, and J. Lukáš, "Highly ionized fluxes of sputtered titanium atoms in high-power pulsed magnetron discharges," *Plasma Sources Science and Technology*, vol. 17, no. 2, p. 025010, 2008.

[102] A. Anders, M. Panjan, R. Franz, J. Andersson, and P. Ni, "Drifting potential humps in ionization zones: The propeller blades of high power impulse magnetron sputtering," *Applied Physics Letters*, vol. 103, pp. 19–23, 2013.

[103] Y. Yang, K. Tanaka, J. Liu, and A. Anders, "Ion energies in high power impulse magnetron sputtering with and without localized ionization zones," *Applied Physics Letters*, vol. 106, no. 12, 2015.

[104] T. D. L. Arcos, R. Schröder, Y. A. Gonzalvo, V. S.-v. D. Gathen, and J. Winter, "Description of HiPIMS plasma regimes in terms of composition, spoke formation and deposition rate," *Plasma Sources Science and Technology*, vol. 23, no. 5, p. 054008, 2014.

[105] Edwards Vacuum, "APG100 Active Pirani Gauge," *Datasheet*, vol. 10, pp. 1–2, 2005.

[106] MKS instruments, "Type 627D Absolute Pressure Transducer," *Datasheet*, 2013.

[107] Edwards Vacuum, "AIM ACTIVE INVERTED MAGNETRON GAUGE 10 -2 TO 10 -9 mbar," Tech. Rep. c, 2013.

[108] E. Passoth, P. Kudrna, C. Csambal, J. F. Behnke, M. Tichý, and V. Helbig, "An experimental study of plasma density determination by a cylindrical Langmuir probe at different pressures and magnetic fields in a cylindrical magnetron discharge in heavy rare gases," *Journal of Physics D: Applied Physics*, vol. 30, no. 12, pp. 1763–1777, 1997.

[109] "Current Monitor Model 2877," *Pearson Electronics, INC.*, vol. 2877.SPX, p. 990506, 1999.

[110] S. L. Chen and T. Sekiguchi, "Instantaneous direct-display system of plasma parameters by means of triple probe," *Journal of Applied Physics*, vol. 36, no. 8, pp. 2363–2375, 1965.

[111] G. F. Matthews, "Tokamak plasma diagnosis by electrical probes," *Plasma Physics and Controlled Fusion*, vol. 36, no. 10, pp. 1595–1628, 1999.

[112] S. L. Chen, "Studies of the effect of ion current on instantaneous triple-probe measurements," *Journal of Applied Physics*, vol. 42, no. 1, pp. 406–412, 1971.

[113] R. L. Merlino, "Understanding Langmuir probe current-voltage characteristics," *American Journal of Physics*, vol. 75, no. 12, p. 1078, 2007.

[114] a. P. Ehiasarian, a. Hecimovic, J. Winter, T. D. L. Arcos, R. New, V. S.-v. D. Gathen, and M. Böke, "Plasma self-organisation in High Power Impulse Magnetron Sputtering Discharges," *IOP Conference Series: Materials Science and Engineering*, vol. 39, p. 012012, 2012.

[115] C. L. Ellison, Y. Raitses, and N. J. Fisch, "Cross-field electron transport induced by a rotating spoke in a cylindrical Hall thruster," *Physics of Plasmas*, vol. 19, no. 1, 2012.

[116] S. Turner, *CERN Accelerator School: Superconductivity in particle accelerators*. No. May 1995, 1989.

[117] S. Calatroni, S. Aull, S. Doebert, T. Junginger, A. P. Ehiasarian, J. Knobloch, and G. Terenziani, "Rf Characterization of Niobium Films for Superconducting Cavities," *Confernce paper IPAC2013*, no. August 2015, pp. 1–4, 2013.

[118] H. Padamsee, "The science and technology of superconducting cavities for accelerators," *Superconductor Science and Technology*, vol. 14, no. 4, pp. R28–R51, 2001.

[119] R. Russo, "Quality measurement of niobium thin films for Nb/Cu superconducting RF cavities," *Measurement Science and Technology*, vol. 18, no. 2212, pp. 2299–2313, 2007.

[120] J. Alami, K. Sarakinos, G. Mark, and M. Wuttig, "On the deposition rate in a high power pulsed magnetron sputtering discharge," *Applied Physics Letters*, vol. 89, no. 15, pp. 15–18, 2006.

[121] A. Hecimovic and a. P. Ehiasarian, "Time evolution of ion energies in HIPIMS of chromium plasma discharge," *Journal of Physics D: Applied Physics*, vol. 42, no. 13, p. 135209, 2009.

[122] D. M. Mattox, "Particle bombardment effects on thin-film deposition: A review," *Journal of Vacuum Science & Technology A: Vacuum, Surfaces, and Films*, vol. 7, no. 3, pp. 1105–1114, 1989.

[123] S. Mikoshiba and Y. Nakano, "Asymmetrical Probe Methods for Measurements in Streaming Plasma," *Japanese Journal of Applied Physics*, vol. 7, no. 4, p. 311, 1968.

[124] R. Franz, C. Clavero, J. Kolbeck, and A. Anders, "Influence of ionisation zone motion in high power impulse magnetron sputtering on angular ion flux and NbO$_x$ film growth," *Plasma Sources Sci. Technol.*, vol. 015022, pp. 1–11, 2015.

[125] H. Bragg, W and L. Bragg W, "The Reflection of X-rays by Crystals," *Proc. R. Soc. Lond A*, vol. 88, no. 605, p. 428, 1913.

[126] G. C. A. M. Janssen, "Stress and strain in polycrystalline thin films," *Thin Solid Films*, vol. 515, no. 17, pp. 6654–6664, 2007.

[127] M. Hála, J. Čapek, O. Zabeida, J. E. Klemberg-Sapieha, and L. Martinu, "Pulse management in high power pulsed magnetron sputtering of niobium," *Surface and Coatings Technology*, vol. 206, no. 19-20, pp. 4186–4193, 2012.

[128] J. T. Gudmundsson, P. Sigurjonsson, P. Larsson, D. Lundin, and U. Helmersson, "On the electron energy in the high power impulse magnetron sputtering discharge," *Journal of Applied Physics*, vol. 105, no. 12, pp. 18–21, 2009.

[129] D. Horwat and A. Anders, "Compression and strong rarefaction in high power impulse magnetron sputtering discharges," *Journal of Applied Physics*, vol. 108, no. 12, 2010.

[130] J. T. Gudmundsson, J. Alami, and U. Helmersson, "Spatial and temporal behavior of the plasma parameters in a pulsed magnetron discharge," *Surface and Coatings Technology*, vol. 161, no. 2-3, pp. 249–256, 2002.

[131] A. Rauch, R. J. Mendelsberg, J. M. Sanders, and A. Anders, "Plasma potential mapping of high power impulse magnetron sputtering discharges," *Journal of Applied Physics*, vol. 111, 2012.

[132] A. Mishra, P. J. Kelly, and J. W. Bradley, "The evolution of the plasma potential in a HiPIMS discharge and its relationship to deposition rate," *Plasma Sources Science and Technology*, vol. 19, no. 4, p. 045014, 2010.

[133] H. Y. W. Tsui, R. D. Bengtson, G. X. Li, H. Lin, M. Meier, C. P. Ritz, and A. J. Wootton, "A new scheme for Langmuir probe measurement of transport and electron temperature fluctuations," *Review of Scientific Instruments*, vol. 63, no. 10, pp. 4608–4610, 1992.

[134] K. Kawashima, Y. Miyoshi, S. Oldenburger, S. Inagaki, H. Arakawa, Y. Nagashima, T. Yamada, M. Sasaki, T. Kobayashi, K. Uriu, S. Sugita, M. Yagi, N. Kasuya, A. Fujisawa, S. I. Itoh, and K. Itoh, "Evaluation of electron temperature fluctuations using two different probe techniques in Plasma Assembly For Nonlinear Turbulence Analysis (PANTA)," *Plasma and Fusion Research*, vol. 6, no. 1 SPECIAL ISSUE, pp. 4–7, 2011.

[135] P. M. Bryant, S. a. Voronin, J. W. Bradley, and a. Vetushka, "Time-resolved triple probe investigations of a pulsed magnetron discharge," *Journal of Applied Physics*, vol. 102, no. 4, pp. 1–11, 2007.

[136] L. Meng, A. N. Cloud, S. Jung, and D. N. Ruzic, "Study of plasma dynamics in a modulated pulsed power magnetron discharge using a time-resolved Langmuir probe," *Journal of Vacuum Science & Technology A: Vacuum, Surfaces, and Films*, vol. 29, no. 1, p. 11024, 2011.

[137] L. Meng, H. Yu, M. M. Szott, J. T. Mclain, and D. N. Ruzic, "Downstream plasma transport and metal ionization in a high-powered pulsed-plasma magnetron," *JOURNAL OF APPLIED PHYSICS*, vol. 115, no. 223301, pp. 1–10, 2014.

[138] J. Alami, J. T. Gudmundsson, J. Bohlmark, J. Birch, and U. Helmersson, "Plasma dynamics in a highly ionized pulsed magnetron discharge," *Plasma Sources Science and Technology*, vol. 14, no. 3, pp. 525–531, 2005.